University of California

Los Angeles

Inclusive Search for Anomalous High-p_T Like-Sign Lepton Pair Production at the Fermilab Tevatron Collider

A dissertation submitted in partial satisfaction

of the requirements for the degree

Doctor of Philosophy in Physics

by

Matthew Peter Worcester

2004

The dissertation of Matthew Peter Worcester is approved.

Robert Cousins

John DeMarco

Jay Hauser

David Saltzberg, Committee Chair

University of California, Los Angeles

2004

For my parents, with love

Table of Contents

List of Figures

List of Tables

Acknowledgments

I would like to thank my advisor David Saltzberg for his support, encouragement, and instruction. His patient dedication to my work and immense knowledge of physics made this thesis possible.

Along with David, most of my development as a physicist is indebted to Jane Nachtman. If I am at all a good physicist it is because Jane showed me how to be a great one.

I would like to thank my friends and colleagues at CDF. Kaori Maeshima, Hartmut Stadie, and the rest of the Consumer Monitoring group taught me C++ by fiat, without ever acting like my questions were ridiculously simple. Bill Ashmanskas, Greg Feild, Nate Goldschmidt, Carla Grosso-Pilcher, Steven Miller, Steve Nahn, Monica Tecchio, Heather Ray, Peter Wittich and the rest of the trigger experts helped me through the joys and despairs of getting electronics to work. Aaron Dominguez, Greg, Juan-Pablo Fernandez, Kaori, J. J. Schmidt and the rest of the CDF runners whipped me into shape. From countless hours in the control room to countless laps around the Tevatron ring they made my time at CDF a pleasure.

This thesis would be unfinished without the hard work and trenchant advice from the like-sign dilepton analysis godparents: Michael Schmidt, Kaori Maeshima, and Aurore Savoy-Navarro.

I must also thank my friends at UCLA. Kip Bishofberger, Dave LaFontese, Jason Mumford, Jay Smallwood, Lisa Weston, Jeremiah Williams, and the other graduate students in my class pulled me through two years and one epic exam worth of study. Fellow physicists Mike Van Zeeland and Steve Vincena got me to

the surf and back every morning. Ryan, J.P., Sam, and everyone else on UCLA Smaug Ultimate Disc kept me playing on the fields. Penny Lucky, Joyce Norton, An-chi Kao and the rest of the Physics Graduate and HEP staffs always went above the call of duty to help me.

My parents Peter and Donna Worcester have been behind me all the way. This thesis is dedicated to them. My brother Bryce has always been there for me and the support from the rest of my family has never wavered.

Finally, I thank my wife Elizabeth for her love and support.

Vita

[redacted]

1998	Teaching Assistant in Physics 2D and 2DL, Relativity and Quantum Physics with associated Modern Physics Laboratory. (UCSD, Prof. V. Sharma)
1998	John Holmes Malmberg Prize. (Physics, UCSD)
1998	B.S. Physics and B.A. Literatures in English (*summa cum laude*), University of California, San Diego.
1998–2001	Alyne and Leon Camp Fellowship. (Physics, UCLA)
1999	Teaching Assistant in Physics 6A, Physics for Life Sciences Majors: Mechanics. (UCLA, Prof. W. Gekelman)
2000	M.S. Physics, University of California, Los Angeles.
2000	Teaching Assistant in Physics 180F, Elementary Particle Physics Laboratory. (UCLA, Prof. D. Saltzberg)
2001	Graduate Student Award to Attend the 51st Meeting of Nobel Laureates. (U.S. Department of Energy/Oak Ridge Associated Universities)
2001–present	Research Assistant, Physics Department, UCLA.

Publications and Presentations

D. Acosta, *et al.* (CDF Collaboration), "Inclusive Search for Anomalous Production of High-p_T Like-Sign Lepton Pairs in $p\bar{p}$ Collisions at $\sqrt{s} = 1.8$ TeV," hep-ex/0405064, 2004.

M. Worcester, *The LSD Experience at CDF Run I.* Poster presented at Lepton Photon 2003, Fermi National Accelerator Laboratory, Batavia, Illinois, USA. August 11-16, 2003.

—, *Like-Sign Dilepton Search for Chargino-Neutralino Production at CDF.* Presented at New Perspectives 2003, Fermi National Accelerator Laboratory, Batavia, Illinois, USA. June 3-5, 2003.

—, *Like-Sign Dilepton Search for Chargino-Neutralino Production at CDF.* Presented at the meeting of the American Physical Society, Philadelphia, Pennsylvania, USA. April 5-8, 2003.

—, J. Nachtman, and D. Saltzberg (CDF Collaboration), "Like-Sign Dilepton Search for Chargino-Neutralino Production at CDF," Int. J. Mod. Phys. A **16S1B**: 797-800, 2001.

—, *Like-Sign Dilepton Search for Chargino-Neutralino Production at CDF.* Presented at the meeting of the Division of Particles and Fields of the American Physical Society, Columbus, Ohio, USA. August 9-12, 2000.

—, *Search for Supersymmetry with Like-Sign Dileptons at CDF.* Presented at the meeting of the American Physical Society, Long Beach, California, USA. April 29-May 2, 2000.

S. Rolli, J. D. Lewis, H. Ray, J. Nachtman, and M. Worcester, "Hardware Trigger Simulation at CDF," in *Proceedings of the International Conference on Computing in High-Energy Physics and Nuclear Physics*:250-255, 2000.

S. Abel, *et al.* (SUGRA Working Group Collaboration), "Report of the SUGRA Working Group for Run II of the Tevatron," hep-ph/0003154, 2000.

M. Worcester, *Search for Chargino-Neutralino Production at CDF Using Like-Sign Dileptons.* Presented at New Perspectives 1999, Fermi National Accelerator Laboratory, Batavia, Illinois, USA. July 8-10, 1999.

J. Nachtman, M. Worcester, and D. Saltzberg, "Study of a Like-Sign Dilepton Search for Chargino-Neutralino Production at CDF," in *Proceedings of the Division of Particles and Fields of the American Physical Society*, hep-ex/9902010, 1999.

M. Worcester, *Feasibility Study of a Search for Chargino-Neutralino Production at CDF Using Like-Sign Dileptons.* Presented at the meeting of the Division of Particles and Fields of the American Physical Society, Los Angeles, California, USA. January 5-9, 1999.

Abstract of the Dissertation

Inclusive Search for Anomalous High-p_T Like-Sign Lepton Pair Production at the Fermilab Tevatron Collider

by

Matthew Peter Worcester

Doctor of Philosophy in Physics

University of California, Los Angeles, 2004

Professor David Saltzberg, Chair

We search for anomalous production of events with at least two charged, isolated, like-sign leptons with $p_T > 11$ GeV/c using a 107 pb^{-1} sample of $\sqrt{s} = 1.8$ TeV $p\bar{p}$ collisions collected by the CDF detector. We define a signal region containing low background from Standard Model processes. To avoid bias, we fix the final cuts before examining the event yield in the signal region using control regions to test the Monte Carlo predictions. We observe no events in the signal region, consistent with an expectation of $0.63^{+0.84}_{-0.07}$ events. We present 95% confidence level limits on new physics processes in both a signature-based context as well as within a representative minimal supergravity ($\tan\beta = 3$) model.

CHAPTER 1

Introduction

> *For small erections may be finished by their first architects; grand ones, true ones, ever leave the copestone to posterity. God keep me from ever completing anything. This whole book is but a draught – nay, but the draught of a draught. Oh, Time, Strength, Cash, and Patience!* [1]

Elementary particle physics is the study of the fundamental particles of matter and their interactions. By "elementary" physicists mean that these particles have no measurable internal structure or components. They can thus be treated as ideal or point-like particles to the smallest scale of size available to physicists in the modern era, about 10^{-19} meters. By "fundamental" we mean that the physical properties such as mass, electric charge, and spin of these infinitesimal particles underlies at the most basic level the physical world of our everyday experience. These physical properties dictate how the fundamental particles themselves compose more complex particles and atoms. The properties of the fundamental particles then govern how those atoms in turn build molecules, cells, organisms and all bulk matter.

The laws of classical biology, chemistry and physics all rely on bulk properties of materials and classical mechanics, *i.e.* many millions of elementary particles moving slowly compared to the speed of light ($c = 2.9979 \times 10^8$ meters/second).

When dealing with individual particles or atoms physicists must replace the laws of classical mechanics with those of quantum mechanics, the physics of single quanta. When dealing with particles moving very quickly, generally greater than $\frac{1}{10}c$, physicists must replace classical dynamics with relativistic dynamics. In the case of both extremes – the regime of modern high-energy particle physics – relativistic dynamics and quantum mechanics must be combined into a relativistic quantum field theory (QFT).

The fundamental particles currently known to physicists are the quarks, leptons, and gauge bosons. The gauge bosons (integer spin) mediate the interactions between the quarks (q) and leptons (ℓ), which have $\frac{1}{2}$-integer spin. One or more gauge bosons have been observed for each of the fundamental forces currently described by physicists with a working QFT: electromagnetic, weak nuclear, and strong nuclear. The QFT describing the electromagnetic and nuclear interactions between quarks, leptons, and gauge bosons is called the Standard Model (SM) of particle physics.

1.1 The Standard Model

The SM is a composite of several other relativistic quantum field theories. It combines Quantum Chromodynamics (QCD) [2], the theory describing the color charge and the strong nuclear force, with the electroweak model [3], itself a combination of Quantum Electrodynamics (describing the electromagnetic force) with the theory of flavor charge and weak nuclear force. Tables 1.1, 1.2, and 1.3 show all of the elementary particles in the SM and some of their important physical properties [4].

The SM has been extremely successful in explaining current observable phe-

Generation	Quark Flavor	Electric Charge	Bare Mass range (MeV/c^2)
First	down (d)	$-1/3$	5.0–8.5
	up (u)	$+2/3$	1.5–4.5
Second	strange (s)	$-1/3$	80–155
	charm (c)	$+2/3$	1.0–1.4 $\times 10^3$
Third	bottom (b)	$-1/3$	4.0–4.5 $\times 10^3$
	top (t)	$+2/3$	174 $\times 10^3$

Table 1.1: Quarks, spin $\frac{1}{2}$.

Generation	Lepton Flavor	Electric Charge	Mass (MeV/c^2)
First	electron (e)	-1	0.511
	electron neutrino (ν_e)	0	$< 3 \times 10^{-3}$
Second	muon (μ)	-1	105.66
	muon neutrino (ν_μ)	0	< 0.19
Third	tau (τ)	-1	1,777
	tau neutrino (ν_τ)	0	< 18.2

Table 1.2: Leptons, spin $\frac{1}{2}$.

Boson	Force Mediated	Electric Charge	Mass (MeV/c^2)
photon (γ)	electromagnetic	0	$< 2\times10^{-19}$
$W^{\pm}$	(charged) weak nuclear	±1	80,423
Z^0	(neutral) weak nuclear	0	91,188
gluon (g)	strong nuclear	0	0

Table 1.3: Gauge Bosons, spin 1.

nomena and making accurate predictions for new physics later confirmed by experiment. A glaring exception, however, is gravity. To date, physicists have neither created a successful theory combining the SM with Einstein's theory of general relativity [5] nor observed the graviton, the gauge boson thought to mediate the force of gravity between two massive particles. The first step of a unified theory of all four forces would be to create a working relativistic *quantum* theory of gravity [6]. The fundamental problems in resolving general relativity with quantum mechanics leads physicists to not include gravity or its spin 2 boson the graviton in the SM.

An important point about theories in general and the SM specifically is that all theories are works in progress. They are always subject to revision. For example, when Wolfgang Pauli and Enrico Fermi theorized the existence of the electrically neutral, conservation-of-energy saving neutrino in the 1930's (see Chapter 1 of Ref. [7] and references therein), they postulated a very light or massless neutrino. But as the SM evolved after the experimental discovery of the neutrino [8], for simplicity it contained a set of massless neutrinos. However, in only the last six years modern neutrino detectors have shown clear, undeniable proof of neutrinos in flight oscillating between lepton family eigenstates, thus implying distinct mass eigenstates, thus implying mass [9]. Physicists have now included non-zero

neutrino mass in the SM and experiments have constrained the neutrino mass to be small as shown in Table 1.2. The SM, like any good theory, not only explains and predicts, but also adapts.

However, the SM contains other, more fundamental, unresolved issues and unanswered questions.

1.1.1 Standard Model Masses

The SM does not have any inherent mechanism to provide the lepton and quark masses shown in Tables 1.1 and 1.2. In the SM the fermionic (spin $\frac{1}{2}$) fields that describe the leptons and quarks are initially massless. Additionally, the SM must have a mechanism to break the symmetry at the electroweak scale, $\sim$100 GeV/c^2, to provide masses for the $W^{\pm}$ and Z^0 bosons while leaving the γ massless. To provide these, a scalar (spin 0) "Higgs" field is inserted *ad hoc* into the theory [10]. Masses for the SM leptons and quarks are generated via the interaction of their fermionic fields with the scalar Higgs field. This requires the existence of a neutral, spinless gauge boson, the Higgs (H^0), which has not been observed experimentally [11]. Despite the lack of evidence to support the Higgs boson, this mechanism is so necessary for SM masses that it has generally been incorporated into the canonical SM.

1.1.2 Hierarchy

The lack of observation of the Higgs is not yet a critical problem as the theory allows for much heavier Higgs particles than can be produced in the highest-energy accelerators; physicists simply may not be able to create the Higgs in the lab. However, no one has yet provided a compelling fundamental reason why the Higgs mechanism breaks the symmetry of the SM at the electroweak scale.

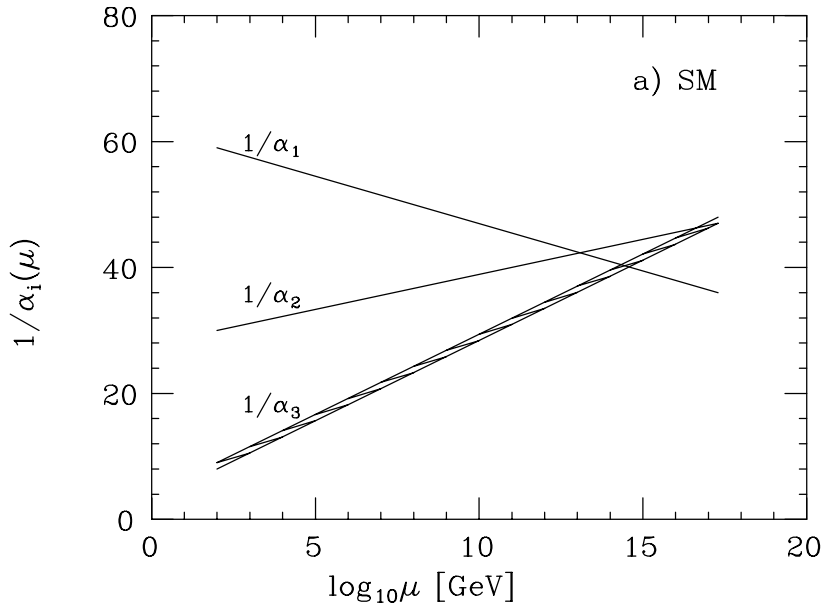

Figure 1.1: SM coupling constants as a function of energy scale μ. α_1 is hypercharge, α_2 is weak nuclear, and α_3 is strong nuclear. Adapted from Ref. [12].

Moreover, no explanation is given for the vast differences in mass scale between the lepton generations themselves (a factor of $\sim 10^3$ between the τ and the e) and the quark generations themselves ($\sim 10^5$ between the t and u quarks).

1.1.3 Grand Unification

The SM coupling constants (α) dictate the relative strength of the interactions between the leptons and quarks (see, for example, Chapter 2 of Ref. [7] and references therein). α_1 is the hypercharge (a mixture of the weak and electromagnetic) coupling constant, and α_2 and α_3 are the weak and strong nuclear force coupling constants, respectively. These coupling constants depend on the energy scale at which they are measured. Figure 1.1 shows the theoretically predicted SM coupling constants as a function of energy scale for the three forces. At the

Fermilab Tevatron collider scale ($\sqrt{s} = 1.8 \times 10^3$ GeV) they are $\alpha_1 = 0.00781$, $\alpha_2 = 0.03397$, and $\alpha_3 = 0.120$ [4].

As Fig. 1.1 shows, the SM does not contain any energy scale at which the relative strength of these forces unifies for all three. Such a "grand unification" scale is very attractive to many physicists. Some suggest that grand unification is mandatory in order to include gravity in the SM [13].

1.1.4 Naturalness

While the Higgs mechanism and differences in mass scale hierarchy are puzzling, they may be simply the way things are in this universe. A more fundamental problem with the SM internally is the difficulty in tuning the parameters of the theory to cancel out large divergences due to the scalar Higgs field. To first order, the Higgs field, h, potential may be simply modeled as:

$$V \sim M_{h0}^2 h^2 + \lambda h^4 \ , \tag{1.1}$$

where M_{h0} is the zeroth order Higgs mass and λ is the unitless parameter defining the order of expansion in the perturbation of the theory. The first order (proportional to λ) Higgs boson mass, M_h, containing the Higgs field self-interaction terms is then:

$$M_h^2 \sim M_{h0}^2 + \frac{\lambda}{4\pi^2}\Lambda^2 + \delta M_h^2 \ , \tag{1.2}$$

where Λ is the energy scale cutoff of order 10^{18} GeV/c^2 and δM_h is the first order correction to the Higgs mass [14]. To deliver the fermionic and bosonic masses given in Section 1.1, the theory needs $M_h \leq 1$ TeV/c^2. This requires δM_h^2 to cancel the Λ^2 term to approximately one part in 10^{16}. This problem repeats itself at each order of perturbation of the SM. Thus, the parameter δM_h must be fine-tuned at every order of expansion of the theory to better than 10^{16}.

While this is theoretically possible, most physicists regard this "unnaturalness" of the Higgs boson as a driving motivation to introduce new physics to the SM to cancel the quadratic growth terms (proportional to Λ^2) in the Higgs field in a manner consistent with the initial assumptions of the theory, rather than with the delicate fine-tuning of parameters at every order of perturbation.

1.2 Physics Beyond the SM

Physicists have proposed a large number of theories beyond the SM to introduce terms into the SM that will cancel the quadratic divergences in the Higgs field. Some are better motivated than others; some are almost completely excluded by experimental results; and none have been experimentally confirmed. All of the theories under serious consideration posit new particles at the electroweak scale, allowing physicists working at high-energy colliders and with astroparticle experiments to probe the new physics. These theories include quark compositeness or leptoquarks [15], axions [16], and supersymmetry [17] to name a few. Currently the one of the most well-motivated theories of physics beyond the SM is supersymmetry.

1.2.1 Supersymmetry

One well-known symmetry of Quantum Electrodynamics is antiparticle symmetry. This assumes that for each charged particle there exists an antiparticle with identical physical properties such as mass and spin *except* that it has the opposite charge. For example, the antiparticle to the e (negative charge) is the positron, usually written e^+, with positive charge and identical mass and spin $\frac{1}{2}$. This is why there are two charged W bosons, W^+ and W^-, but only one neu-

tral Z^0 boson. This symmetry is a well-understood and experimentally verified feature of the SM.

Supersymmetry (SUSY) further assumes a set of fermionic ($\frac{1}{2}$-integer spin) counterpart or superpartner fields for each bosonic (integer spin) particle in the current SM, and a set of bosonic superpartner fields for each fermion. Thus, SUSY posits a symmetry that relates particles of different spin. As a massive scalar (S) boson the Higgs will receive fermionic counterparts. The addition of these superpartner fields introduces to the first order Higgs mass new terms for massive fermionic (F) fields which come directly from the superpartner fields. Thus, under SUSY, Equation 1.2 becomes:

$$M_h^2 \sim M_{h0}^2 + \frac{g_F^2}{4\pi^2}(\Lambda^2 + \delta m_F^2) - \frac{g_S^2}{4\pi^2}(\Lambda^2 + \delta m_S^2) \ . \tag{1.3}$$

Here g_i^2 are the relative strength of the couplings and δm_i^2 are the mass corrections from the fermionic and scalar field self-interactions [14]. The term proportional to g_S^2 is the original correction to the Higgs mass in Equation 1.2, and the term proportional to g_F^2 is new. The critical feature of including both fermionic and scalar fields is the relative negative sign between the two mass correction terms. If the constraint $g_F^2 = g_S^2 \equiv g^2$ is applied then Equation 1.3 reduces to:

$$M_h^2 \sim M_{h0}^2 + \frac{g^2}{4\pi^2}(\delta m_F^2 - \delta m_S^2) \ , \tag{1.4}$$

removing the quadratic divergence terms from the Higgs mass. If the masses of the new fermionic and scalar fields are not too different [18], then SUSY causes the Higgs mass to become well-behaved. Also note that because the cancellations come from terms added by the initial assumptions of the SUSY model, they occur naturally at each order of perturbative expansion of the theory [19].

1.2.2 R-parity

The SUSY Lagrangian contains terms which allow for interactions leading to the violation of the lepton and baryon number conservation in the SM. However, no evidence for such a process, *e.g.* proton decay, has been experimentally observed. Thus, SUSY introduces a new multiplicative quantum number, R-parity, the conservation of which protects against lepton and baryon number violation:

$$R \equiv (-1)^{3(B-L)+2S} \ , \tag{1.5}$$

where B is baryon number, L is lepton number, and S is the particle spin [20]. Thus, SM particles have $R = +1$ and SUSY particles have $R = -1$. If R-parity is conserved, then SUSY particles must be produced in pairs. Furthermore, SUSY particles are unable to decay to SM particles alone: at least one superpartner must be produced in each decay [21]. This implies that SUSY requires a lightest supersymmetric particle (LSP) which is massive and stable.

As an LSP candidate has not been experimentally observed, it is assumed to be electrically neutral and interact very weakly via the nuclear forces. Thus, if produced in the lab it will escape direct detection. Moreover, the LSP is considered a good candidate for cold dark matter [22]. Cold dark matter is required to balance the composition of matter in the universe to fit the experimental data from cosmic microwave background anisotropy measurements [23]. The SM has no good candidate particle as a cold dark matter source.

1.2.3 Minimal Supersymmetry

In order to make SUSY theory tractable to experimental measurements, it has been simplified to the Minimal Supersymmetric Standard Model (MSSM). The MSSM assumes only one superpartner field per SM particle. The MSSM also

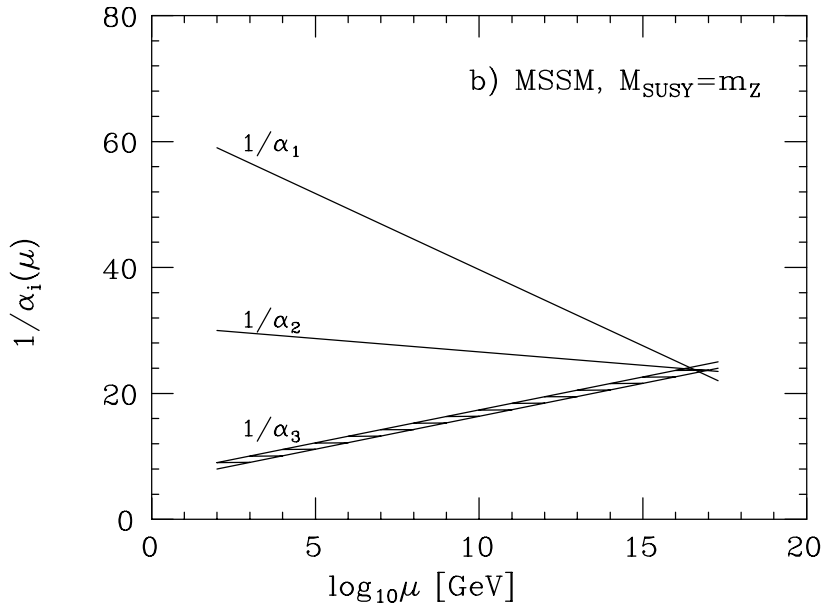

Figure 1.2: MSSM coupling constants as a function of energy scale μ. α_1 is hypercharge, α_2 is weak nuclear, and α_3 is strong nuclear. Adapted from Ref. [12].

allows the Higgs field to be charged. The combination of charged and neutral Higgs bosons is called a Higgs doublet. The MSSM also requires a second Higgs doublet ($H_2^{\pm,0}$) in addition to the single Higgs doublet (now $H_1^{\pm,0}$) introduced in Section 1.1.1 (and superparters for both Higgs) to cancel anomalies and provide masses to all the leptons and quarks [24]. Physicists have chosen the terminology such that the SUSY partners are called the *sparticles*; the bosonic superpartners to the fermions are the *sfermions*, *e.g.* the sleptons ($\tilde{\ell}$) and the squarks ($\tilde{q}$); the fermionic superpartners to the gauge bosons gain an *-ino*, *e.g.* the gauginos.

1.2.4 Grand Unification Revisited

The complete MSSM still has over 100 free parameters in the theory. However, a number of assumptions can be made to produce a simplified MSSM model with

a reduced number of free parameters.

One such reduced MSSM model unifies the coupling constants at the grand unification scale, as discussed in Section 1.1.3. This is done by placing the MSSM in a "supergravity" inspired framework, which includes gravity among the forces [25]. Figure 1.2 shows the MSSM coupling constants as a function of energy scale. The strengths of the couplings have been unified at a point near 10^{16} GeV. This assumption alters the MSSM model sufficiently for physicists to give it its own name: minimal Supergravity (mSUGRA).

Under mSUGRA the free parameters in the MSSM have been reduced to five [21]. These parameters directly and indirectly determine the sparticle production cross sections, masses, and decay branching ratios. The five parameters are:

- $\tan\beta$, the ratio of the vacuum expectation values of the two Higgs fields
- A_0, the Higgs-squark-squark trilinear coupling constant
- $sign(\mu)$, where μ is the unmixed Higgsino mass or the SUSY-conserving Higgs mass parameter
- m_0, the universal scalar mass
- $m_{1/2}$, the universal gaugino mass

1.2.5 Sparticles

In mSUGRA each SM particle is assigned a superparter with the same quantum numbers but differing by $\frac{1}{2}$ unit of spin, as discussed in Section 1.2.3. The quark, lepton, and neutrino superparters are the scalar squarks, sleptons, and

SM Particles		SUSY Particles		
		Weak Eigenstates		Mass Eigenstates
particle	spin	particle	spin	
$q = u, d, s, c, b, t$	$\frac{1}{2}$	$\tilde{q}_L, \tilde{q}_R$ squarks	0	$\tilde{q}_1, \tilde{q}_2$
$\ell = e, \mu, \tau$	$\frac{1}{2}$	$\tilde{\ell}_L, \tilde{\ell}_R$ sleptons	0	$\tilde{\ell}_1, \tilde{\ell}_2$
$\nu = \nu_e, \nu_\mu, \nu_\tau$	$\frac{1}{2}$	$\tilde{\nu}$ sneutrinos	0	$\tilde{\nu}$
g	1	$\tilde{g}$ gluino	$\frac{1}{2}$	$\tilde{g}$
$W^{\pm}$	1	$\tilde{W}^{\pm}$ Wino	$\frac{1}{2}$	
$H_1^{\pm}$	0	$\tilde{H}_1^{\pm}$ Higgsino	$\frac{1}{2}$	$\tilde{\chi}_{1,2}^{\pm}$
$H_2^{\pm}$	0	$\tilde{H}_2^{\pm}$ Higgsino	$\frac{1}{2}$	charginos
γ	1	$\tilde{\gamma}$ photino	$\frac{1}{2}$	
Z^0	1	$\tilde{Z}^0$ Zino	$\frac{1}{2}$	$\tilde{\chi}_{1,2,3,4}^0$
H_1^0	0	$\tilde{H}_1^0$ Higgsino	$\frac{1}{2}$	neutralinos
H_2^0	0	$\tilde{H}_2^0$ Higgsino	$\frac{1}{2}$	

Table 1.4: Particle spectrum of the MSSM. Adapted from Ref. [26].

sneutrinos, respectively. The gauge boson superparters are the fermionic gauginos: photino, Wino, Zino, gluino, and Higgsinos. The SM particles and their mSUGRA superpartners are summarized in Table 1.4.

Notice that the sparticles have different weak and mass eigenstates. The mass eigenstates are superpositions of the weak eigenstates which correspond directly to one SM superpartner. However, only the mass eigenstates are observable in the laboratory. Thus, experimental physicists search for squarks, sleptons, sneutrinos, gluinos, charginos, and neutralinos. If R-parity is conserved as discussed in Section 1.2.2, the LSP must be the lightest massive, weakly-interacting, neutral sparticle. The mSUGRA LSP is usually taken to be the lightest neutralino,

$\tilde{\chi}_1^0$, which will be difficult to observe experimentally.

The chargino and neutralino masses are determined by the mSUGRA parameter $m_{1/2}$. The cross section for chargino-neutralino production depends both on the sparticle masses, determined by m_0 and $m_{1/2}$, and couplings, which are set by μ and $\tan\beta$ [27]. The cross section for squark-gluino production depends on the masses, determined by m_0 and $m_{1/2}$ [28]. We assume no $\tilde{\tau}$ mixing by taking the trilinear coupling constant A_τ to be zero.

With $A_\tau = 0$, the parameters μ and $\tan\beta$ determine the mixing in the gaugino sector, which in turn indirectly affects the chargino and neutralino decay branching ratios. The chargino-neutralino branching ratios are primarily determined by the masses of the sleptons and squarks, set by m_0 [29]. The squark and gluino masses, set by m_0 and $m_{1/2}$, determine the squark-gluino decay branching ratios [28]. For sparticle mass spectra in GeV/c^2 at a set of representative points in mSUGRA-space see Chapter III of Ref. [30].

1.2.6 Experimental mSUGRA

SUSY in general and mSUGRA specifically provide a range of attractive theoretical improvements over the SM. Many direct searches for specific production signatures of mSUGRA sparticles have been carried out at the current generation of high-energy physics colliders. For example, the Collider Detector at Fermilab and DØ experiments at Run I of the Fermilab Tevatron have searched for direct evidence of chargino-neutralino production and decay in proton-antiproton collisions at center-of-mass energy $\sqrt{s} = 1.8$ TeV via the reaction:

$$\tilde{\chi}_1^\pm \tilde{\chi}_2^0 \rightarrow \ell^\pm \ell^\pm \ell^\mp \tilde{\chi}_1^0 \tilde{\chi}_1^0 \nu \ , \tag{1.6}$$

in which all three leptons are observed directly by the particle detectors and the neutralinos and neutrino escape detection due to their weak interaction strengths [31, 32]. However, the results from these searches have been expressed only in relation to mSUGRA production of $\tilde{\chi}_1^{\pm}\tilde{\chi}_2^0$: they say nothing about any other theories of non-Standard Model physics.

Despite these and other searches, the sparticles are as yet unobserved by experimental physicists up to mass scales on the order of ~ 100 GeV/c^2 [33]. If mSUGRA requires a superparter for the 0.511 MeV/c^2 SM electron, then it must be much heavier than its counterpart. Thus, SUSY must be broken at the electroweak scale [34]. Furthermore, because we constrained $M_h \leq 1$ TeV/c^2 in Section 1.1.4 to preserve lepton and quark masses at the electroweak scale, we have already placed a constraint on the new physics from SUSY to also be ≤ 1 TeV/c^2. This makes it possible for the current data from Run II of the Fermilab Tevatron and the next generation of high-energy physics experiments such as the CERN Large Hadron Collider to probe a almost all of mSUGRA parameter space [35].

1.3 Inclusive Searches

An attractive method of searching for new physics with current data in parallel with direct search techniques is the inclusive search. Rather than search for particle production and decay via a specific model, such as mSUGRA, an inclusive search seeks to reduce particle production from known SM processes while remaining open to as much new physics as possible [36]. Such a search yields results on any number of new physics processes for which the final state has sensitivity. For this reason inclusive searches are also known as model-independent searches [37]. However, it is important to note that while a search can be purely inclusive, any discussion of results in the context of a specific model must tie itself to model-

dependent assumptions, and is therefore not entirely model-independent.

1.3.1 Like-Sign Dileptons

This thesis presents an inclusive search for like-sign lepton pair production at the Fermilab Tevatron Collider. In the context of mSUGRA $\tilde{\chi}_1^{\pm}\tilde{\chi}_2^0$ production, we search for the signal:

$$\tilde{\chi}_1^{\pm}\tilde{\chi}_2^0 \rightarrow \ell^{\pm}\ell^{\pm} + X \ , \tag{1.7}$$

where X includes any particles beyond the minimum requirement of the like-sign lepton pair. With $X = \ell^{\mp}\tilde{\chi}_1^0\tilde{\chi}_1^0\nu$ this is equivalent to Equation 1.6. Thus, we can interpret the direct $\tilde{\chi}_1^{\pm}\tilde{\chi}_2^0$ searches described in Section 1.2.6 as a subset of this inclusive dilepton channel. Results from the direct and inclusive searches can then be combined to yield greater sensitivity to $\tilde{\chi}_1^{\pm}\tilde{\chi}_2^0$ production than either search channel alone [38].

However, the like-sign dilepton (LSD) signature is not limited to expressing results in the context of mSUGRA; it can be used to probe a large range of new physics at proton-antiproton colliders [39]. As shown in Chapter 3, LSD greatly reduces background from SM processes while retaining sensitivity to *any other* physics process that results in the $\ell^{\pm}\ell^{\pm} + X$ final state. This includes a number of physics beyond the SM processes in addition to SUSY, such as majorana neutrino production [40] and doubly-charged Higgs production [41].

1.3.2 Blind Analyses

A blind analysis seeks to reduce human bias in the final result as much as possible by keeping the final result and the data upon which it is based hidden from physicists until the analysis is essentially complete [42]. In the context of

search analyses a set of selection criteria, called "cuts," are used to define a signal region in the data. By not examining the data in this signal region, physicists keep themselves blind to the final answer, which prevents any (un)conscious hand-picking of data or modifying of systematic uncertainties which may favor a specific result, such as the discovery or exclusion of new physics.

For the LSD search, backgrounds to the $\ell^{\pm}\ell^{\pm} + X$ signal are generated with Monte Carlo simulations. We also use Monte Carlo to generate signal produced by a given beyond-the-SM process, such as mSUGRA production of $\tilde{\chi}_1^{\pm}\tilde{\chi}_2^0$. In high-energy physics, Monte Carlo programs take as their starting point the initial physics processes that can occur in an experiment, including known or predicted production cross sections. They are then given a combination of analytical results and QCD-based models of decay branching ratios to simulate the different types of final state particles which are produced by each physics process.

For the Fermilab Tevatron, we employ Monte Carlo programs which simulate the proton-antiproton collider environment. We use the Monte Carlo routines ISAJET [43], versions 7.16 and 7.20, and a combination of PYTHIA [44] version 6.157 and MCFM [45] to generate all SM backgrounds. PYTHIA version 6.157 is used to generate all signal processes. Once we have generated the final state particles from the Tevatron, we model the response of the CDF detector using the detector simulation QFL, discussed in Section 2.2.7.

We use signal and background Monte Carlo samples to optimize the analysis cuts and evaluate the systematic uncertainties from the values of the cuts before looking at the data. In the LSD analysis, we optimize the cuts with the goal of defining a signal region with low SM background, while retaining acceptance for the $\ell^{\pm}\ell^{\pm} + X$ signal. In addition to Monte Carlo samples, we can use regions of the data which have already been excluded from the signal region by

other cuts, called "sidebands," to evaluate the effectiveness of a given cut or to estimate the amount of expected background or signal in the signal region. Sidebands are especially necessary to estimate contributions to the signal region from backgrounds which are not well-modeled by the Monte Carlo simulations.

CHAPTER 2

Apparatus

Deus ex machina. [46]

The Fermi National Accelerator Laboratory (Fermilab) Tevatron is a proton-antiproton ($p\bar{p}$) particle accelerator and collider [47]. The Collider Detector at Fermilab (CDF) is a forward-backward and azimuthally symmetric solenoidal particle detector situated around one of the Tevatron's beam interaction regions [48, 49]. This chapter describes the Fermilab Run I iteration of the Tevatron and CDF detector, with which the data for this analysis were taken. For Fermilab Run II, both the Tevatron [50] and CDF [51, 52] underwent significant upgrades.

2.1 The Tevatron

The Fermilab Tevatron separately accelerates proton and antiproton beams to $0.99944c$ in order to collide them with a center-of-mass energy ($\sqrt{s}$) of 1.8 TeV. The first stage of the process is the Cockcroft-Walton, essentially a giant capacitor. In the Cockcroft-Walton hydrogen gas is ionized by adding an extra electron to form H^-. The H^- ions are electrostatically accelerated to 750 keV through a system of voltage dividing diodes. The H^- ions exit the Cockcroft-Walton in approximately $1.4 \text{x} 10^{14}$ H^- ion bunches. The H^- bunches are then injected into the Linear Accelerator (LINAC). Figure 2.1 shows the Run I accelerator complex

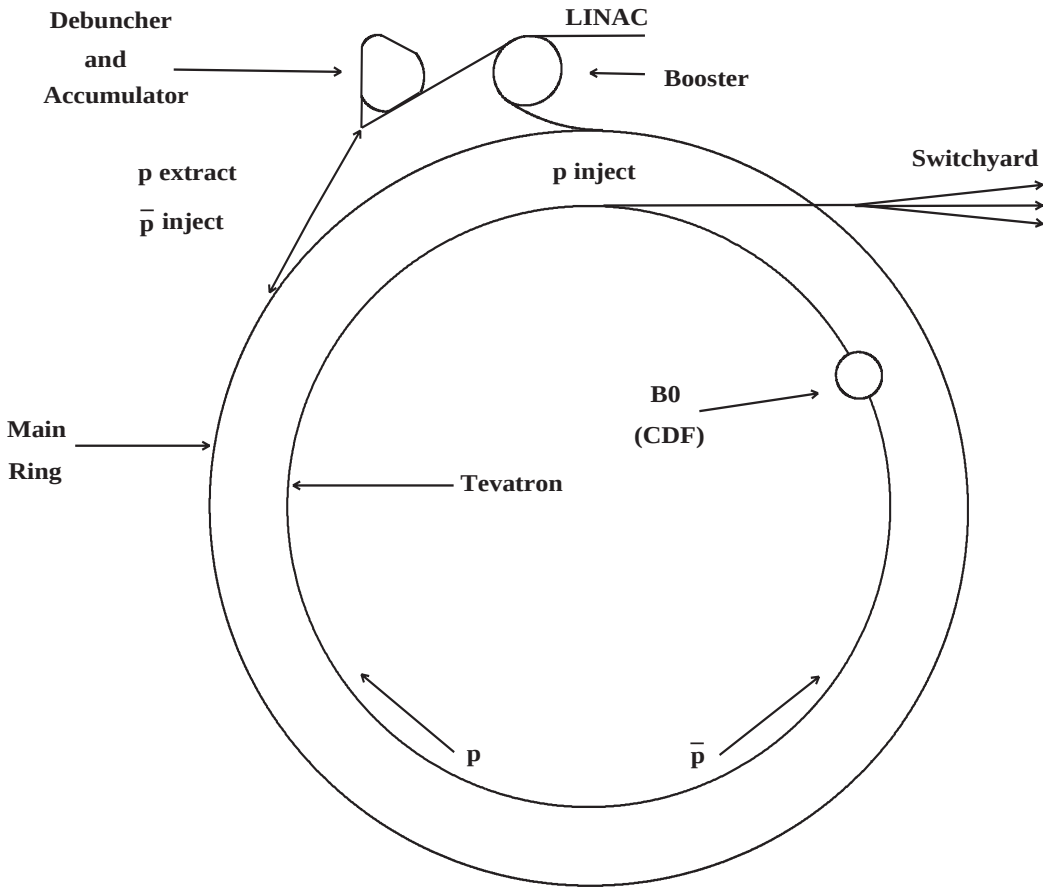

Figure 2.1: Overview of the accelerator complex at Fermilab.

starting from the LINAC.

The LINAC is a series of nine radio-frequency (RF) cavities separated by RF-shielded drift tubes. The RF cavities accelerate the bunches by producing a electric field that rapidly changes direction. When the H^- ions are in the cavities the force of the field acting on the ions accelerates them; when the force of the field would decelerate the ions they move through the RF-shielded drift tubes. The cavities increase in length along the LINAC to provide acceleration to the

ions along the entire 150 meter length of the device. The H^- ions exit the LINAC with a kinetic energy of 400 MeV.

Before entering the Booster a thin carbon foil strips the H^- ions of both electrons as they pass through, leaving only proton (p) bunches. The Booster is a rapid-cycling synchrotron, with a single RF cavity precisely controlled to provide continuous acceleration to the p. The Booster ring has radius 500 m, with conventional magnets to focus and steer the beam and the RF cavity that accelerates the p. Exiting the Booster, bunches of 10^{10} p, each with 8 GeV of kinetic energy, are injected into the Main Ring.

The Main Ring is a 1 km radius rapid-cycling synchrotron ring with 3.5 kGauss conventional dipole magnets for steering the beam, quadrupole magnets for focusing, and an RF cavity that accelerates the p to 150 GeV before they are injected into the Tevatron. The Tevatron uses superconducting magnets with a 4 Tesla magnetic field, which allows the Tevatron to finally accelerate the p to 900 GeV.

To produce antiprotons ($\bar{p}$), protons from the Main Ring are impinged on a tungsten target at the Antiproton Source. About 20 $\bar{p}$ are produced per million p impinging on the target. A constant magnetic field separates the $\bar{p}$ from the other particles produced in the collision and sends the $\bar{p}$ bunches to the Debuncher. In the Debuncher stochastic cooling tightens the $\bar{p}$ bunches before they are transferred to the Accumulator for storage. When enough $\bar{p}$ are collected they are injected into the Main Ring and accelerated in the direction opposite to the p bunches. Because the $\bar{p}$ have opposite electric charge to the p, the same magnetic field used to bend the p-beam in the Main Ring and Tevatron will bend the $\bar{p}$-beam in the direction opposite to the p bunches. Finally, the $\bar{p}$ bunches are injected into the Tevatron where they reach an energy of 900 GeV.

Quadrupole magnets focus the p and $\bar{p}$ bunches so that they collide at an

interaction point in the center of the CDF and DØ detectors. A typical p bunch contains 2×10^{11} protons, while a typical $\bar{p}$ bunch contains 6×10^{10} antiprotons. Bunch crossings occur every 3.5 μs. Each bunch crossing containing a $p\bar{p}$ collision observed by the CDF and DØ detectors is designated an "event." The collision rate is measured by the Tevatron luminosity,

$$\mathcal{L} \equiv \frac{N_p N_{\bar{p}} N_B f_0}{4\pi\sigma} , \tag{2.1}$$

where N_p is the number of p per bunch, $N_{\bar{p}}$ is the number of $\bar{p}$ per bunch, N_B is the number of bunches, f_0 is the revolution frequency ($\sim$ 50 kHz), and σ is the transverse cross-sectional area of each bunch ($\sim 5 \times 10^{-5}$ cm^2). Usually cross section is expressed in terms of "barns", where 1 picobarn (pb) = 10^{-24} cm^2. During Run IB (August 1994 to December 1995) the typical instantaneous luminosity was $\mathcal{L} \approx 3 \times 10^{31}$ cm^{-2}s^{-1}.

2.2 The Collider Detector at Fermilab

CDF is a forward-backward and azimuthally symmetric solenoidal particle detector situated around one of the Tevatron's interaction points. It is designed to identify many of the types of particles produced in high-energy $p\bar{p}$ collisions. It is cylindrical with the axis of symmetry, the z-axis, pointing in the direction of the incoming p beams. CDF uses a right-handed coordinate system, and the x and y axes point up and radially outward from the center of the Tevatron ring, respectively. CDF then defines a cylindrical coordinate system with polar angle θ measured from the positive z-axis and radial distance r and azimuthal angle ϕ describing the $x - y$ plane. More commonly than θ, CDF uses pseudorapidity,

$$\eta \equiv -\ln(\tan(\theta/2)) . \tag{2.2}$$

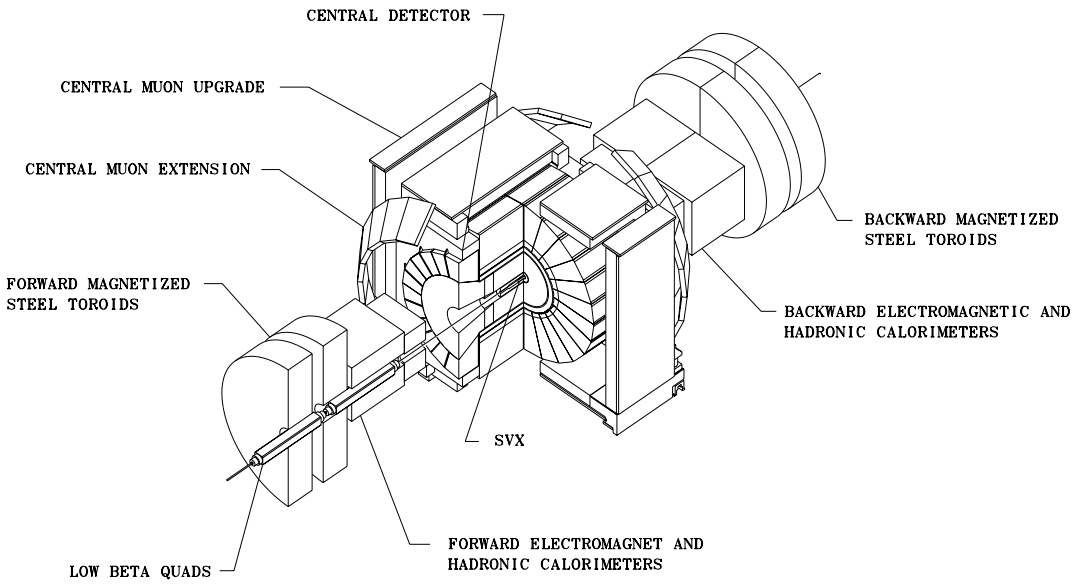

Figure 2.2: Perspective view of the CDF detector.

The advantage of pseudorapidity is that for particles with momentum much larger than their masses (such as those produced by the Tevatron and detected by CDF) the average number of particles per slice of pseudorapidity, $\langle dN/d\eta \rangle$, is constant throughout the CDF detector.

Figure 2.2 shows a 3-dimensional perspective of the detector with one quadrant cut away to reveal the detector components inside. The entire detector is approximately 27 m long, 10 m high, and weighs 5000 tons. Figure 2.3 shows a side view of one quadrant of the detector. From the interaction region outward, the particles in the region $|\eta| < 0.6$ first pass through the Silicon Vertex (SVX) detector. All particles traverse the Vertex Time Projection Chamber (VTX) which measures the event vertex. In the central region of the detector ($|\eta| < 1.1$), they pass through the Central Tracking Chamber (CTC) which measures particle trajectory to obtain momentum and electric charge. Outside the CTC is a solenoid

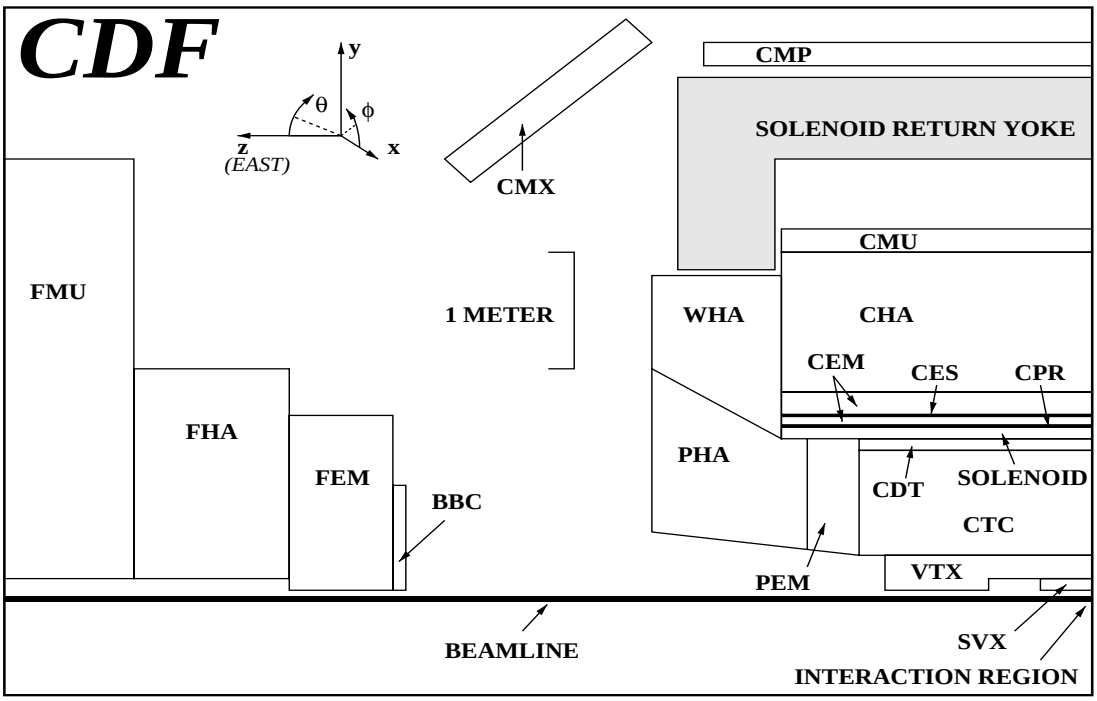

Figure 2.3: Side view of the CDF detector.

magnet which produces a 1.4 Tesla magnetic field perpendicular to the beamline through the SVX, VTX, and CTC.

Outside the solenoid are the Central Electromagnetic (CEM) and Central and Wall Hadronic (CHA and WHA) calorimeters which measure deposited energies from electron and photon candidates. In the case of a muon or other penetrating particle, the Central Muon Chambers (CMU/CMP/CMX) reside outside the central calorimeters to identify muon candidates. Outside the central region ($|\eta| > 1.1$), the particles pass through the plug and forward detector subsystems. The Plug Electromagnetic (PEM) and Plug Hadronic (PHA) calorimeters have the same function as the central calorimeters. These systems are described in detail in the following sections.

Most particles which traverse the plug and forward regions of the detector do

not first pass through much of the CTC. Because the CTC cannot measure well the momentum and electric charge of those particles, the LSD analysis, which relies on good charge identification, uses the plug detectors only for first-stage lepton identification and does not use the forward regions of the CDF detector, including the Forward calorimeter (FEM and FHA) and Forward muon (FMU) systems. These systems are described in detail elsewhere [48].

CDF can detect and measure only those particles which have some component of their momenta transverse to the beamline. In each $p\bar{p}$ collision the interacting particles are the constituent quarks which comprise the p (uud) and $\bar{p}$ ($\bar{u}\bar{u}\bar{d}$). The quarks are allowed to move inside the p or $\bar{p}$. This motion causes an uncertainty in the momenta of the quarks prior to the collision in the direction of motion of the p and $\bar{p}$: the z-axis. This smearing in p_z introduces a systematic error in measuring the total momentum produced in each collision. Thus, we work with transverse energy and momentum, which are independent of this effect,

$$\begin{aligned} E_T &\equiv E \times \sin\theta \\ p_T &\equiv p \times \sin\theta \ , \end{aligned} \tag{2.3}$$

where E is energy measured in the calorimeters and p is momentum measured by the CTC.

2.2.1 Vertex Time Projection Chamber

The Vertex Time Projection Chamber (VTX) is used to reconstruct the event vertex position. The vertex position is important for lepton track reconstruction in the CTC and measurement of E_T. The VTX extends 1.4 m from either side of the nominal interaction region at the center of the detector with $|\eta| < 3.25$. It surrounds the SVX detector and has an inner radius of 7 cm and an outer radius of 22 cm.

The VTX consists of 8 octagonal chambers in ϕ placed along the beamline. The chambers use 50/50% argon-ethane gas mixture and a high-voltage grid with a 320 V/cm longitudinal electric field which divides the chamber into two oppositely directed drift regions, each about 5 cm long. The drift direction is along the z-axis with a drift velocity of 46 μm/ns and a maximum drift distance of 15.25 cm. The maximum drift time is less than the 3.5 μs timing between $p\bar{p}$ bunch crossings. Ionization electrons drift to the endcaps of each chamber, where 24 azimuthally-strung sense wires in each octant measure the position of the hit. The resolution of the z vertex measurement is ± 2 mm.

2.2.2 Central Tracking Chamber

The Central Tracking Chamber (CTC) lies just outside the VTX and inside the 1.4 T solenoidal magnet (the magnetic field is uniform to $\approx 1\%$). It is a cylindrically symmetric open-wire drift chamber that provides tracking out to $|\eta| \sim 1$. The CTC is 3.2 m long and has radial coverage $31 < r < 1325$ cm. Wires are strung along the z-direction between endplates at $z = \pm 1.6$ m.

There are 84 layers of sense wires divided into 5 axial and 4 stereo "superlayers" in an argon-ethane-ethanol gas mixture (49.6/49.6/0.8%). The axial superlayers are composed of 12 radially separated layers of wires that run parallel to the z-axis and provide $r-\phi$ hit information. The stereo superlayers are composed of 6 wires per layer, rotated approximately 3 degrees from the z-axis. Axial and stereo hit information is combined to reconstruct 3-dimensional tracks.

Charged particles that pass through the 1.4 T magnetic field of the solenoid follow a helical trajectory of which the curvature determines the momentum and electric charge of the particle. The momentum resolution of a beam-constrained track in the CTC is $\delta p_T/p_T = 0.001 \times p_T/\mathrm{GeV}/c$.

2.2.3 Central Electromagnetic Calorimeter

The Central Electromagnetic calorimeter (CEM) covers $|\eta| < 1.1$ and is split into two equal halves covering positive η (east) and negative η (west). Each half is divided into 24 wedges, and each wedge covers 15° in ϕ and 1.1 in η. Each wedge is broken into towers each covering $\eta = 0.1$. Where the east and west calorimeters meet there is a dead area between them approximately 8 cm wide, which is known as the 90° crack.

Each CEM wedge consists of 31 layers of 5mm thick plastic scintillator interleaved with 30 layers of $\frac{1}{8}$ inch lead absorber sheets. Light guides collect the light from the scintillator and direct it to photomultiplier tubes (PMTs). There are two PMTs per tower. The amplified pulse height from the PMT is proportional to the amount of energy deposited by an electromagnetic shower in the calorimeter.

The CEM is about 18 radiation lengths (X_0) thick. A single radiation length is the distance in which a high-energy electron loses all but $1/e$ of its energy. In each wedge, a proportional strip chamber, the Central Electromagnetic Shower (CES) detector, is inserted between the eighth layer of lead and the ninth scintillator layer. This corresponds to six X_0, which is where the electromagnetic shower is expected to deposit its maximum energy. The CES gives position information about the shower, both z and $r - \phi$, with a resolution in each view of ± 2 mm. Figure 2.4 shows the $\eta - \phi$ segmentation of the CDF calorimeters.

2.2.4 Central and Wall Hadronic Calorimeters

The Central and Wall Hadronic Calorimeters (CHA and WHA) are located outside the CEM and are similar in structure to the CEM. The same tower

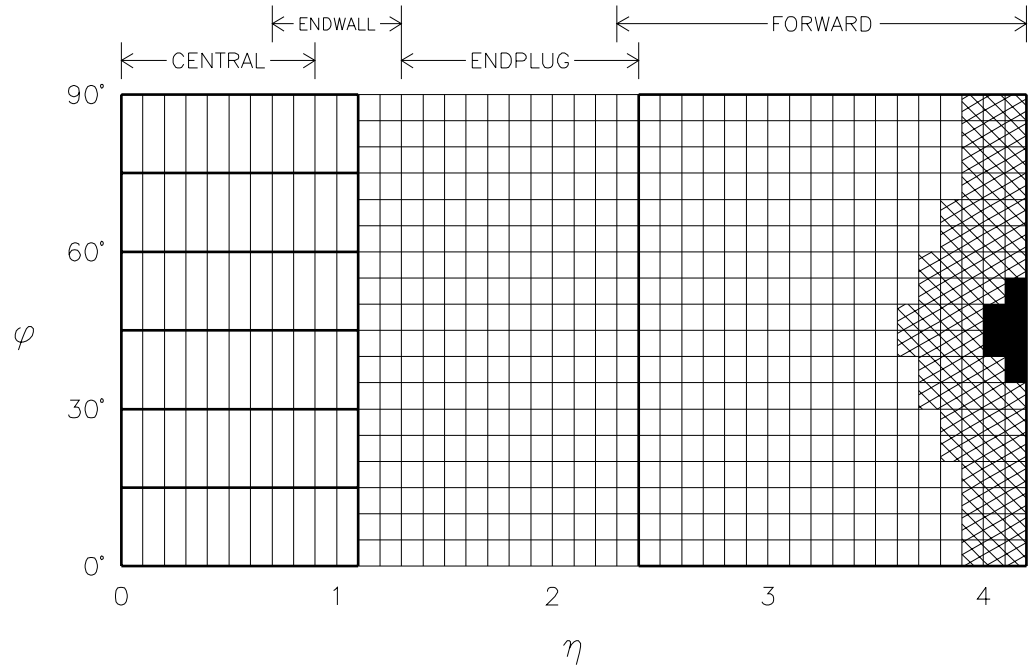

Figure 2.4: The $\eta - \phi$ segmentation of one quadrant of the east half of the CDF detector calorimeters. The central region used in the LSD analysis is $|\eta| < 1.1$ where the calorimeters are segmented $(\Delta\eta = 0.1) \times (\Delta\phi = 15°)$.

structure is used, but steel is used as the absorber material in place of lead. The CHA covers the region $0.0 < |\eta| < 0.9$ and has 32 layers of 2.5 cm thick steel absorber sandwiched with layers of 1 cm thick plastic scintillator. It is about 4.7 interaction lengths (λ_0) thick. The WHA covers $0.7 < |\eta| < 1.3$. It has 15 layers of 5.1 cm thick steel sandwiched with 1 cm thick plastic scintillator for about 4.5 λ_0.

PMTs read out the scintillator light pulses from the hadronic calorimeters. The amplified pulses also trigger a discriminator pulse. Hadron Time-to-Digital Converters (HTDCs) inside the calorimeters measure the time elapsed between this discriminator pulse and a common stop signal. The HTDCs have a range of

System	η Coverage	Energy Resolution	Thickness
CEM	$\lvert\eta\rvert < 1.1$	$13.7\%/\sqrt{E_T} \oplus 2\%$	18 X_0
CHA	$\lvert\eta\rvert < 0.9$	$50\%/\sqrt{E_T} \oplus 3\%$	4.7 λ_0
WHA	$0.7 < \lvert\eta\rvert < 1.3$	$75\%/\sqrt{E_T} \oplus 4\%$	4.5 λ_0
PEM	$1.1 < \lvert\eta\rvert < 2.4$	$22\%/\sqrt{E_T} \oplus 2\%$	19 X_0
PHA	$1.3 < \lvert\eta\rvert < 2.4$	$106\%/\sqrt{E_T} \oplus 4\%$	5.7 λ_0

Table 2.1: Properties of the CDF calorimeters. The symbol $\oplus$ indicates that the constant term is added in quadrature to the resolution. λ_0 signifies interaction lengths and X_0 radiation lengths. Adapted from [53].

700 ns and resolution of ± 0.5 ns, and are used to identify cosmic ray muons.

2.2.5 Plug Calorimeters

The Plug Electromagnetic Calorimeter (PEM) is multi-wire gas (argon-ethane) proportional system, segmented into 72 ϕ wedges of 5° each. The PEM covers $1.1 < |\eta| < 2.4$ in $\eta = 0.1$ towers. It contains 34 gas proportional tube arrays interleaved with 2.7 mm thick steel absorber sheets, totalling about 19 X_0 thick.

The Plug Hadronic Calorimeter (PHA) has 20 layers of 5.1 cm thick steel alternating with gas proportional tubes. It covers $1.3 < |\eta| < 2.4$ with identical segmentation as the PEM. The PHA is about 5.7 λ_0 thick. Table 2.1 summarizes the properties of the CDF calorimeters.

2.2.6 Central Muon Chambers

The CMU is outside the CHA and consists of 4 layers of drift chambers covering $|\eta| < 0.6$. Only muons and a small number of punch-throughs from energetic

jets can survive the large number of interaction lengths between the nominal interaction region and the CMU. Muons must have $p_T > 1.4$ GeV/c to reach the CMU. The Central Muon Upgrade (CMP) is another set of 4 drift chambers that are outside the CMU. Between the CMU and CMP is an additional 60 cm of steel absorber (8 λ_0), which helps reduce the rate of non-muon punch-throughs being misidentified as muon candidates.

The Central Muon Extension (CMX) consists of four-standing conical arches and covers $0.6 < |\eta| < 1.0$. The arches contain drift chambers, to detect muons, between scintillators that are used for triggering. The CMX has a 90° gap at the bottom of the detector where it intersects the floor and a 30° gap at the top of the detector where the Main Ring and solenoid refrigerator are located. Figure 2.5 shows the $\eta - \phi$ coverage of the CMU, CMP, and CMX chambers.

2.2.7 CDF Detector Simulation

QFL is a software package that simulates the CDF detector. It includes detector effects such as smearing and resolution. We use QFL version 3.48 [54] in both the estimates of expected number of background events generated with ISAJET or PYTHIA and the estimates of acceptance for signal events generated with PYTHIA. QFL, in general, accurately reproduces the results from test-beam studies. However, it does not model the HTDCs at all, and tends to be over-efficient when modeling the detector efficiency to identify leptons. Thus, we compare information from each detector subsystem in CDF Run IB data to events generated using ISAJET version 7.20 and simulated using QFL version 3.48 and to find a correction factor, C_{QFL}, to be applied to Monte Carlo estimates. The individual detector correction factors are shown in Table 2.2.

For the LSD analysis, we weight a selected event from Monte Carlo by the

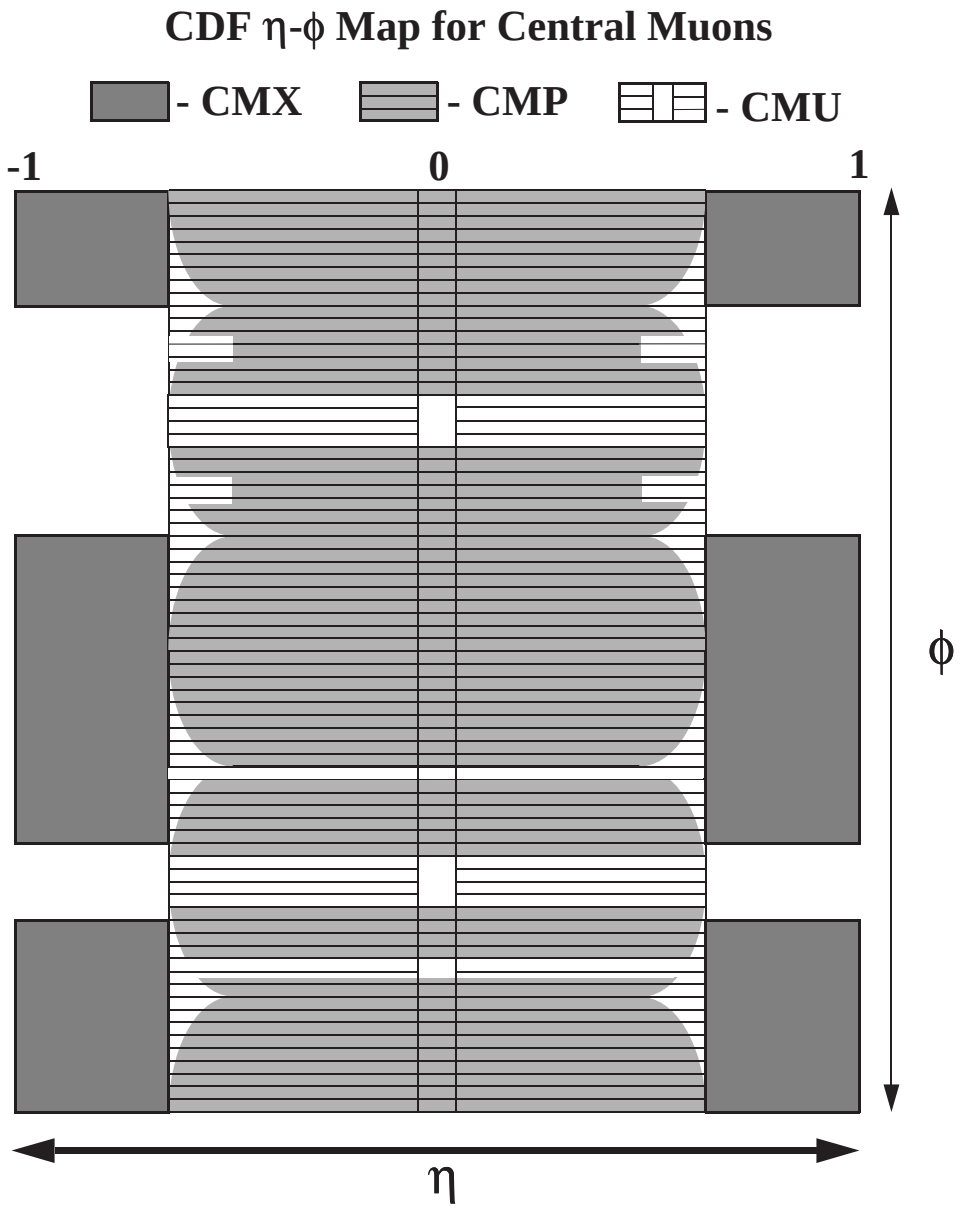

Figure 2.5: $\eta - \phi$ muon coverage for the central region of the CDF detector.

detector	MC efficiency	data efficiency	data/MC
CEM	0.867±0.004	0.819±0.008	0.945±0.010
PEM	0.924±0.004	0.920±0.007	0.996±0.009
CMU/CMP	0.978±0.003	0.929±0.007	0.950±0.008
CMX	0.972±0.005	0.929±0.010	0.956±0.011

Table 2.2: Summary of QFL efficiencies for lepton identification. Adapted from Ref. [55].

detector correction factors of each of the two like-sign leptons, $\ell 1$ and $\ell 2$, used to identify the event:

$$C_{QFL} \equiv (\text{data/MC})_{\ell 1} \times (\text{data/MC})_{\ell 2} \ . \tag{2.4}$$

For example, an $e\mu$ Monte Carlo event, where the electron was identified in the CEM and the muon in the CMX, receives the weight $C_{QFL} = 0.903 \pm 0.014$. The factor C_{QFL} is applied to both Monte Carlo signal and background events. After the events generated with ISAJET or PYTHIA are simulated with QFL, they are identical in structure to data taken with the detector.

2.2.8 Trigger

CDF uses a three level trigger system to determine whether data in the various CDF detector systems from a given $p\bar{p}$ collision should be written to tape. Each successive level of trigger is more sophisticated than the previous and requires more time to reach a decision.

The Level 1 trigger is composed of fast electronics that separately process the output of several individual subsystems to determine if some basic requirement is met (*e.g.* a minimum amount of electromagnetic energy deposited in

the calorimeter or number of hits detected in the muon chambers). The Level 1 trigger decides whether to pass the event to the next trigger level before the next bunch crossing occurs every 3.5 μs. In Run 1B the Level 1 trigger rate was approximately 1 kHz.

The Level 2 trigger takes approximately 20 μs to make a decision. During this time $\sim$ 6 bunch crossings are ignored by the detector. Level 2 is a fast electronic processor trigger like Level 1, but it combines requirements from different subsystems. Calorimeter data is used to find clusters of towers with energy above threshold, and fast timing signals from the CTC are used in conjunction with a hardware track processor, the Central Fast Tracker (CFT), to find simple 2-dimensional tracks. A look-up table gives the particle momentum with a resolution of $\delta p_T \approx 0.035 \times p_T$. For example, a typical electron Level 2 trigger might require both a cluster with E_T above some threshold and a CFT track with some minimum p_T. Muon Level 2 triggers require CFT tracks that are matched to hits in the muon chambers.

Some types of events occur frequently enough relative to the maximum rate that the trigger can accept that a Level 2 trigger must be "prescaled" to accept one of every N events that would have normally passed that trigger. This allows events that occur less frequently than the high-rate events, but that may be just as interesting, to be recorded to tape. Prescaling can be either static (fixed for an entire entire data taking run) or dynamic (changed during the course of the run depending on the instantaneous luminosity).

Events which pass the Level 2 trigger system are completely read out and processed in more detail at Level 3. The Level 3 trigger is a software trigger that uses a farm of Silicon Graphics processors to reconstruct and examine the full event. The CFT and hardware calorimeter cluster data are dropped in favor of

the full CTC tracking code and offline calorimeter clustering routines. Events passing the Level 3 trigger were written to tape at a rate of $\sim$ 10 Hz.

2.2.9 Trigger Monte Carlo

The QFL package discussed in Section 2.2.7 does not include a simulation of the trigger. Events in the final dataset can follow any one of many trigger paths, passing different triggers at Levels 1, 2, and 3. We use the standard CDF Run I routine MC_WGT to simulate the trigger efficiency of the Monte Carlo events generated with ISAJET and PYTHIA and simulated with QFL. MC_WGT returns three probabilities, each one for a Monte Carlo event to have passed one of the three trigger levels. We multiply the three separate probabilities to get the overall trigger efficiency for an event:

$$W_{trig} \equiv \mathrm{P}_1 \times \mathrm{P}_2 \times \mathrm{P}_3 \ , \tag{2.5}$$

where the P_i are the probabilities for an event to pass a Level i trigger. We weight both Monte Carlo signal and background events with W_{trig}.

2.2.10 Beam Beam Counters

Luminosity at CDF is measured using Beam-Beam Counters (BBC). The BBC are two planes of scintillation counters covering the angular range of 0.32° to 4.47° in both the forward and backward directions ($3.24 < |\eta| < 5.88$). Hits in both counters that coincide (to within the detector resolution of about 200 ps) with particle bunches crossing the detector interaction point serve as both a minimum bias trigger (a trigger with no requirements whatsoever in the rest of the CDF detector) and the primary luminosity monitor. The rate of coincidences in these counters divided by the effective σ of the counters provides

a measurement of the instantaneous luminosity, $\mathcal{L}$, defined in Section 2.1. The integrated luminosity, $\int \mathcal{L}\ dt$, is calculated similarly using the total number of coincidences in these counters instead of coincidence rate. The entire Run I (1992-95) integrated luminosity collected by CDF is 107 pb^{-1}.

CHAPTER 3

Analysis

There are more things in heaven and earth, Horatio,
Than are dreamt of in our philosophy. [56]

As discussed in Section 1.3.1, the LSD analysis is an inclusive search for physics beyond the SM. We define a signal region containing less than one event from SM processes. To reduce SM background in the signal region while maximizing sensitivity to non-SM processes, we search for dilepton events with the final state $\ell^{\pm}\ell^{\pm} + X$ using a minimal number of analysis cuts. We select candidate LSD events from 107 pb^{-1} of data collected by CDF during Run I.

3.1 Event Selection

The events written to tape out of the CDF L3 trigger are stored in a series of data structures called "banks." Each event contains many banks; for example, each electron candidate in an event has an associated ELES bank, each track has a TRKS bank. These banks hold all of the information about their associated object. The LSD analysis uses the ELES, CMUO, and TRKS banks from which we select e, μ, and track candidates.

3.1.1 ELES Banks

The energy of an electron candidate is reconstructed from the sum of the energies measured in a cluster of towers in the CEM. Each tower energy is the geometric mean of the charge from the two PMTs in the tower, converted from PMT counts to MeV by a conversion factor. The tower with the largest E_T is designated the "seed" tower of the cluster. The two towers on either side of the seed tower in z, called the "shoulder" towers, are included in the cluster, and the sum of the EM energy in the seed and shoulder towers is the energy of the electron candidate. Clusters are identified down to a seed tower energy threshold of 5 GeV. Each cluster has an associated ELES bank.

3.1.2 CMUO Banks

A muon candidate is identified in the CMU, CMP, and CMX drift chambers. The muon is located in the drift chambers by a time-to-distance relationship in the ϕ direction and a charge distribution in the z direction. We require a coincidence of multiple separate layers in the drift chamber that are aligned relative to each other within the detector resolution: 250 μm in r and 1.2 mm in z) in both the $r-\phi$ and $r-z$ planes. Such an alignment is called a muon "stub." The stubs are matched with a track extrapolated from the CTC. Each stub and track pair is an muon candidate and has an associated CMUO bank.

3.1.3 TRKS Banks

A track is identified by multiple hits in the detectors built to measure the passage of a charged particle: SVX, VTX, and CTC. A three-dimensional fit is performed to the hits and that fit is extrapolated to the various energy depositions

in the EM and HAD calorimeters and muon drift chambers. Each track has an associated TRKS bank.

3.1.4 Dilepton Dataset

During Run I data taking, events with two leptons passing the L3 Exotic Dilepton trigger (COMBINED_EXOB_DIL) were written to the XDLB_5P tapes, a series of 56 data tapes. The L3 Exotic Dilepton trigger requires at least one central lepton ($|\eta| < 1$) candidate with $p_T > 8$ GeV/c and at least one other lepton candidate anywhere in the detector with $p_T > 3$ GeV/c. The XDLB_5P tapes were further searched for events with at least one central electron candidate passing the tight electron identification (ID) cuts shown in Table 3.1 or at least one central muon candidate in the CMU or CMP passing the tight muon ID cuts shown in Table 3.2. Then, at least one other electron anywhere in the detector passing the loose electron ID cuts listed in Table 3.1 or at least one muon anywhere in the detector passing the loose muon ID cuts listed in Table 3.2 was required to select the dilepton event. After this selection, we are left with a dilepton dataset on disk with 457,478 events.

3.1.5 Electron ID Cuts

Table 3.1 lists the electron ID cuts used to select electron candidates for the dilepton dataset in either the CEM or PEM. The difference between the PEM and CEM cuts are primarily due to the lack of tracking for PEM electrons.

The variables E_T and p_T are the electron energy and momentum, respectively, transverse to the beamline as defined in Section 2.2. To measure p_T requires a good track with a well-defined curvature, making a p_T cut in the PEM impossible. A small E/p, the ratio of the electron energy to its momentum, distinguishes

Variable	Tight	Loose	
	CEM	CEM	PEM
p_T (GeV/c)	≥ 6.0	≥ 2.8	–
E_T (GeV/c^2)	≥ 8.0	≥ 4.0	≥ 4.0
E/p	≤ 2.0	≤ 2.0	–
HAD/EM	≤ 0.05	$\leq 0.055 + 0.045(\frac{E}{100})$	≤ 0.1
L_{shr}	≤ 0.2	≤ 0.2	–
$\lvert\Delta x\rvert$ (cm)	≤ 3.0	≤ 3.0	–
$\lvert\Delta z\rvert$ (cm)	≤ 5.0	≤ 5.0	–
χ^2_{strip}	≤ 10.0	≤ 15.0	–
$\chi^2_{3\times3}$	–	–	≤ 3.0
VTX occupancy	–	–	≥ 0.5

Table 3.1: Identification criteria for CEM and PEM electrons.

electrons from heavier mesons such as pions depositing energy in the calorimeter (for a complete list of SM particles, see Ref. [4]). The ratio of the energy deposited in the hadronic calorimeters to the energy deposited in the electromagnetic calorimeters is HAD/EM. A good electron should deposit almost all of its energy in the electromagnetic calorimeter, so we require a small value of HAD/EM.

The variable L_{shr} is the transverse profile of the electromagnetic shower. It compares the lateral sharing of energy in the calorimeter towers of an electron cluster to electron shower shapes from test beam data:

$$L_{shr} \equiv 0.14 \frac{E^{adj} - E^{exp}}{\sqrt{0.14^2 E + (\Delta E^{exp})^2}} \ , \tag{3.1}$$

where E^{adj} is the measured energy in GeV in a tower adjacent to the seed tower,

E^{exp} is the expected energy in GeV in the adjacent tower based on test-beam data, $0.14\sqrt{E}$ is the error on the energy measurement, and ΔE^{exp} is the error on the expected energy estimate. The quantities $|\Delta x|$ and $|\Delta z|$ match the CTC track to the calorimeter cluster that makes an electron candidate, where $|\Delta x|$ is the distance between the cluster position and the extrapolated track in cm in the $r-\phi$ plane and $|\Delta z|$ is the distance in cm in the z direction.

The chi-square χ^2_{strip} quantifies the comparison of the calorimeter pulse height to the test beam data for each of the 11 strips per CEM chamber in z. The chi-square $\chi^2_{3\times3}$ quantifies the shape of the lateral sharing of energy in the calorimeter towers in the 3×3 array of towers in $\eta-\phi$ around the seed tower fit to the shape expected from test beam data [57]. It is applied to PEM electrons in place of the L_{shr} cut. VTX occupancy is the ratio of layers in the VTX detector where the electron deposits charge to the expected number of layers where the electron should have deposited charge based on its trajectory. This ensures the presence of a charged track in an event with a PEM electron candidate, even though the track cannot be extrapolated to the cluster.

3.1.6 Muon ID Cuts

Table 3.2 lists the muon ID cuts used to select muon candidates for the dilepton dataset in either the CMU, CMP, or CMX.

As defined in Section 2.2, p_T is the muon momentum transverse to the beamline. EM and HAD are the energies deposited by the muon candidate in the electromagnetic and hadronic calorimeters, respectively. A good muon candidate should deposit almost no energy in the calorimeters, so we require small values of these energies. A small value of d_0, the SVX impact parameter, requires the muon to originate from near the nominal interaction region. The matching cuts

Variable	Tight	Loose
	CMU/P	CMU/P or CMX
p_T (GeV/c)	≥ 7.5	≥ 2.8
EM (GeV)	≤ 2.0	≤ 2.0
HAD (GeV)	≤ 6.0	≤ 6.0
d_0 (cm)	≤ 0.5	≤ 0.8
CMU matching	$\lvert\Delta x\rvert \leq 2$ cm or $\chi^2_{CTC} \leq 9$	$\lvert\Delta x\rvert \leq 2$ cm or $\chi^2_{CTC} \leq 9$
CMP matching	$\lvert\Delta x\rvert \leq 5$ cm or $\chi^2_{CTC} \leq 9$	$\lvert\Delta x\rvert \leq 5$ cm or $\chi^2_{CTC} \leq 9$
CMX matching	–	$\lvert\Delta x\rvert \leq 5$ cm or $\chi^2_{CTC} \leq 9$

Table 3.2: Identification criteria for CMU, CMP, and CMX muons.

require good alignment between the extrapolation of the CTC track and the muon stub. $|\Delta x|$ is the distance in cm between the track and stub in the $r-\phi$ plane and χ^2_{CTC} is the chi-square that quantifies a fit from the CTC track to the muon stub. We require the OR of the $|\Delta x|$ and χ^2_{CTC} cuts to increase the number of well-matched muons. For complete details of the dilepton dataset selection and ID cuts, see Ref. [58].

3.1.7 Event Quality Cuts

The LSD analysis further improves the event selection from the dilepton dataset with several general requirements on event quality and the quality of the leptons in each event. To ensure that both leptons in each dilepton event are well-measured, charged leptons, we select the two highest-p_T leptons in the event and require that they both satisfy the tight lepton ID cuts listed in Tables 3.1 and 3.2. This requirement forces all leptons in the event to be in the central part of the detector, ensuring a good measurement of the lepton charge (Q).

Cut	Number of Events		
	$e^{\pm}e^{\pm}$	$e^{\pm}\mu^{\pm}$	$\mu^{\pm}\mu^{\pm}$
$Q_1 \times Q_2 = 1$	6,437	28,315	34,918
Bad run = false	6,101	26,697	33,105
$\lvert z_{vertex}\rvert < 60$ cm $\lvert z_{lepton} - z_{vertex}\rvert < 5$ cm	5,654	25,226	31,532
Fiducial = true	4,432	22,680	31,532
Conversion = false	2,545	17,126	31,532
Cosmic = false	2,545	17,123	31,330
Muon hitmask	2,545	9,770	9,428

Table 3.3: Number of events surviving each dilepton event quality cut.

With two leptons of well-measured Q, we apply the like-sign (LS) requirement: $Q_1 \times Q_2 = 1$. We identify the two highest-p_T leptons with LS charges as the LSD pair. After this selection, we are left with a LSD dataset with 69,670 events divided into 6,437 $e^{\pm}e^{\pm}$, 28,315 $e^{\pm}\mu^{\pm}$, and 34,918 $\mu^{\pm}\mu^{\pm}$ events. The disparity in number of μ and e events is due to the difference in identification of electrons and muons.

Some of the remaining events are from data later identified as bad. Reasons for bad data include hardware malfunctions in the detector or poor beam conditions during physics data taking. We use the standard CDF routine BADRUN [59] to check the data quality during a given data run. BADRUN queries a database and returns a bit marking certain data runs bad. These are removed from the LSD dataset, leaving 65,903 total events. The removal of events from this and the following quality cuts is summarized in Table 3.3.

As discussed in Chapter 2, the VTX measures the distance of the $p\bar{p}$ col-

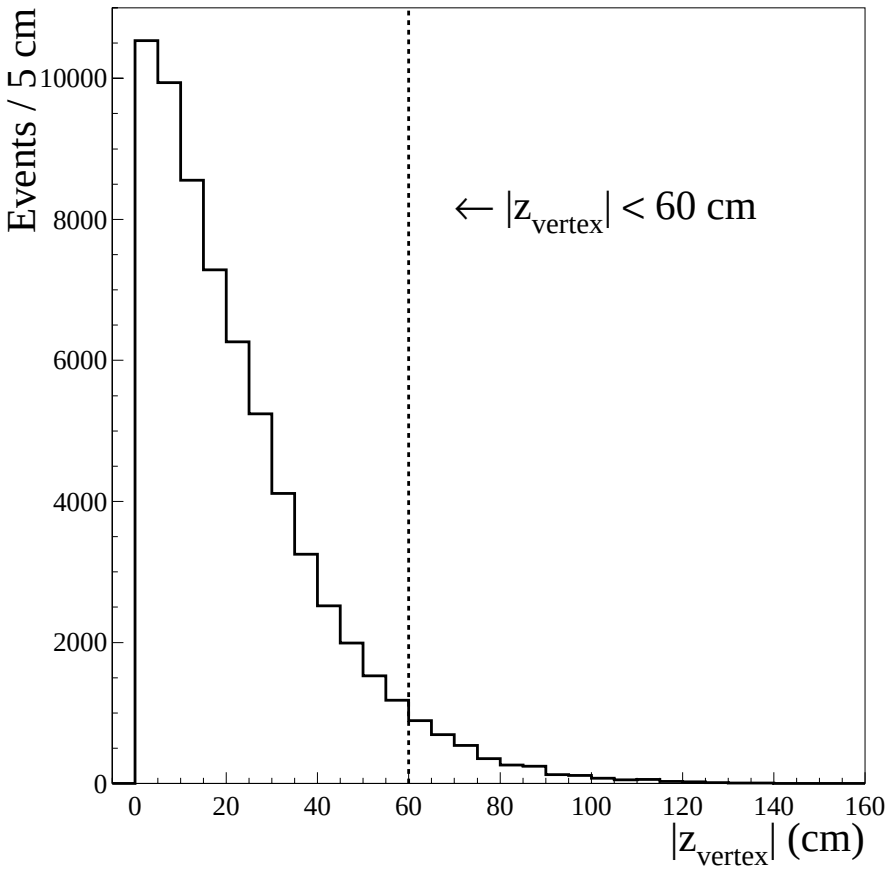

Figure 3.1: Distribution of $|z_{vertex}|$. The $|z_{vertex}| < 60$ cm cut is marked by the dashed line.

lision event vertex (z_{vertex}) from the center of the detector along the z axis. To ensure that the track for each lepton is well-extrapolated to the calorimeters and drift chambers, we require $|z_{vertex}| < 60$ cm. We further require that $|z_{lepton} - z_{vertex}| < 5$ cm for each lepton, to ensure that both leptons came from the same primary collision. Figure 3.1 shows the z_{vertex} distribution prior to applying these cuts.

We require that each electron is in a region of the calorimeter known to

function well, called the "fiducial area." We use the standard CDF routine FIDELE [60], which returns a bitmap containing information on the electron location. We remove any events where either of the LSD pair is an electron outside the fiducial area. We also remove electrons which originate from photon conversions inside the detector. We use the standard CDF routine CONFND [61], which checks for two opposite-sign tracks pointing to an electron cluster indicating the presence of a photon conversion. We remove any events where either of the LSD pair electrons is identified as resulting from a conversion.

Cosmic ray muons constantly pass through the CDF detector. They appear as back-to-back opposite-sign (OS) charged tracks in the CTC with matched muon stubs in the muon drift chambers. Because the event appears to be an OS pair, we do not expect a cosmic ray muon to be identified as a LS dimuon pair. However, if there is an actual lepton in the event, one "leg" of the cosmic ray muon can be identified together with the lepton as a LSD event. Thus, we search each LSD event for a third muon with OS charge relative to the charge of the LS dilepton pair. We then match this third OS-charged muon to either of the LSD leptons if they are muons using the CDF cosmic ray filter DIMUCOS [62]. DIMUCOS identifies a cosmic ray muon from a muon pair with 99.1% efficiency. We reject all events which DIMUCOS identifies as cosmic rays.

Finally, we require that if a muon candidate is identified in a region of the detector where the muon drift chambers overlap, for example, where both the CMU and CMP are present (see Fig. 2.5), then there must be muon stubs in *all* of the muon detectors present in that region. We use the standard CDF routine CMUSWM [63], which applies a muon detector hitmask, to check each muon in the LSD pair. We remove any events where the hitmask is not satisfied. After these selections we are left with a total of 21,743 LSD candidate events.

3.2 LSD Backgrounds

In LSD analysis we search for dilepton events with the final state $\ell^{\pm}\ell^{\pm} + X$. In LSD candidate events each lepton candidate can be selected from two sources: real leptons and "fake" leptons, *i.e.* a hadronic jet [64] or other non-leptonic object in the event which passes all of the lepton ID cuts defined in Sections 3.1.5 and 3.1.6 and is thus misidentified as a lepton candidate. Thus, LSD backgrounds can be discussed in three major categories: (1) background from SM processes that yield two real LS leptons in an LSD signature event, (2) background from one real lepton from SM processes and one fake lepton which passes the LSD selection criteria, and (3) background from two fake leptons. Several SM processes yield two real LS dileptons to create "dilepton" background: diboson production ($W^{\pm}Z^0$ and Z^0Z^0) and heavy flavor production ($t\bar{t}$ and $b\bar{b}$).

The largest source of LSD background comes from events with no real LS dilepton pair, but with at least one real lepton and one fake lepton with the same charge as one of the real leptons. Drell-Yan γ^*/Z^0, J/ψ and Υ production, and diboson $W^{\pm}W^{\mp}$ production can each produce a real OS dilepton pair. Either of the real OS leptons can be combined with a fake lepton from a hadronic jet to yield "lepton + fake" background. High-energy jets and tracks in general are produced in an event by higher order processes (*e.g.* gluon radiation) which contribute to the main production process. Low-energy jets are also produced by further collisions in the $p\bar{p}$ collider environment, called "underlying events." A $W^{\pm}$ will produce a single real lepton if the $W^{\pm}$ decays leptonically, which can be paired with a fake lepton from a jet to also yield a lepton + fake LSD event.

Finally, any event with two or more hadronic jets has a small probability of *both* leptons in the LSD analysis being selected from fakes. The primary source of these "difake" events are diffractive QCD dijet events, in which two jets are

produced colinearly along with jets from higher order processes or an underlying event. Any two of the multijets in these events may be misidentified as LS leptons.

3.2.1 $W^{\pm}Z^0$ and Z^0Z^0

Diboson $W^{\pm}Z^0$ and Z^0Z^0 production can each yield at least three real leptons in the final state via the leptonic decays: $W^{\pm} \rightarrow \ell^{\pm}\nu$ and $Z^0 \rightarrow \ell^{\pm}\ell^{\mp}$, which respectively have a 22% and 6.7% decay branching ratio (BR), if $\ell = e$ or μ [4]. Two of the three real leptons can be selected to yield an LSD candidate event. The production cross sections for these two processes at the Tevatron energy scale $\sqrt{s} = 1.8$ TeV are small: $\sigma = 2.5$ pb for $W^{\pm}Z^0$ and $\sigma = 1.0$ pb for Z^0Z^0 [58]. However, as the leptons produced in $W^{\pm}$ Z^0 decays are very similar to LSD signal leptons, we must estimate this background.

We model this background using PYTHIA version 6.157 and MCFM which include off-shell decays of the Z^0. We generate 100,000 $W^{\pm}Z^0$ events with $\int \mathcal{L}\, dt = 1.524 \times 10^6$ pb^{-1} and 100,000 Z^0Z^0 events with $\int \mathcal{L}\, dt = 6.11 \times 10^6$ pb^{-1}. In both cases we force both bosons decay leptonically to e, μ, or τ.

3.2.2 $t\bar{t}$ and $b\bar{b}$

Like $W^{\pm}Z^0$ and Z^0Z^0 production, heavy flavor $t\bar{t}$ and $b\bar{b}$ production result in at least two real LS leptons in an event. The Tevatron produces a large number of b events, making $b\bar{b}$ a substantial background. The large b production cross section, of order 10^6 pb, has been well-measured at both CDF [65] and DØ [66] during Run I of the Tevatron ($\sqrt{s} = 1.8$ TeV). The $b\bar{b}$ background is selected as a result of leptonic decays of the b and $\bar{b}$. For example, typical semi-leptonic

b and $\bar{b}$ decays are:

$$b \to W^{*-}c \to W^{*-}(W^{*+}d) \tag{3.2}$$

$$\bar{b} \to W^{*+}\bar{c} \to W^{*+}(W^{*-}\bar{d}) \tag{3.3}$$

If both $W^{*\pm}$ in either of the same-sign $W^{*\pm}$ pairs in the combined $b\bar{b}$ event decay leptonically, a 4.8% probability, we are left with a $\ell^{\pm}\ell^{\pm}\nu\nu + X$ final state, where X represents the decays of the remaining $W^{*\pm}$, either leptonically or hadronically, and the hadronization into jets of the d and $\bar{d}$ quarks. This final state can be selected as a LSD candidate event.

In addition to leptonic b decays, $B^0 \leftrightarrow \bar{B}^0$ mixing can yield a final state with a LS dilepton pair. The flavor eigenstates, $B^0 = q\bar{b}$, where $q = s$ or d, are produced with a single well-defined flavor. In particular, they originate from $\Upsilon(4S)$ (mass $= 10.5800 \pm 0.0035$ GeV/c^2) production and subsequent decay $\Upsilon(4S) \to B^0\bar{B}^0$ with BR $> 96\%$ [4]. The BR for $B^0 \to \ell^+\nu + X$ and $\bar{B}^0 \to \ell^-\bar{\nu} + X$ is $(10.8\pm0.8)\%$, where the lepton originates in the decay of the b and $\bar{b}$, via the semi-leptonic processes above. Therefore, we should select an OS dilepton pair from $\Upsilon(4S)$ production with final state leptons produced from b and $\bar{b}$ decays. However, the B^0 and $\bar{B}^0$ propagate in electroweak eigenstates, $B^{\pm}$, which are linear superpositions of the B^0 and $\bar{B}^0$. Thus, the B^0 and $\bar{B}^0$ can mix in flight, leading to B^0B^0 or $\bar{B}^0\bar{B}^0$ decaying to a $\ell^{\pm}\ell^{\pm}\nu\nu + X$ final state, which can be selected as a LSD candidate event. The properties of this mixing have been well-measured by the BABAR [67] and BELLE [68] experiments. Because the leptons produced in the $B^0 \leftrightarrow \bar{B}^0$ mixing final state are produced from b and $\bar{b}$ decays, we include this background in the estimate of heavy flavor $b\bar{b}$ background production.

Production of $t\bar{t}$ events is limited by the small t production cross section, $8.2^{+4.4}_{-3.4}$ pb, reported by CDF from Run I data in 1998 [69]. The t quark decays

via $t \to W^+ b$ with a BR of greater than 99% [4]. For this analysis we use the SM predicted top production cross section, as the measured value may contain potential new physics misidentified as top quark production. If the b and $\bar{b}$ quarks, resulting from the decays of the t and $\bar{t}$ respectively, decay via the processes shown above, then we have several permutations from which to select a LS dilepton pair from a $t\bar{t}$ event; the number of permutations grows if the $W^{\pm}$ also decay leptonically. Therefore, a large fraction of the lepton candidates selected from $t\bar{t}$ production will be produced in b quark decays, and will be removable with the same selection cuts as $b\bar{b}$ background. Because of the small $t\bar{t}$ production cross section, we expect that the cuts made to remove the larger $b\bar{b}$ background discussed below are sufficient to remove top production as well.

We model this background using ISAJET version 7.16 with the parton distribution functions CTEQ2L, MRSD0, and GRVLO and ISAJET version 7.20 with the CTEQ3L and GRV94LO parton distribution functions. We generate a total of 2.37M $b\bar{b}$ events summarized in Table 3.4. We include three methods of producing the $b\bar{b}$ pair: direct production from the $p\bar{p}$ collision, and production from either initial or final state gluon radiation. In each generated event, we require at least one b or c quark with $p_T > 10$ GeV/c in $|y| < 4.0$. In the decay products we require either at least one lepton (e, μ, or τ) with $p_T > 9.0$ GeV/c in $|\eta| < 1.5$ region of the detector or two leptons with $p_T > 2.8$ GeV/c in the $|\eta| < 3.0$ region. We generate a total of 125k $t\bar{t}$ events with an $\int \mathcal{L}\, dt = 27{,}308$ pb^{-1}. In the decay products we require at least one lepton of $p_T \geq 7.5$ GeV/c in the $|\eta| \leq 1.5$ region.

3.2.3 $W^{\pm}$ + Jets

The Tevatron copiously produces $W^{\pm}$ events, with a production cross section at $\sqrt{s} = 1.8$ TeV of $\sigma(W \to e\nu) = 2{,}190 \pm 40(\text{stat}) \pm 210(\text{syst})$ pb, reported

Sample ID	Production Mechanism	p_T Range (GeV/c)	Number of Events	$\int \mathcal{L}\, dt$ (pb^{-1})
81	direct	10–25	300k	175.1
82	direct	25–50	400k	348.3
83	direct	50–500	150k	867.7
84	initial state g radiation	10–25	200k	286.1
85	initial state g radiation	25–50	400k	581.2
86	initial state g radiation	50–500	150k	1,075.3
87	final state g radiation	10–25	70k	286.5
88	final state g radiation	25–50	300k	185.7
89	final state g radiation	50–500	400k	499.0

Table 3.4: Summary of $b\bar{b}$ Monte Carlo events. The sample ID number is arbitrary. The p_T range is the allowed p_T of the generated quark.

by CDF in 1991 [70]. Along with the $W^{\pm}$, high-p_T hadronic jets are produced by higher order processes or occasionally in an underlying event. The combination of $W^{\pm}$ and hadronic jet production is called "$W^{\pm}$ + jets." If the $W^{\pm}$ decays leptonically, a lepton may be selected with such a jet misidentified as a lepton as an LSD candidate event [71]. The inclusive production cross section for $W^{\pm}$ + jets events has been well-measured by CDF during Run I of the Tevatron [72]. We model this background with PYTHIA version 6.157. We generate 1.5M $W^{\pm}$ + jets events with $\int \mathcal{L}\ dt = 273.7\ \text{pb}^{-1}$ in which we force the $W^{\pm}$ to decay leptonically to either an e, μ, or τ.

3.2.4 Drell-Yan γ^*/Z^0

Drell-Yan γ^*/Z^0 produces a pair of OS charged leptons in the $p\bar{p}$ collider environment via the color neutral process $q\bar{q} \rightarrow \gamma^*/Z^0 \rightarrow \ell^{\pm}\ell^{\mp}$. The Drell-Yan γ^*/Z^0 production cross sections at $\sqrt{s} = 1.8$ TeV have been well-measured in the e and μ channels: $\sigma \cdot \text{BR}(Z \rightarrow ee) = 224 \pm 17$ pb and $\sigma \cdot \text{BR}(Z \rightarrow \mu\mu) = 228 \pm 18$ pb [73]. As in $W^{\pm}$ events, hadronic jets are also produced in these events. If one such jet is misidentified as a lepton, it can be selected with one of the OS dilepton pair as an LSD candidate event.

We model this background using ISAJET version 7.20 with the CTEQ3L and GRV94LO parton distribution functions. We generate 350k events of Drell-Yan γ^* with $\int \mathcal{L}\ dt = 1{,}658.5\ \text{pb}^{-1}$, with γ^* mass between 5–500 GeV/c^2. We generate 400k events of Drell-Yan Z^0 with $\int \mathcal{L}\ dt = 1{,}668.1\ \text{pb}^{-1}$, with Z^0 mass between 5–500 GeV/c^2. In the decay products we require either at least one lepton (e, μ, or τ) with $p_T > 9.0$ GeV/c in $|\eta| < 1.5$ region of the detector or two leptons with $p_T > 2.8$ GeV/c in the $|\eta| < 3.0$ region.

3.2.5 $W^{\pm}W^{\mp}$

Diboson $W^{\pm}W^{\mp}$ production can yield up to two real leptons, depending on the manner of the $W^{\pm}$ decay. Similarly to Drell-Yan γ^*/Z^0 and $W^{\pm}$ production, any real leptons produced in the $W^{\pm}$ decay can be selected with a jet misidentified as a lepton as an LSD candidate event. However, this background is small due to the small production cross section at $\sqrt{s} = 1.8$ TeV reported by CDF in 1997, $\sigma(WW \rightarrow \text{leptons}) = 10.2^{+6.3}_{-5.1}(\text{stat}) \pm 1.6(\text{syst})$ pb [74]. We model this background using ISAJET version 7.20 with the CTEQ3L and GRV94LO parton distribution functions. We generate 30k events of $W^{\pm}W^{\mp}$ with $\int \mathcal{L}\, dt = 4{,}527$ pb^{-1}.

3.2.6 QCD Dijet

Events with ≥ 2 jets but no real leptons have a small probability of being selected as an LSD candidate event with two jets misidentified as a LS dilepton pair. Diffractive QCD dijet events, which have a large production cross section at $\sqrt{s} = 1.8$ TeV [75], contain two jets produced colinearly with a rapidly falling jet p_T spectrum [76] along with any jets from an underlying event or higher order processes. Any two of the jets in these multijet events may be misidentified as LS leptons. None of the Monte Carlo programs successfully model pure QCD jet production. Therefore, we use data sidebands adjacent to the LSD signal region to estimate the QCD dijet contribution to the signal region.

3.3 LSD Background Removal

These backgrounds to the LSD signature must be removed from the remaining 21,743 LSD candidate events in the dilepton dataset by further LSD analysis cuts. After the cuts have been applied, we estimate the contribution from each

background to the signal region with the Monte Carlo events. In the case of QCD dijet background, we use data from control regions adjacent to the signal region to estimate the contribution to the signal region.

3.3.1 Z^0 Resonance

The Z^0 boson decays to an OS dilepton pair $Z^0 \rightarrow \ell^+\ell^-$ with BR = 6.7% for $\ell = e$ or μ. The Z^0 mass resonance peaks at 91.2 GeV/c^2 [4]. Events with a Z^0 which decays leptonically and a fake lepton from an underlying event may be selected as an LSD candidate event. We remove events with either of the LSD lepton candidates associated with a known resonance. By reconstructing the invariant dilepton mass of any OS dilepton pairs in an event, we can identify any events which contain a $Z^0 \rightarrow \ell^+\ell^-$ decay. The invariant dilepton mass is defined:

$$m_{\ell\ell} \equiv \sqrt{(E^{\ell 1} + E^{\ell 2})^2 - (p_x^{\ell 1} + p_x^{\ell 2})^2 - (p_y^{\ell 1} + p_y^{\ell 2})^2 - (p_z^{\ell 1} + p_z^{\ell 2})^2} \,, \qquad (3.4)$$

where $E^{\ell i}$ is the energy of each lepton in the OS pair as measured in the calorimeter and $p^{\ell i}$ is the momentum of each lepton as measured by the CTC. The LSD analysis selects the two highest-p_T LS leptons in the event. To identify a Z^0, we therefore search each LSD event for a third, opposite-sign lepton in addition to the LS pair and reconstruct its $m_{\ell\ell}$ with both the first ($m_{\ell 1 \ell 3}$) and second ($m_{\ell 2 \ell 3}$) LS leptons in the event.

The reconstructed Z^0 mass is a finite-width distribution around the central Z^0 resonance because of known uncertainties in measuring the lepton energy and momentum and because the leptons from the Z^0 decay may be produced off-shell with an invariant mass not exactly equal to the central value of the Z^0 resonance peak. Therefore, we remove events with a range of $m_{\ell\ell}$ values around the central Z^0 mass: 81 GeV/c^2 $< \; m_{\ell\ell} \; <$ 101 GeV/c^2. Figures 3.2 and 3.3 show the

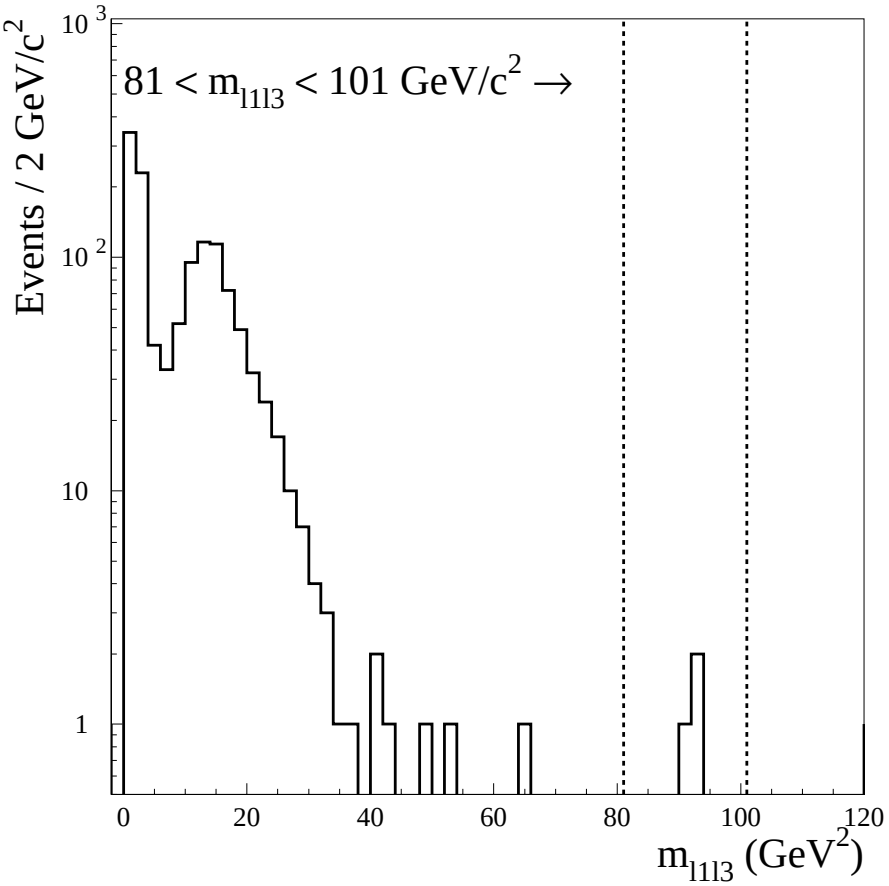

Figure 3.2: Distribution of $m_{\ell 1 \ell 3}$. The range 81 GeV/c^2 < $m_{\ell 1 \ell 3}$ < 101 GeV/c^2 is marked by the dashed lines.

invariant mass distributions and cuts for $m_{\ell 1 \ell 3}$ and $m_{\ell 2 \ell 3}$, respectively, in the LSD dataset. Events where no third OS lepton was found have been suppressed from the plot. The higher masses in general in the $m_{\ell 1 \ell 3}$ distribution are due to the LS pair being selected in order of highest and second-highest p_T LS leptons in the event.

In addition to single Drell-Yan γ^*/Z^0 production, diboson $W^{\pm}Z^0$ and Z^0Z^0 background to the LSD signal will contain at least one leptonic Z^0 decay. The

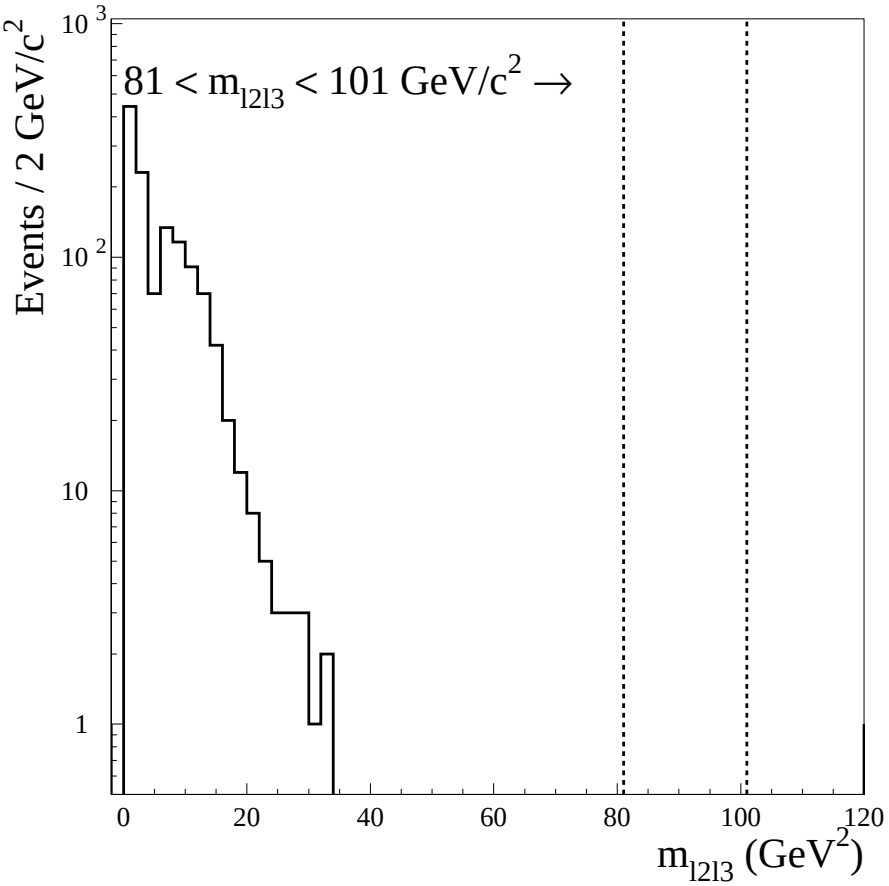

Figure 3.3: Distribution of $m_{\ell 2 \ell 3}$. The range 81 GeV/c^2 < $m_{\ell 2 \ell 3}$ < 101 GeV/c^2 is marked by the dashed lines.

LSD analysis will select one lepton from the $W^{\pm}$ and one from the Z^0 in the case of $W^{\pm}Z^0$ and one lepton from each of the Z^0 in the case of Z^0Z^0. To identify one of the Z^0, we require a third, opposite-sign lepton in addition to the LS pair. Therefore, the same cut which rejects Drell-Yan γ^*/Z^0 production around the Z^0 resonance is also effective in removing the small SM diboson $W^{\pm}Z^0$ and Z^0Z^0 contribution to the LSD signal region.

3.3.2 J/ψ and Υ Resonance

The J/ψ meson ($c\bar{c}$) decays to an OS dilepton pair $J/\psi \to \ell^+\ell^-$ with BR = 11.8% for $\ell = e$ or μ. The J/ψ mass resonance peaks at 3.097 GeV/c^2. The Υ meson ($b\bar{b}$) decays to an OS dilepton pair with a branching fraction of 4.9% for $\ell = e$ or μ. The $\Upsilon(1S)$ mass resonance peaks at 9.46030 ± 0.00026 GeV/c^2 [4]. Events with a J/ψ or $\Upsilon(1S)$ which decays leptonically and a fake lepton from an underlying event may be selected as an LSD candidate event. We remove events with either of the LSD lepton candidates associated with a known resonance. We remove these events identically to removing events with a $Z^0 \to \ell^+\ell^-$ on the Z^0 resonance peak by rejecting events with a low-mass OS dilepton pair in the event with $m_{\ell 1 \ell 3} > 10$ GeV/c^2 and $m_{\ell 2 \ell 3} > 10$ GeV/c^2. Figures 3.4 and 3.5 show the invariant mass distributions and cuts for $m_{\ell 1 \ell 3}$ and $m_{\ell 2 \ell 3}$, respectively, near the J/ψ and $\Upsilon(1S)$ resonances in the LSD dataset. Events where no third OS lepton was found have been suppressed from the plots.

This cut is also effective in removing low mass OS dilepton pairs from Drell-Yan γ^*/Z^0 production, which can contribute to the LSD signal when selected along with a fake lepton from an underlying event. After removing LSD candidates containing OS dilepton pairs with reconstructed invariant mass within the Z^0, J/ψ, and $\Upsilon(1S)$ resonance peaks, we are left with 20,575 LSD candidate events.

3.3.3 Minimum p_T

Once we have removed backgrounds from particle resonances, we require several kinematic cuts on event properties to further remove LSD backgrounds. We expect several important backgrounds to result in one or both of the LS leptons to have low p_T, including real leptons from $b\bar{b}$ and Drell-Yan γ^*/Z^0 production

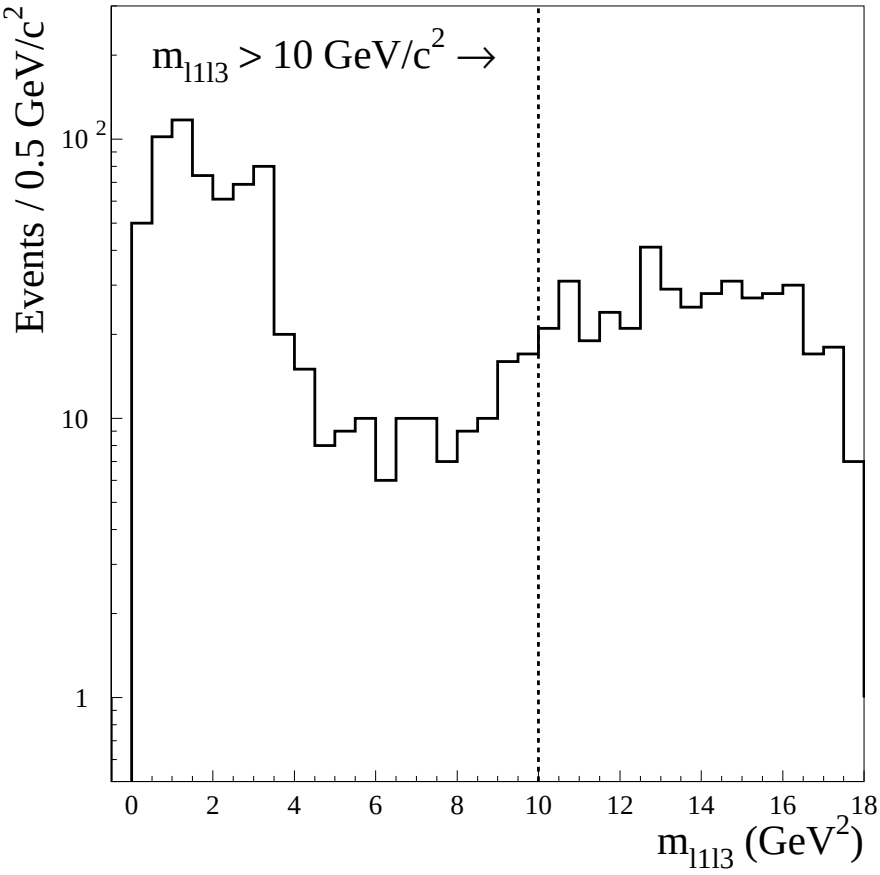

Figure 3.4: Low mass distribution of $m_{\ell 1 \ell 3}$. The $m_{\ell 1 \ell 3} > 10$ GeV/c^2 cut is marked by the dashed line.

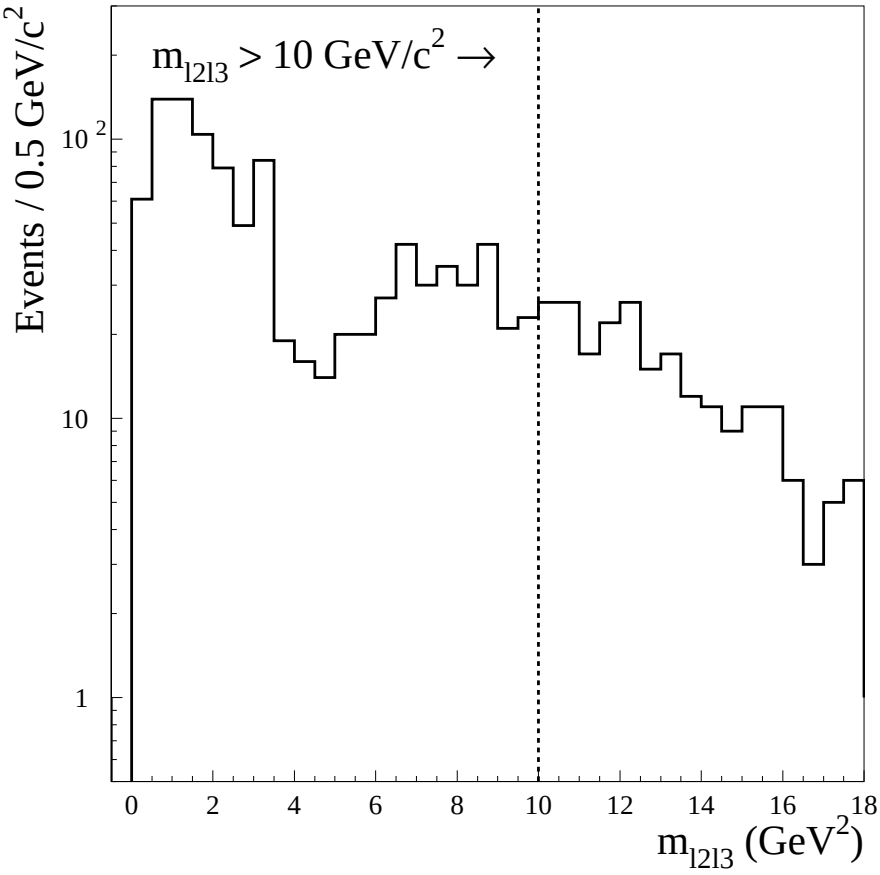

Figure 3.5: Low mass distribution of $m_{\ell 2 \ell 3}$. The $m_{\ell 2 \ell 3} > 10$ GeV/c^2 cut is marked by the dashed line.

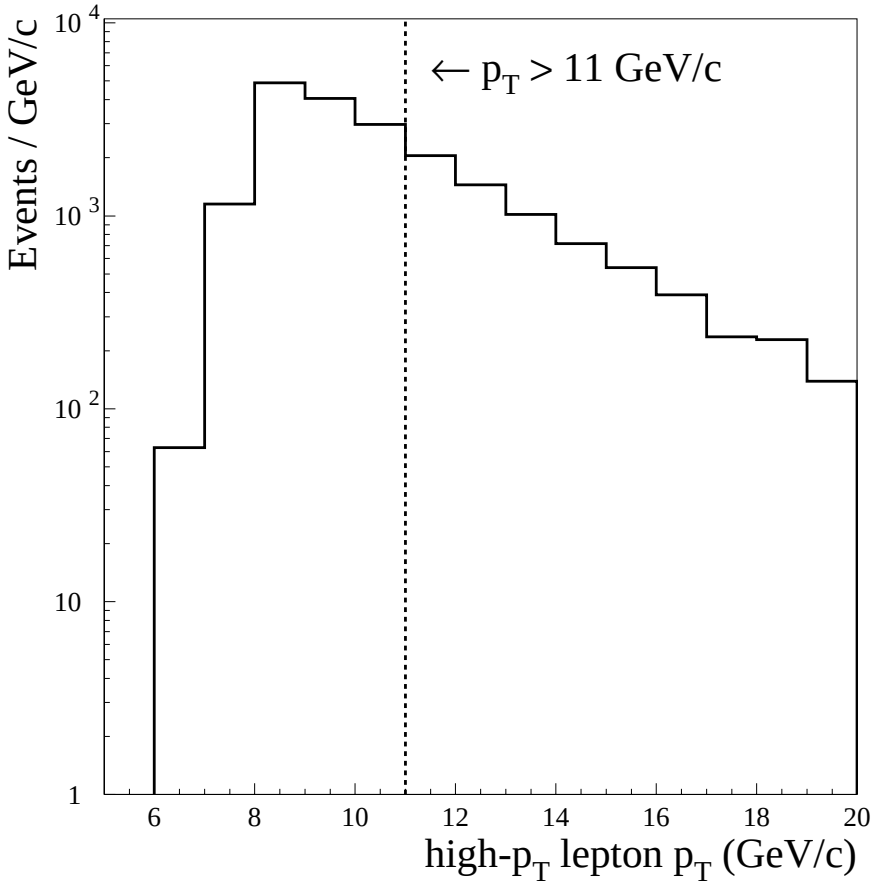

Figure 3.6: p_T distribution of the high-p_T LS lepton. The $p_T > 11$ GeV/c cut is marked by the dashed line.

and fake leptons produced in jets, which are important in $W^{\pm}W^{\mp}$, $W^{\pm}$ + jets, and QCD dijet backgrounds. Against these backgrounds, we increase the minimum p_T cut on both leptons in the LSD pair from the 6.0 and 7.5 GeV/c values used for identification of electrons and muons, respectively, to $p_T > 11$ GeV/c for both e and μ. Figures 3.6 and 3.7 show the p_T distributions of the LS leptons in the remaining LSD candidate events prior to increasing the minimum p_T cut. The $p_T > 11$ GeV/c cuts are shown as dashed lines.

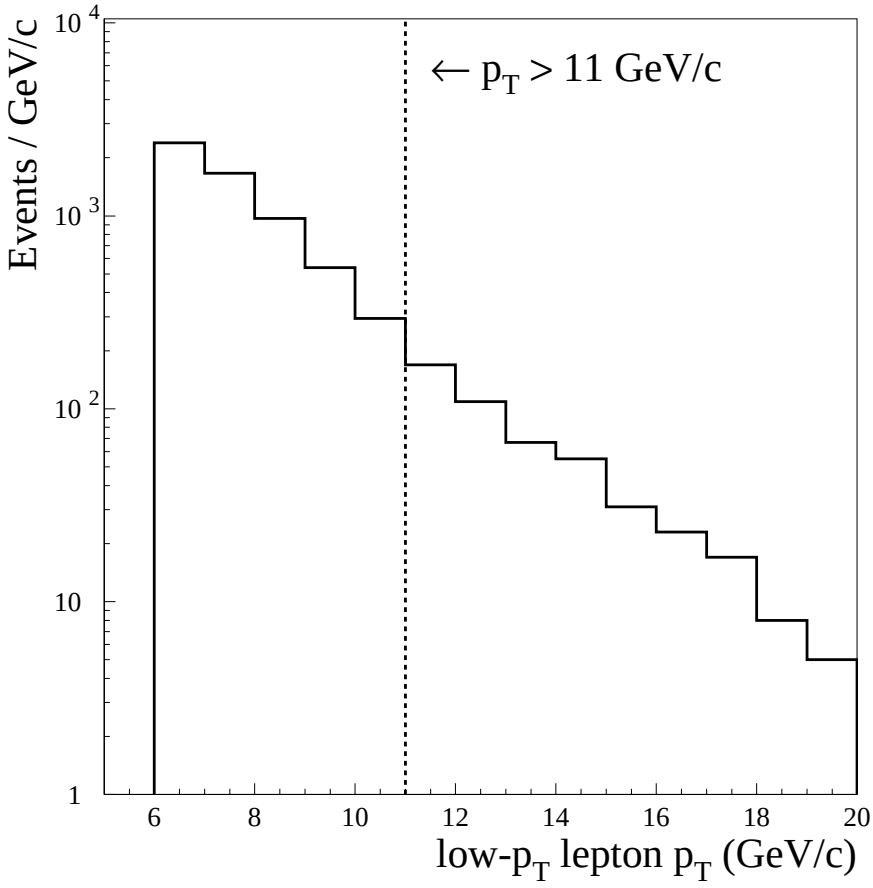

Figure 3.7: p_T distribution of the low-p_T LS lepton. The $p_T > 11$ GeV/c cut is marked by the dashed line.

Increasing the minimum p_T cut does not affect diboson $W^{\pm}W^{\mp}$, $W^{\pm}Z^0$, and Z^0Z^0 production or $t\bar{t}$ production, which yield leptonic decays to high-p_T leptons due to the large masses of the t quark and gauge bosons relative to the leptons.

3.3.4 Isolation

As discussed in Section 3.2.2, the Tevatron produces a large number of b events, making $b\bar{b}$ a substantial background. However, the b quark is light compared to

the Tevatron $\sqrt{s} = 1.8$ TeV, so that the b and $\bar{b}$ quarks will in general be produced with large momentum. This boost causes the final state leptons to be produced in the same direction as the rest of the b decay products, including the jets. A jet will usually deposit its energy across a wide area of the detector [64]. Thus, an effective method of removing events containing leptons that originate from b decays is to require little energy in the detector surrounding the lepton candidate.

This requirement, called isolation (ISO), has been improved from previous CDF searches [31, 77], due to its vital contribution to the LSD analysis by effectively cutting against $b\bar{b}$ and fake lepton backgrounds. In this analysis, ISO is defined as the scalar sum of the E_T measured in each calorimeter cell, $\sum E_T$, added in quadrature to the scalar sum of the p_T measured in the CTC, $\sum p_T$, within a cone $\Delta R \equiv \sqrt{(\Delta\phi)^2 + (\Delta\eta)^2}$ of each lepton candidate. The energy of the lepton candidate is removed from the ISO sum by subtracting the p_T of the lepton candidate track, p_T^{cand}, and the calorimeter E_T of the lepton candidate, E_T^{cand}, from $\sum p_T$ and $\sum E_T$, respectively,

$$ISO = \sqrt{((\sum E_T) - E_T^{cand})^2 + ((\sum p_T) - p_T^{cand})^2} \ , \tag{3.5}$$

where E_T^{cand} is the scalar sum of the E_T in the calorimeter tower to which we extrapolate the lepton candidate track (the "seed" tower) and the adjacent towers into which we expect the energy from the lepton candidate to spread. This effect is called leakage:

$$E_T^{cand} = E_T^{seed} + E_T^{leakage} \ . \tag{3.6}$$

We have changed $E_T^{leakage}$ so that the lepton is excised from $\sum E_T$ more effectively by modeling the energy leakage between towers in greater detail [78]. The details of leakage modeling and the improvement of the ISO cut is discussed in Appendix D.

To remove lepton candidates which are associated with jets, we require both a loose ISO cut on a cone of $\Delta R = 0.7$ in $\eta - \phi$ space, $ISO_{\Delta R=0.7} < 7$ GeV, and a tighter cut on a cone of $\Delta R = 0.4$, $ISO_{\Delta R=0.4} < 2$ GeV. In general the looser cut removes events with a large amount of energy in the event underlying the lepton production. Figure 3.8 shows the $ISO_{\Delta R=0.7}$ distributions for the high and low-p_T leptons in the LS dilepton pair and the $ISO_{\Delta R=0.7} < 7$ GeV cut applied to each lepton. The tighter cut then removes events with individual lepton candidates which are associated with jet production. Figure 3.9 shows the $ISO_{\Delta R=0.4}$ distributions for the high and low-p_T leptons in the LS dilepton pair and the $ISO_{\Delta R=0.4} < 4$ GeV cut applied to each lepton after the $ISO_{\Delta R=0.7} < 7$ GeV cut has been applied to both leptons.

Isolation does not affect diboson $W^{\pm}Z^0$ and Z^0Z^0 background, as the leptons produced in the decays of the gauge bosons are not associated with jets and therefore well isolated. Real leptons produced in the $W^{\pm}$ + jets, diboson $W^{\pm}W^{\mp}$, and Drell-Yan γ^*/Z^0 processes are also well isolated. However, as we expect an LSD candidate event to be selected from these backgrounds with one lepton from a jet misidentified as a lepton the isolation cut is effective against these backgrounds as well. Isolation cuts most effectively against $b\bar{b}$ and QCD dijet backgrounds.

3.3.5 Dilepton Pair p_T

Diffractive QCD dijet events in the LSD dataset can be well-identified by the angle between the two colinear jets produced in the detector ($\Delta\phi$), which should approach 180°. As we generally expect each lepton in the LS pair to come from one of these jets, we can remove difake events with a cut away from 180° between the LS lepton pair. A complementary cut to a $\Delta\phi$ cut is dilepton pair

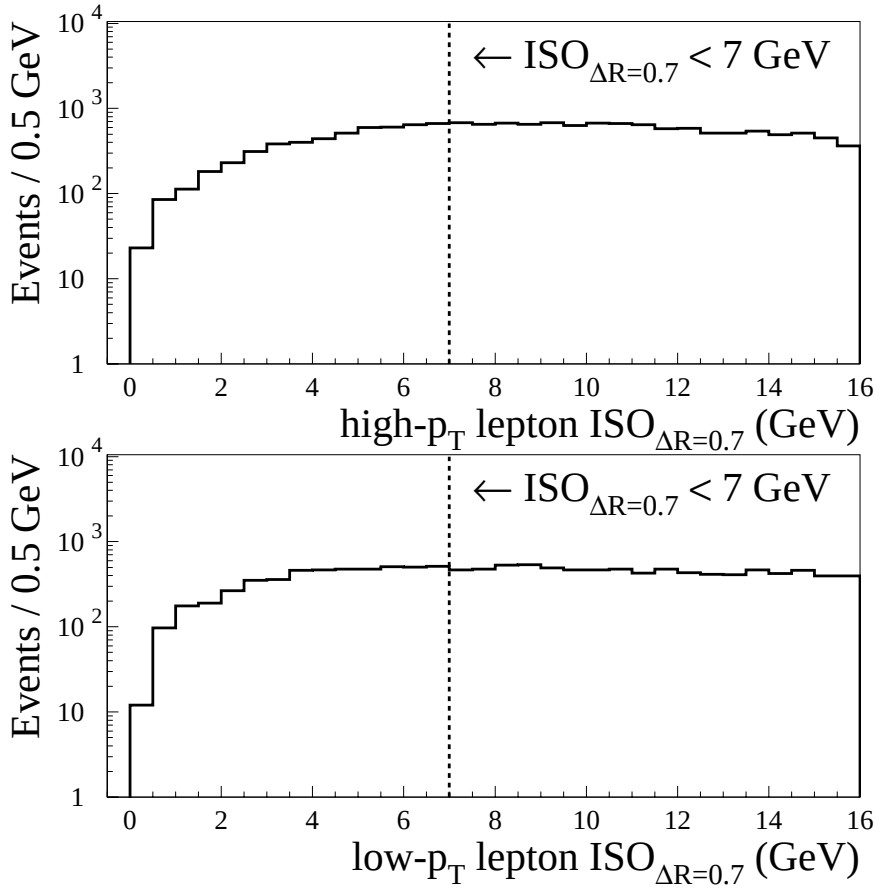

Figure 3.8: Distribution of $ISO_{\Delta R=0.7}$ for the high-p_T lepton (top) and low-p_T lepton (bottom) in the LS dilepton pair. The $ISO_{\Delta R=0.7} < 7$ GeV requirement is marked by the dashed lines.

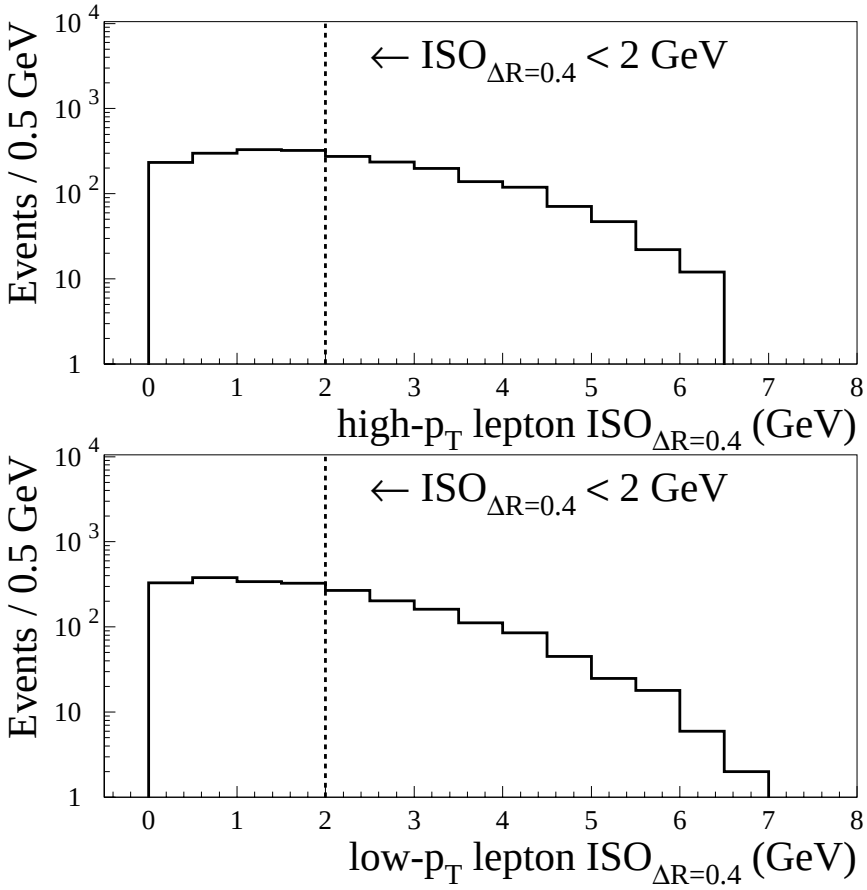

Figure 3.9: Distribution of $ISO_{\Delta R=0.4}$ for the high-p_T lepton (top) and low-p_T lepton (bottom) in the LS dilepton pair. The $ISO_{\Delta R=0.4} < 2$ GeV requirement is marked by the dashed lines. The $ISO_{\Delta R=0.7} < 7$ GeV has already been applied to these distributions.

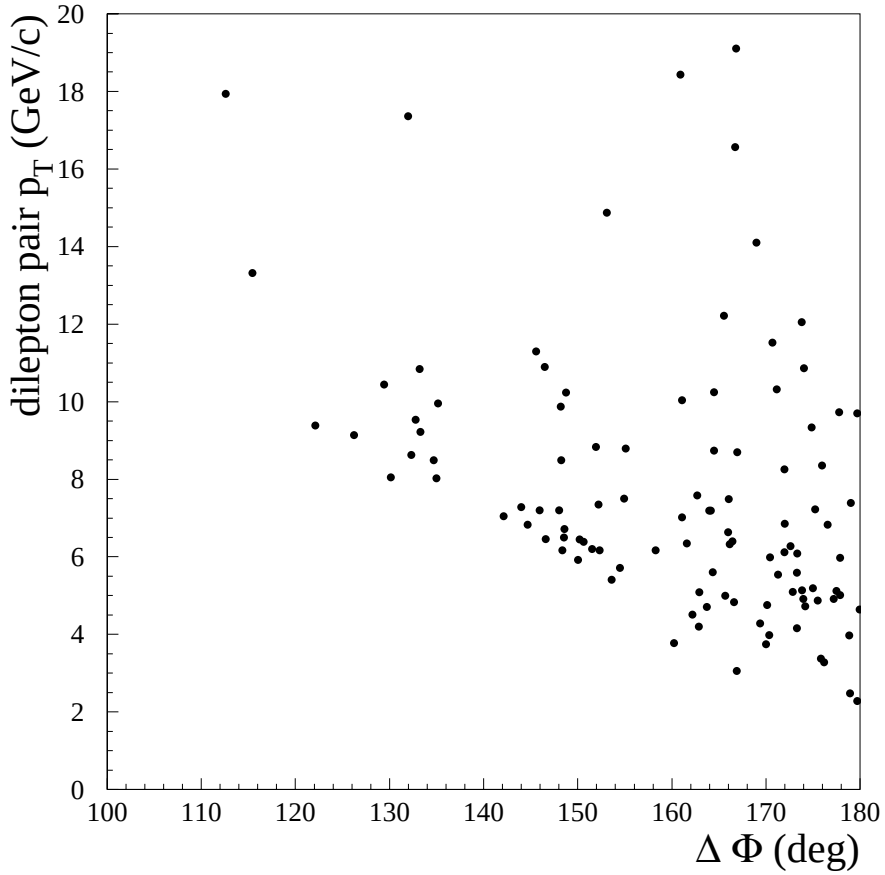

Figure 3.10: Distribution of $p_T^{\ell\ell}$ as a function of $\Delta\phi$ in events passing all other LSD analysis cuts.

p_T. Dilepton pair p_T is the vector sum transverse momentum of the LS lepton pair:

$$p_T^{\ell\ell} \equiv \sqrt{(p_x^{\ell 1} + p_x^{\ell 2})^2 + (p_y^{\ell 1} + p_y^{\ell 2})^2} \ , \tag{3.7}$$

where $p^{\ell i}$ is the momentum of each lepton as measured by the CTC. Figure 3.10 shows $p_T^{\ell\ell}$ as a function of $\Delta\phi$ for events passing all the other LSD analysis cuts. Events with low $p_T^{\ell\ell}$ (< 6 GeV/c) always have $\Delta\phi$ approaching 180°, demonstrating the ability of $p_T^{\ell\ell}$ to select QCD dijet events. However, as $p_T^{\ell\ell}$ increases there

is an increasing spread in $\Delta\phi$, probably due to events selected with a more complicated jet topology. Thus, while a strict $\Delta\phi$ cut removes only events with both LS leptons selected from misidentified jets from the QCD dijet pair, a $p_T^{\ell\ell}$ cut removes both these events and events selected from one jet from the QCD dijet pair and one jet from other jet production.

To remove QCD dijet plus additional jet background, we require $p_T^{\ell\ell} > 20$ GeV/c. Figure 3.11 shows the $p_T^{\ell\ell}$ distribution in the LSD candidate events after removing the Z^0, J/ψ, and $\Upsilon(1S)$ resonances but before applying the remaining LSD analysis kinematic cuts: minimum p_T and ISO.

QCD dijet events also tend to have low invariant mass of the LS dilepton pair because of the colinearity of the leptons. We calculate the invariant mass of the LS dilepton pair, $m_{\ell\ell}$, identically to the OS dilepton invariant mass defined in Section 3.3.1. We require $m_{\ell\ell} > 10$ GeV/c^2 as an extra cut against QCD dijet background. This cut is also effective against Drell-Yan γ^*/Z^0 production where one of the OS Drell-Yan γ^*/Z^0 pair is not detected (causing the OS dilepton mass cuts $m_{\ell 1\ell 3} > 10$ GeV/c^2 and $m_{\ell 2\ell 3} > 10$ GeV/c^2 to be ineffective) and the remaining lepton along with a misidentified jet fakes the LSD signal. Table 3.5 summarizes the important LSD analysis cuts, including the same-sign $Q_1 \times Q_2 = 1$ requirement.

3.4 LSD Background Estimation

The LSD signature backgrounds are divided into three types defined in Section 3.2: real dilepton, lepton + fake, and difake. We use different techniques to estimate the contribution to the LSD signal region from each type of background.

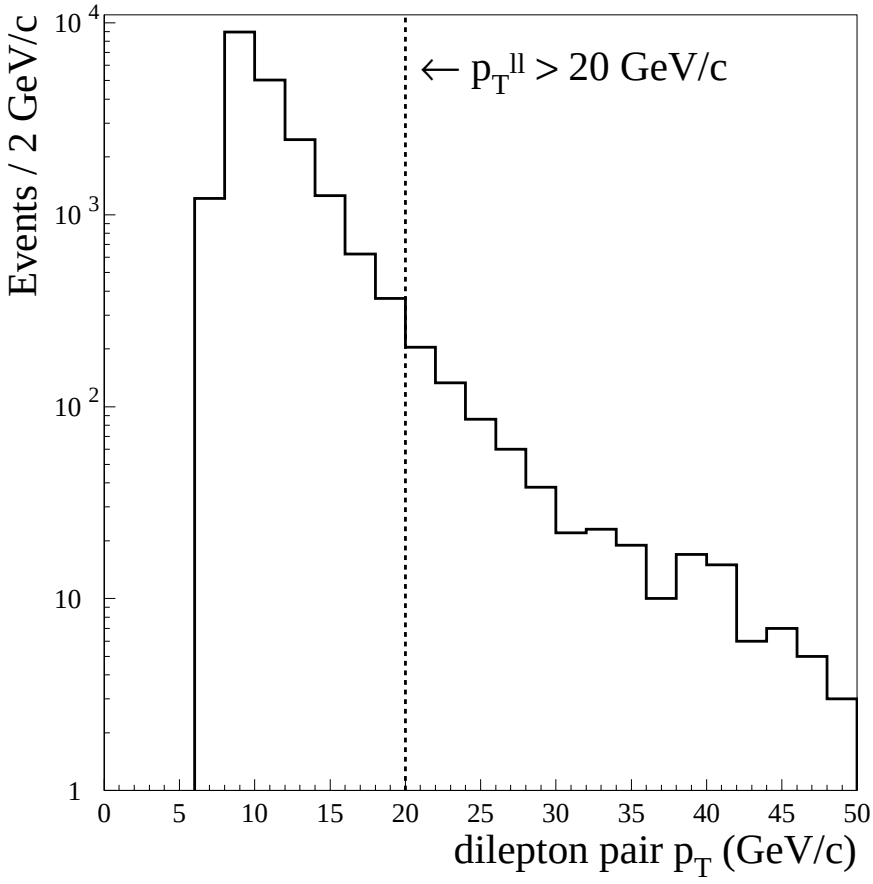

Figure 3.11: Distribution of $p_T^{\ell\ell}$ prior to applying any kinematic cuts. The $p_T^{\ell\ell} > 20$ GeV/c cut is marked by the dashed line.

3.4.1 Real Dilepton

Real dilepton backgrounds are selected from diboson $W^{\pm}Z^0$ and Z^0Z^0 and heavy flavor $t\bar{t}$ and $b\bar{b}$ production. We select LSD events with two reconstructed leptons from the Monte Carlo generated for these backgrounds identically to selecting LSD candidate events in the data. We then apply the event quality and LSD background removal cuts, weight the remaining events with the QFL lepton efficiency correction factor, C_{QFL}, defined in Section 2.2.7 and the Monte Carlo

Background	Same-sign	Isolation	minimum p_T	$p_T^{\ell\ell}$ and $m_{\ell\ell}$
$W^{\pm}W^{\mp}$	$\surd$	$\surd$	$\surd$	
$t\bar{t}$	$\surd$	$\surd$		
Drell-Yan γ^*/Z^0	$\surd$	$\surd$	$\surd$	$\surd$
$W^{\pm}Z^0$, Z^0Z^0	$\surd$			
$b\bar{b}$	$\surd$	$\surd$	$\surd$	
$W^{\pm}$ + jets	$\surd$	$\surd$	$\surd$	
QCD dijet		$\surd$	$\surd$	$\surd$

Table 3.5: Summary of the LSD analysis cuts. A $\surd$ indicates that a given cut is effective in removing the listed background.

trigger weight,W_{trig}, defined in Section 2.2.9, and scale the number of selected events to the CDF Run I dataset $\int \mathcal{L}\, dt = 107$ pb^{-1}.

Figures 3.12 and 3.13 show distributions of p_T for both high and low-p_T leptons and $m_{\ell 1 \ell 3}$ and $m_{\ell 2 \ell 3}$ in $W^{\pm}Z^0$ and Z^0Z^0 Monte Carlo events, respectively, with event quality cuts but no LSD analysis cuts applied. Events with no third OS lepton identified in the event have been suppressed from the invariant mass plots. The 81 GeV/c^2 $< m_{\ell\ell} <$ 101 GeV/c^2 resonance window and $p_T > 11$ GeV/c cuts are marked by dashed lines on the appropriate plots. The p_T cut is largely ineffective against these backgrounds, while the $m_{\ell 1 \ell 3}$ and $m_{\ell 2 \ell 3}$ cuts remove 78% of $W^{\pm}Z^0$ and 67% of Z^0Z^0 events with an identified third lepton. The Z^0 resonance cut removes a smaller fraction of Z^0Z^0 events with a third lepton than $W^{\pm}Z^0$ events due to a larger contamination from low p_T leptons in the Z^0Z^0 sample, seen in Figure 3.13 in the low-p_T lepton p_T and $m_{\ell 2 \ell 3}$ distributions. This contamination is likely from fake leptons from jets. However, most events escaping the invariant mass cuts are primarily those in which no third lepton is

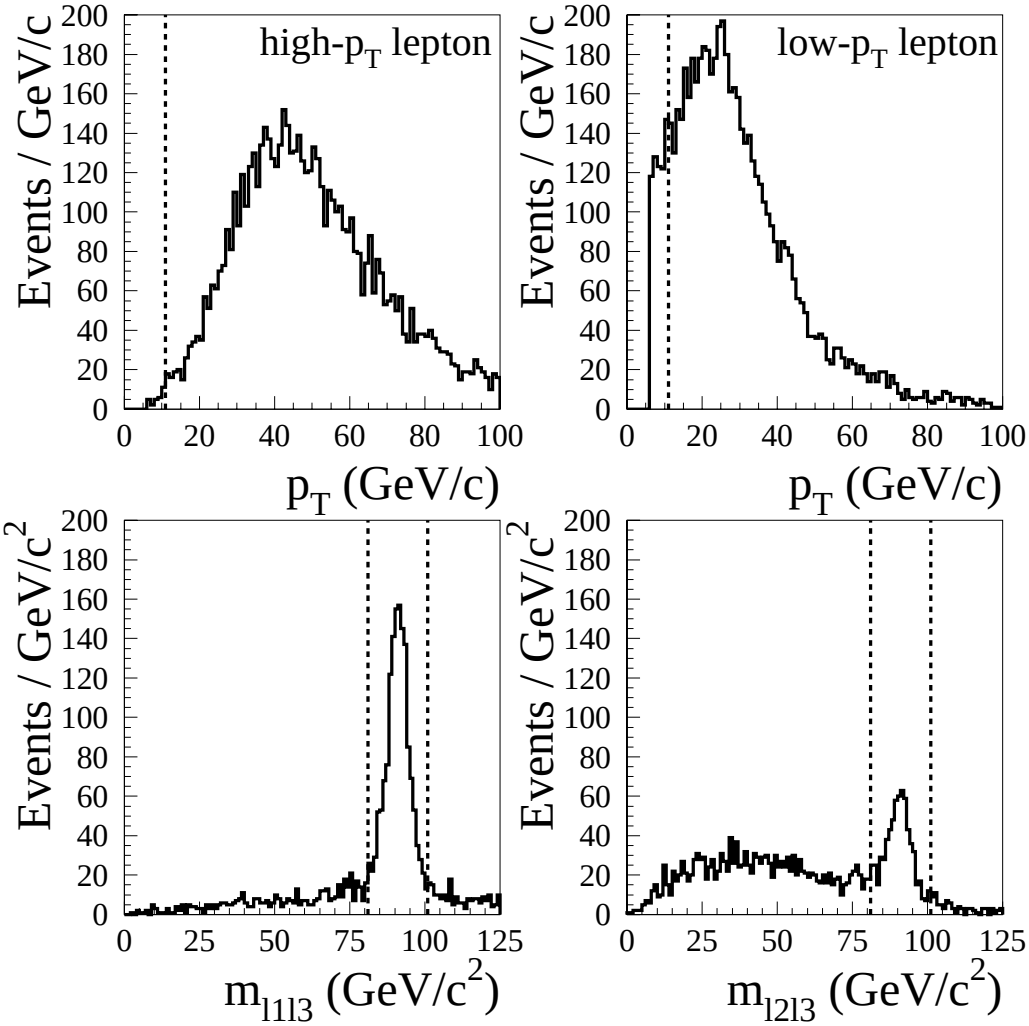

Figure 3.12: Distributions of p_T for both high and low-p_T leptons and $m_{\ell 1 \ell 3}$ and $m_{\ell 2 \ell 3}$ in $W^{\pm}Z^0$ Monte Carlo events prior to applying any LSD analysis cuts. The $p_T > 11$ GeV/c cut for each lepton and 81 GeV/c^2 $< m_{\ell\ell} <$ 101 GeV/c^2 resonance window are marked by dashed lines.

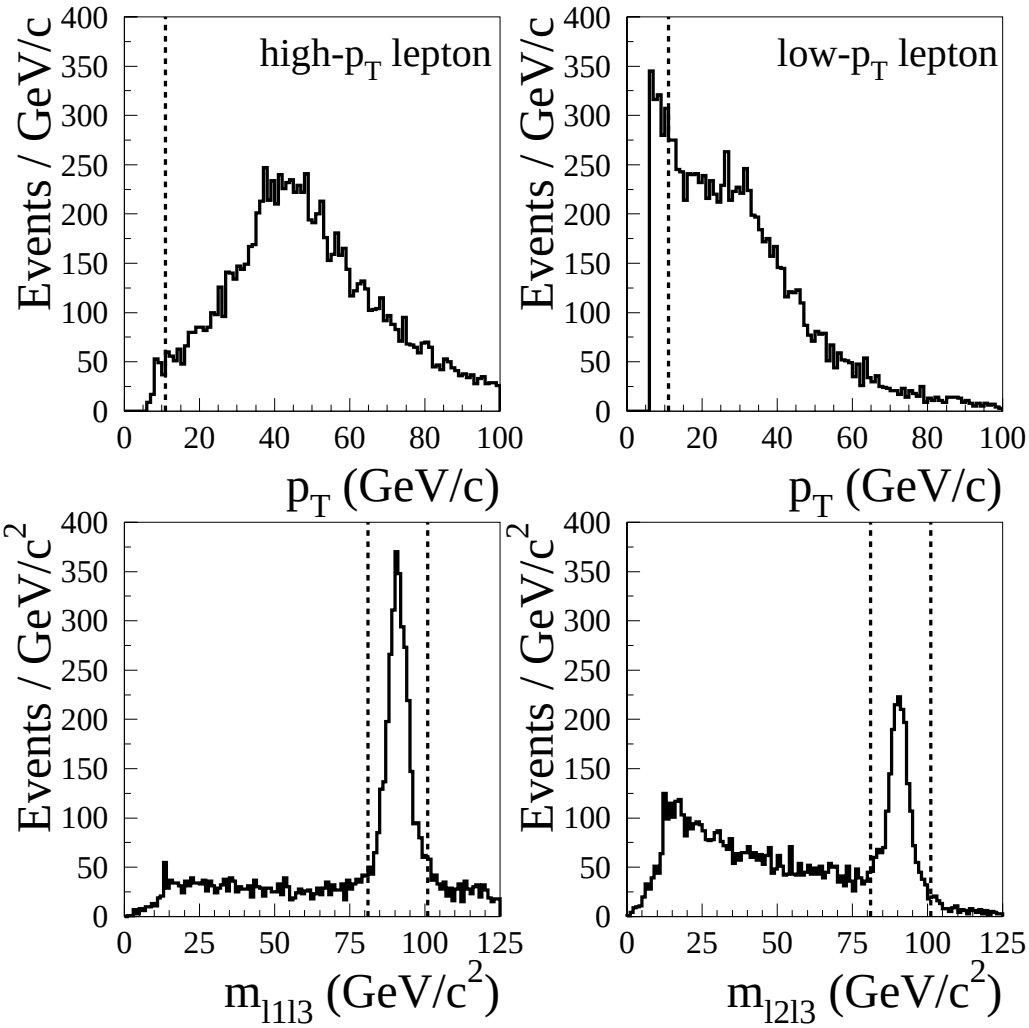

Figure 3.13: Distributions of p_T for both high and low-p_T leptons and $m_{\ell 1 \ell 3}$ and $m_{\ell 2 \ell 3}$ in $Z^0 Z^0$ Monte Carlo events prior to applying any LSD analysis cuts. The $p_T > 11$ GeV/c cut for each lepton and 81 GeV/c^2 $< m_{\ell\ell} <$ 101 GeV/c^2 resonance window are marked by dashed lines.

found due to the low ($\sim 40\%$) efficiency to identify three leptons in the CDF detector. After applying the LSD analysis cuts and scaling the Monte Carlo events to match the data luminosity we estimate 0.229 ± 0.004 and 0.061 ± 0.001 events in the LSD signal region from $W^{\pm}Z^0$ and Z^0Z^0, respectively.

Figure 3.14 shows distributions of p_T for both high and low-p_T leptons in $t\bar{t}$ Monte Carlo events with only event quality and resonance cuts applied. Figure 3.15 shows distributions of $ISO_{\Delta R=0.4}$ and $ISO_{\Delta R=0.7}$ for both high and low-p_T leptons in $t\bar{t}$ Monte Carlo events with the same applied cuts. The high-p_T LS leptons in this Monte Carlo sample are high-p_T, non-isolated leptons consistent with the decay of the heavy t quark to light e and μ via the semi-leptonic b decay process discussed in Section 3.2.2. The combined $ISO_{\Delta R=0.4} < 2$ GeV and $ISO_{\Delta R=0.7} < 7$ GeV cuts on the high-p_T lepton removes 52% of this sample. These cuts together with the $p_T > 11$ GeV/c cut applied to the low-p_T lepton removes a total of 80% of the $t\bar{t}$ background. After applying the LSD analysis cuts and scaling the Monte Carlo events to match the data luminosity we estimate $0.008^{+0.006}_{-0.004}$ events in the LSD signal region from $t\bar{t}$ production.

Figure 3.16 shows distributions of p_T for both high and low-p_T leptons in $b\bar{b}$ Monte Carlo events with only event quality and resonance cuts applied. Figure 3.17 shows distributions of $ISO_{\Delta R=0.4}$ and $ISO_{\Delta R=0.7}$ for both high and low-p_T leptons in $b\bar{b}$ Monte Carlo events with the same applied cuts. For brevity these plots include all $b\bar{b}$ Monte Carlo samples listed in Table 3.4. When estimating the $b\bar{b}$ background contribution to the LSD signal region, we compute the direct, initial state gluon radiation, and final state gluon radiation production mechanism estimates separately and sum them to calculate the total estimated events from $b\bar{b}$ production.

In general both LS leptons in the $b\bar{b}$ Monte Carlo samples have low p_T and

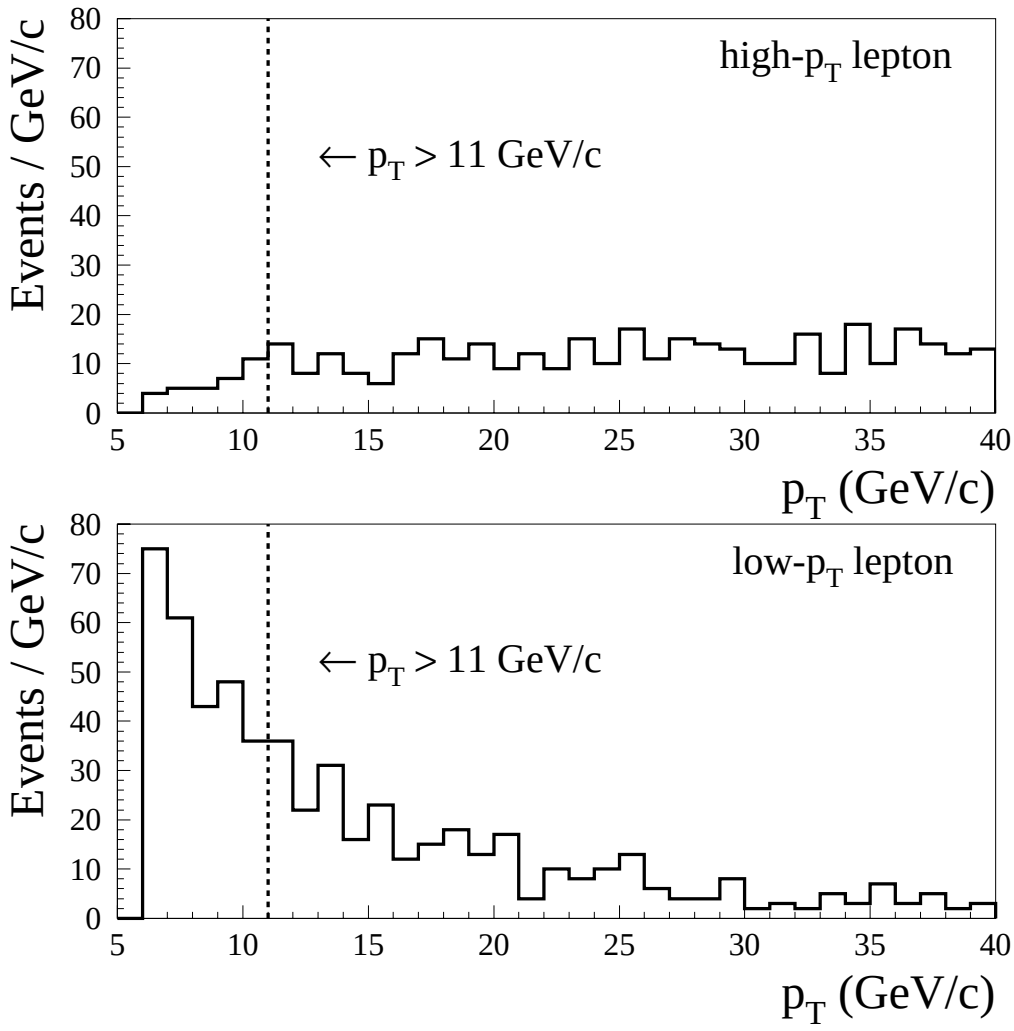

Figure 3.14: Distributions of p_T for both high and low-p_T leptons in $t\bar{t}$ Monte Carlo events after applying only the resonance windows of the LSD analysis cuts. The $p_T > 11$ GeV/c cut for each lepton is marked by dashed lines.

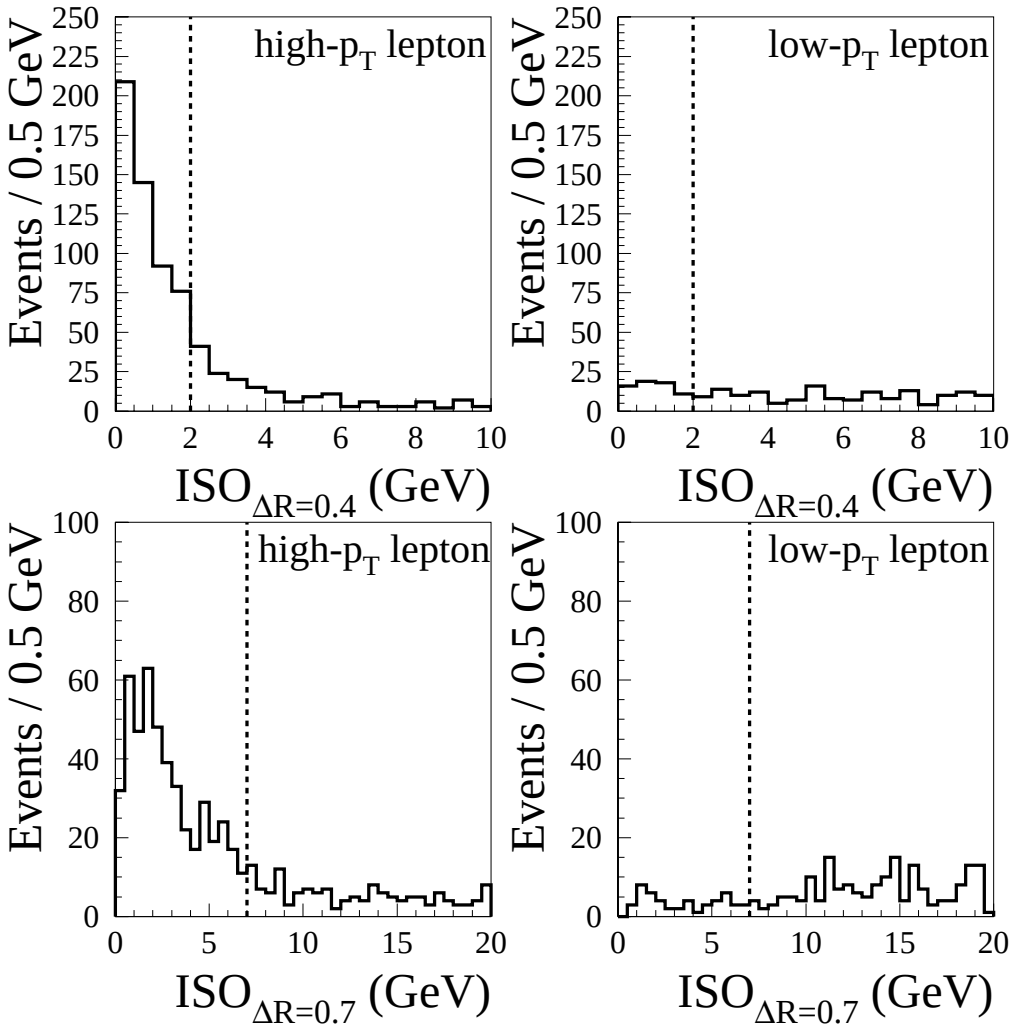

Figure 3.15: Distributions of $ISO_{\Delta R=0.4}$ and $ISO_{\Delta R=0.7}$ for both high and low-p_T leptons in $t\bar{t}$ Monte Carlo events after applying only the resonance windows of the LSD analysis cuts. The $ISO_{\Delta R=0.4} < 2$ GeV and $ISO_{\Delta R=0.7} < 7$ GeV cuts for each lepton are marked by dashed lines.

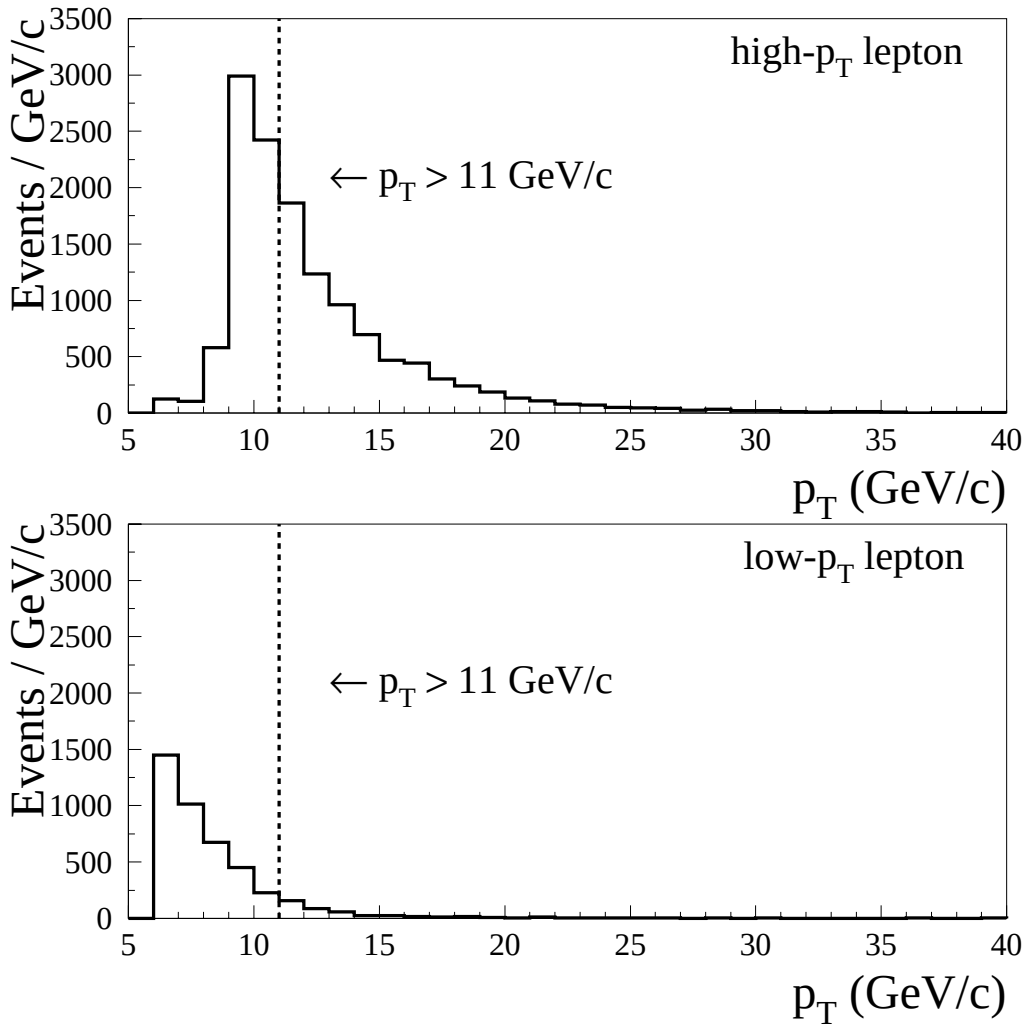

Figure 3.16: Distributions of p_T for both high and low-p_T leptons in $b\bar{b}$ Monte Carlo events after applying only the resonance windows of the LSD analysis cuts. The $p_T > 11$ GeV/c cut for each lepton is marked by dashed lines.

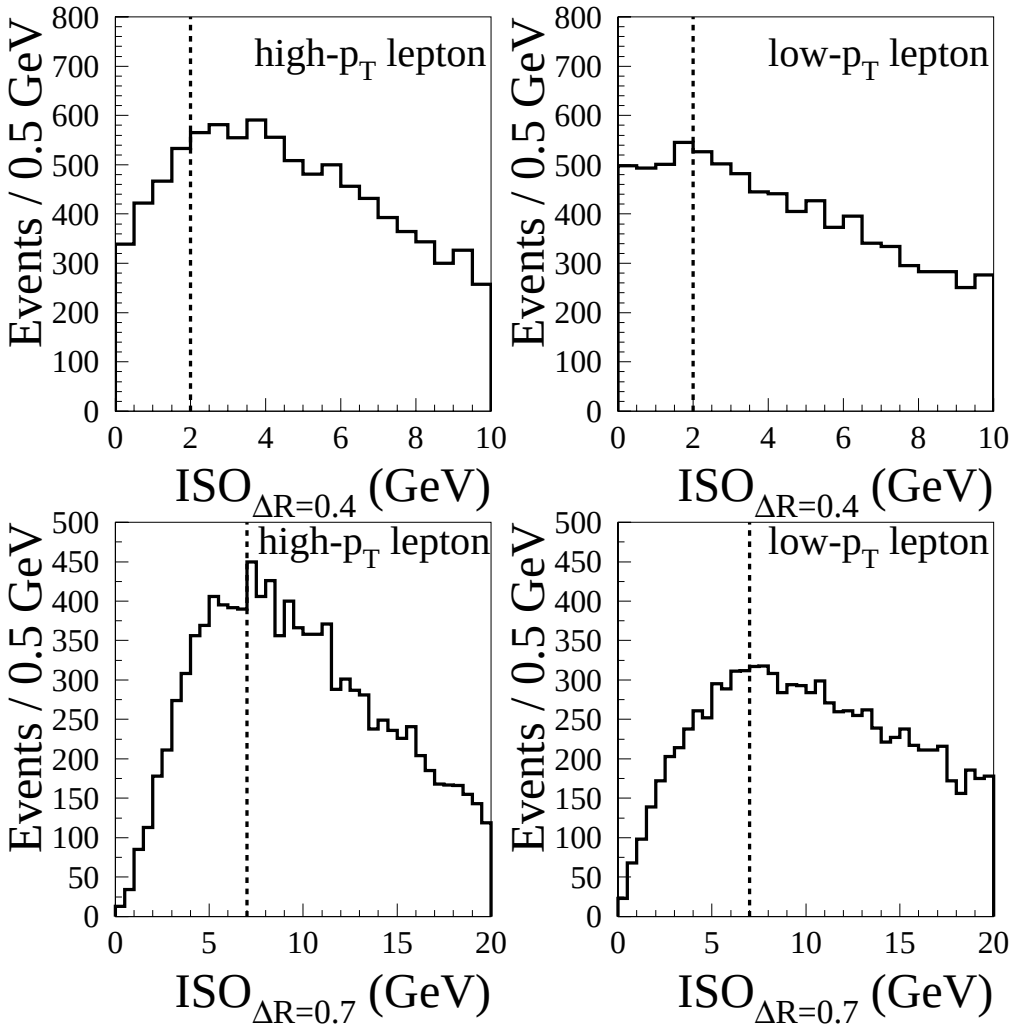

Figure 3.17: Distributions of $ISO_{\Delta R=0.4}$ and $ISO_{\Delta R=0.7}$ for both high and low-p_T leptons in $b\bar{b}$ Monte Carlo events after applying only the resonance windows of the LSD analysis cuts. The $ISO_{\Delta R=0.4} < 2$ GeV and $ISO_{\Delta R=0.7} < 7$ GeV cuts for each lepton are marked by dashed lines.

large ISO, consistent with the semi-leptonic b and $\bar{b}$ decays resulting in almost all final state leptons associated with jets as discussed in Section 3.2.2. Thus, it is unlikely that both of the LS leptons selected from a $b\bar{b}$ event will pass the ISO cuts. Applying the $ISO_{\Delta R=0.4} < 2$ GeV and $ISO_{\Delta R=0.7} < 7$ GeV cuts together with the $p_T > 11$ GeV/c cut removes 99% of this sample. After applying the LSD analysis cuts and scaling the Monte Carlo events to match the data luminosity we estimate $0.0^{+0.001}_{-0.0}$ events in the LSD signal region from $b\bar{b}$ production.

3.4.2 Lepton + Fake

Lepton + fake backgrounds are selected from diboson $W^{\pm}W^{\mp}$, Drell-Yan γ^*/Z^0, and $W^{\pm}$ + jets production. To estimate the contribution to the LSD signal region from these backgrounds, we first check that the Monte Carlo used to generate the background samples correctly models the rate of isolated tracks per event as a function of track p_T using the $Z^0 \rightarrow \ell^+\ell^-$ data samples defined in Appendices B.2.1 and B.2.2. We then use the jet data samples defined in Appendix B.2.4 to measure the "fake rate": the probability that such an isolated track passes all of the lepton ID cuts described in Section 3.1.5 and 3.1.6. Finally, we select events from the Monte Carlo with at least one lepton passing the lepton ID cuts and a like-sign, isolated track from the TRKS bank. The initial selection cuts on the track are loose: $ISO_{\Delta R=0.4} < 2$ GeV, no cut on $ISO_{\Delta R=0.7}$, and $p_T > 4$ GeV.

To these lepton + track events we apply the usual event quality and LSD background removal cuts, *except* those such as electron fiducial or muon hitmask which require information for real e or μ which does not exist in the TRKS bank. We then multiply the number of selected events by the fake rate, which accounts for the probability of the selected track in the event faking a real lepton. Finally,

we weight the fake rate scaled events with C_{QFL} and W_{trig}, and scale the number of selected events to $\int \mathcal{L}\, dt = 107$ pb^{-1}.

3.4.3 Isolated Track Rate

We compare the rate of isolated tracks per event between data and Monte Carlo as a function of p_T in $Z^0 \rightarrow \ell^+\ell^-$ events, excluding the two tracks from the legs of the Z^0. We define the p_T-dependent isolated track rate per event:

$$R_{isotrk} \equiv \frac{N_{sel}}{N_{events}} \ , \tag{3.8}$$

where N_{sel} is the number of isolated tracks selected in a given p_T bin, and N_{events} is the total number of events in the $Z^0 \rightarrow \ell^+\ell^-$ sample. We use $Z^0 \rightarrow \ell^+\ell^-$ events within the Z^0 resonance peak, 81 GeV/c^2 $< m_{\ell\ell} <$ 101 GeV/c^2, because these events have been removed from the LSD signal region by the Z^0 resonance cut. Thus, using this data to estimate the lepton + fake background in the signal region will not bias the final result. We cannot use $W^\pm \rightarrow \ell^\pm\nu$ data to compare R_{isotrk} between data and Monte Carlo without opening the LSD signal region. However, based on expectations from the SM, we assume that R_{isotrk} is the same in $W^\pm \rightarrow \ell^\pm\nu$ + jets events as it is in $Z^0 \rightarrow \ell^+\ell^-$ + jets events.

For Z^0 data we use the 1,255 high-quality $Z^0 \rightarrow e^+e^-$ events and 1,389 high-quality $Z^0 \rightarrow \mu^+\mu^-$ events selected in Appendices B.2.1 and B.2.2. These events must contain a high-p_T OS dilepton pair with dilepton invariant mass in the Z^0 resonance peak: 81 GeV/c^2 $< m_{\ell\ell} <$ 101 GeV/c^2. We require Monte Carlo $Z^0 \rightarrow \ell^+\ell^-$ samples generated with both PYTHIA and ISAJET. We use the ISAJET version 7.20 Drell-Yan γ^*/Z^0 sample presented in Section 3.2.4, which contains 350k γ^* production and 400k Z^0 production events. We generate 200k Drell-Yan Z^0 events with PYTHIA version 6.157, forcing the Z^0 to decay leptonically. We select $Z^0 \rightarrow \ell^+\ell^-$ events from these Monte Carlo samples

Cut	Value
p_T	≥ 3.0 GeV/c
d_0	≤ 0.5 cm
$ISO_{\Delta R=0.4}$	≤ 5.0 GeV

Table 3.6: Initial cuts for a low-p_T, minimally-isolated track selected from $Z^0 \rightarrow \ell^+\ell^-$ data and Monte Carlo samples.

identically to the selection made on the Z^0 dilepton data sample. We are left with 17,029 $Z^0 \rightarrow e^+e^-$ events and 22,267 $Z^0 \rightarrow \mu^+\mu^-$ events in the ISAJET sample, and 4,677 $Z^0 \rightarrow e^+e^-$ events and 6,166 $Z^0 \rightarrow \mu^+\mu^-$ events in the PYTHIA sample. Figure 3.18 shows the $m_{\ell\ell}$ distributions for the combined $Z^0 \rightarrow e^+e^-$ and $Z^0 \rightarrow \mu^+\mu^-$ data and Monte Carlo samples.

We search these events for an isolated track candidate, excluding the tracks associated with the Z^0 dilepton pair. We select the highest-p_T, loosely-isolated track in each event with the cuts given in Table 3.6. To ensure that these track candidates are not associated with a third real lepton in the event (for example, if the Z^0 event was selected from the leptonic decay of $W^{\pm}Z^0$ production), we require that the track candidate does not have an associated ELES or CMUO bank in the data stream; if the track candidate has an associated ELES or CMUO bank the events we remove the event from the data or Monte Carlo sample, making N_{events}, the R_{isotrk} denominator, negligibly smaller while removing real leptons from N_{sel}, the R_{isotrk} numerator.

We then require that each isolated track candidate has $p_T > 5$ GeV/c to be consistent with the strict lepton ID cuts for the LSD analysis. In each $Z^0 \rightarrow \ell^+\ell^-$ sample, we apply the $ISO_{\Delta R=0.4} < 2$ GeV and $ISO_{\Delta R=0.7} < 7$ GeV cuts to each track candidate in p_T bins of 1 GeV/c to determine N_{sel}, the number of isolated

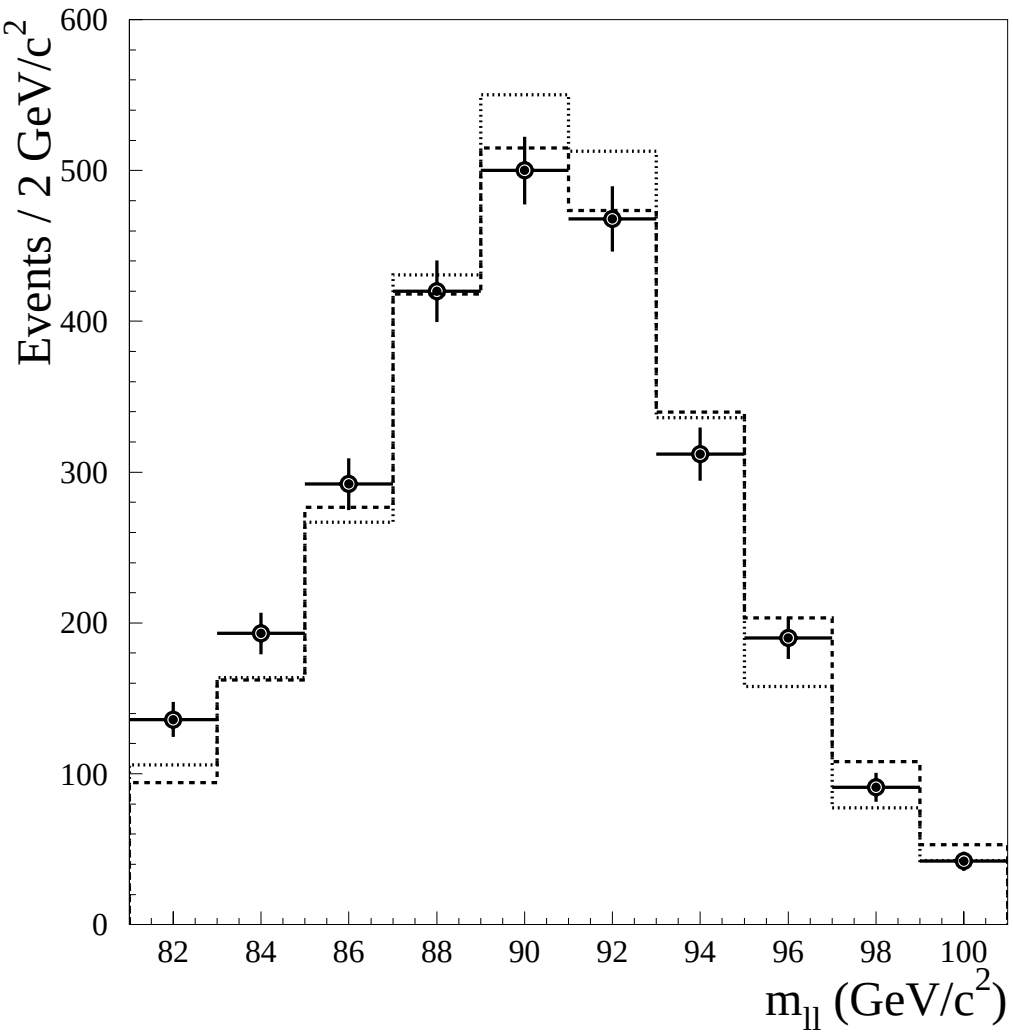

Figure 3.18: Distributions of $m_{\ell\ell}$ in the ISAJET (dashed histogram), PYTHIA (dotted histogram), and data (points) $Z^0 \rightarrow \ell^+\ell^-$ samples. The Monte Carlo histograms have been normalized to the 2,644 events in the data.

track p_T bin (GeV/c)	N_{sel}		
	data	ISAJET	PYTHIA
5-6	11	245	34
6-7	5	115	15
7-8	2	67	9
8-9	1	36	4
9-10	0	23	1
10-11	0	15	1

Table 3.7: The number of selected isolated tracks (N_{sel}) in track p_T bins of 1 GeV/c in $Z^0 \rightarrow \ell^+\ell^-$ data and ISAJET and PYTHIA Monte Carlo.

tracks as a function of track p_T. Table 3.7 lists N_{sel} for p_T bins in the range $5 < p_T < 11$ GeV/c for each sample. We divide N_{sel} by N_{events} = 2,616 events in the data sample and by N_{events} = 39,155 and 10,829 in the ISAJET and PYTHIA Monte Carlo samples, respectively, to calculate R_{isotrk} as a function of p_T. Figure 3.19 shows the R_{isotrk} distributions in the $Z^0 \rightarrow \ell^+\ell^-$ ISAJET (dashed histogram), PYTHIA (dotted histogram), and data (points) samples. As R_{isotrk} is by definition normalized to the number of events in the sample, we do not *a priori* rescale the Monte Carlo distributions to match the data.

The R_{isotrk} measurement in data is limited by low statistics, with no events found containing a $p_T > 9$ GeV/c isolated track. However, within the statistical errors R_{isotrk} is the same between the $Z^0 \rightarrow \ell^+\ell^-$ data and PYTHIA Monte Carlo samples. For $W^\pm$ + jets background, estimated with PYTHIA, we do not apply a correction based on R_{isotrk}. R_{isotrk} in ISAJET is consistently higher than the data. Therefore, we apply a p_T dependent correction to backgrounds estimated with ISAJET Monte Carlo, Drell-Yan γ^*/Z^0 and $W^\pm W^\mp$ production.

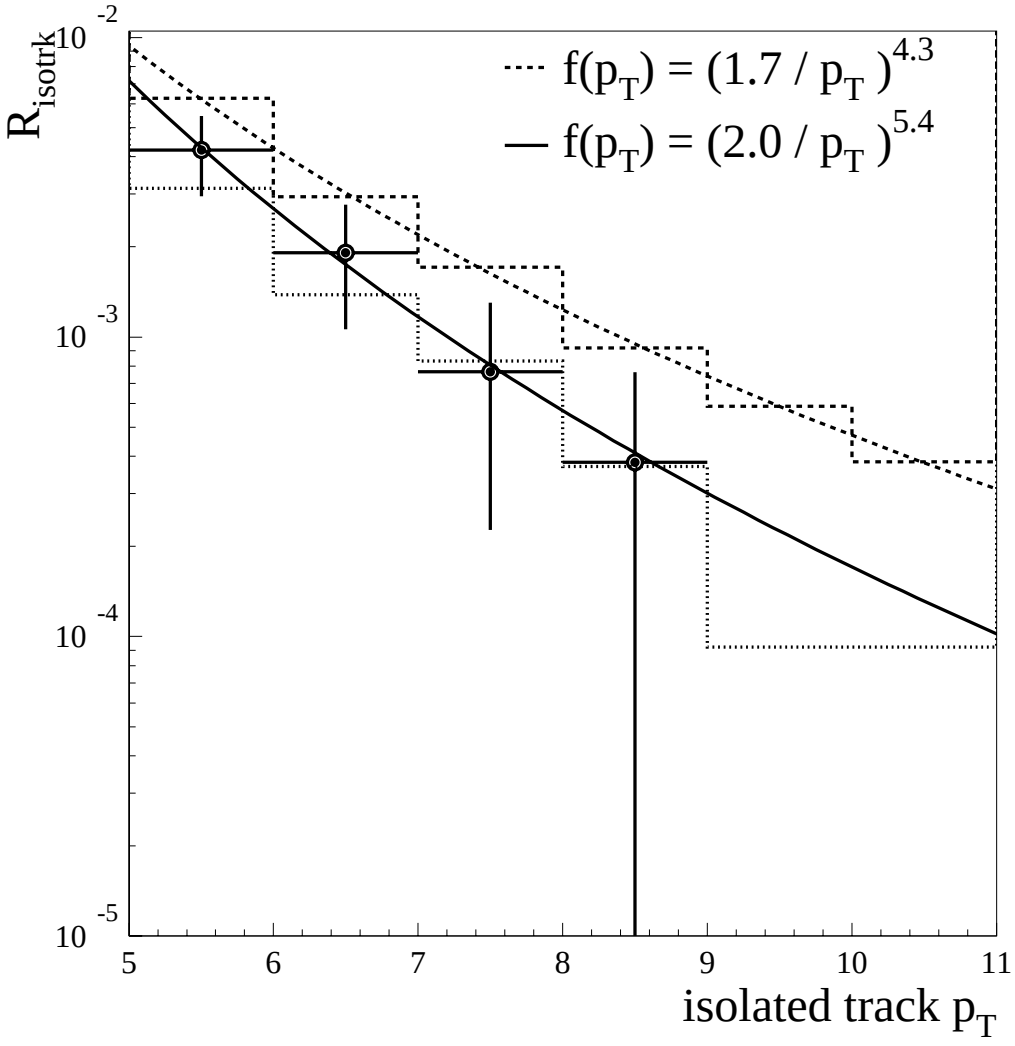

Figure 3.19: Distributions of R_{isotrk} in the ISAJET (dashed histogram), PYTHIA (dotted histogram), and data (points) $Z^0 \rightarrow \ell^+\ell^-$ samples. None of the distributions have been scaled. The errors shown on the data points assume binomial statistics.

From earlier CDF measurements of the inclusive isolated track rate, we expect the distribution of isolated tracks to fall approximately as track ${p_T}^{-6}$ [79]. Thus, we fit R_{isotrk} in data and ISAJET Monte Carlo with a falling power spectrum as a function of p_T:

$$f(p_T) = (P1/p_T)^{P2} \ , \tag{3.9}$$

where $P1$ and $P2$ are free parameters. We find $f(p_T) = ((2.0 \pm 0.6)/p_T)^{(5.4 \pm 1.3)}$ in the data with a $\chi^2 = 0.028$ per 2 degrees of freedom (four points fit with with two free parameters), consistent with the previous CDF measurements. In ISAJET, we find $f(p_T) = ((1.7 \pm 1.0)/p_T)^{(4.3 \pm 0.2)}$ with a $\chi^2 = 0.075$ per four degrees of freedom. The central values of these fits in data (solid line) and ISAJET (dashed line) are shown in Figure 3.19. When estimating the expected background in the LSD signal region, we scale down the number of lepton + track events selected from ISAJET by a correction factor, $C(p_T)$, that is defined as the ratio of the fits:

$$C(p_T) \equiv \frac{f_{data}}{f_{ISAJET}} = 4.3{p_T}^{-1.1} \ , \tag{3.10}$$

where f_{data} is the data fit and f_{ISAJET} is the ISAJET fit, using the central values of the fits. $C(p_T)$ is always less than one for $p_T > 5$ GeV/c, the region in which we select our LSD signal leptons.

3.4.4 Fake Rate

Once we have the rate of isolated tracks underlying $Z^0 \rightarrow \ell^+\ell^-$ + jets and (by assumption) $W^\pm \rightarrow \ell^\pm\nu$ + jets production, we require the probability that such an isolated track passes all of the lepton ID cuts described in Section 3.1.5 and 3.1.6, thus faking a signal lepton. We define the fake rate per isolated track:

$$P_{fake} = \frac{N_{fake}}{N_{isotrk}} \ , \tag{3.11}$$

where N_{fake} is the number of fake leptons selected in a given p_T bin and N_{isotrk} is the number of isolated tracks selected in that p_T bin. To select isolated tracks, we use the 151,452 JET20 and 83,710 JET50 events presented in Appendix B.2.4, which contain at least one low-p_T, minimally-isolated track satisfying the loose cuts given in Table B.3.

To select fake leptons we use the 292 fake electron and 237 fake muon candidates from the bias-removed JET20 and JET50 background samples presented in Appendix B.2.4. The events in these samples must pass the event quality cuts given in Table 3.3. They contain at least one loosely-isolated lepton ($ISO_{\Delta R=0.4} < 5.0$ GeV) which passes the strict electron and muon ID cuts given in Tables 3.1 and 3.2 and must pass the event quality cuts given in Table 3.3. We have removed real leptons from the e and μ candidates by removing the jet trigger bias and cutting against events consistent with leptonic decays of the $W^{\pm}$ and Z^0. We do not use minimum bias data in the P_{fake} estimate because of the low numbers of lepton candidates in that sample.

In the isolated track samples, we apply the tight $ISO_{\Delta R=0.4} < 2$ GeV and $ISO_{\Delta R=0.7} < 7$ GeV cuts to each isolated track candidate to find the number of events with an isolated track (N_{isotrk}). We also apply the $ISO_{\Delta R=0.4} < 2$ GeV and $ISO_{\Delta R=0.7} < 7$ GeV cuts to each fake lepton candidate in the fake lepton samples to find the number of events with a fake electrons or muons (N_{fake}). Tables 3.8 and 3.9 give N_{fake} for electrons and muons, respectively, and N_{isotrk} in variable p_T bins in the range $6 < p_T < 20$ GeV/c for the combined JET20 and JET50 samples. We vary the size of the p_T of the bins and combine the JET20 and JET50 samples to ensure a statistically significant sample of fake leptons in most bins.

Figures 3.20 and 3.21 show the electron and muon P_{fake} per isolated track for

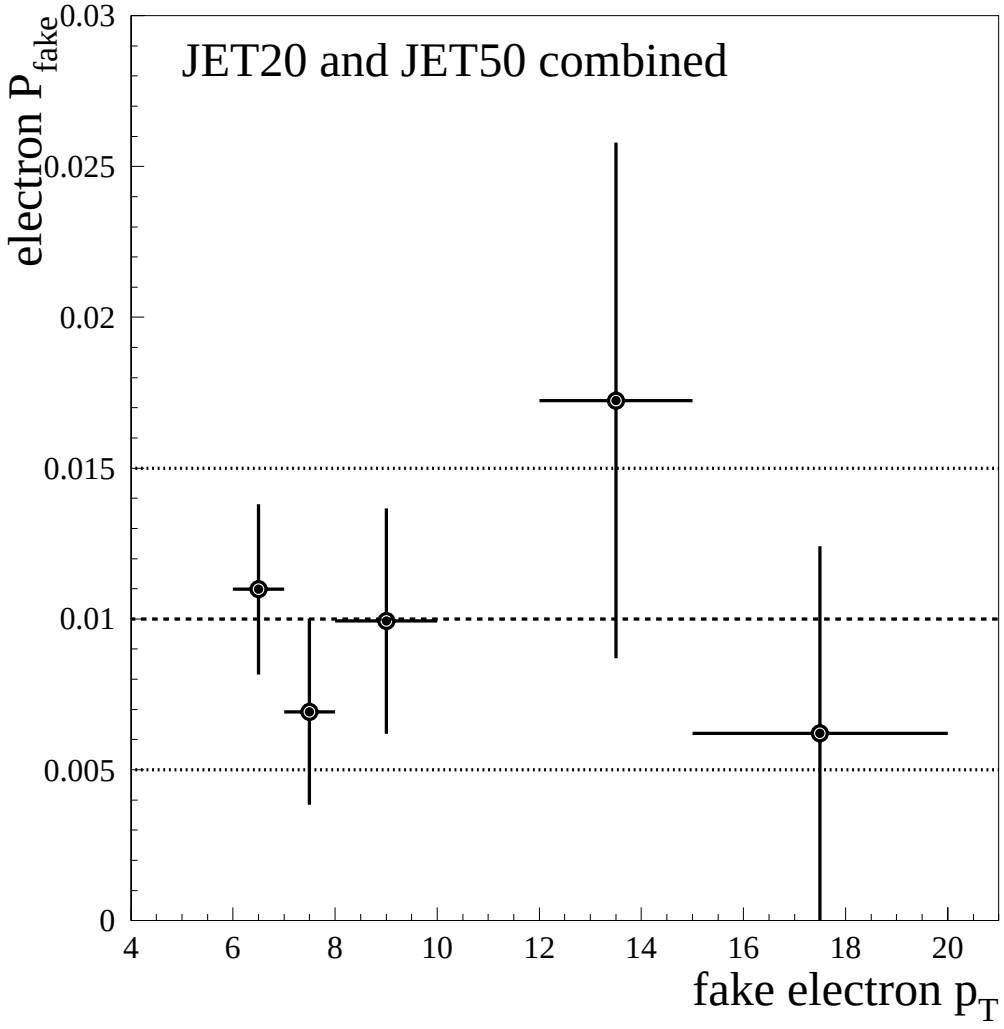

Figure 3.20: Electron fake rate (P_{fake}) per isolated track for the combined JET20 and JET50 data as a function of p_T. The errors shown on the data points assume binomial statistics. The errors shown on the fits are statistical and systematic.

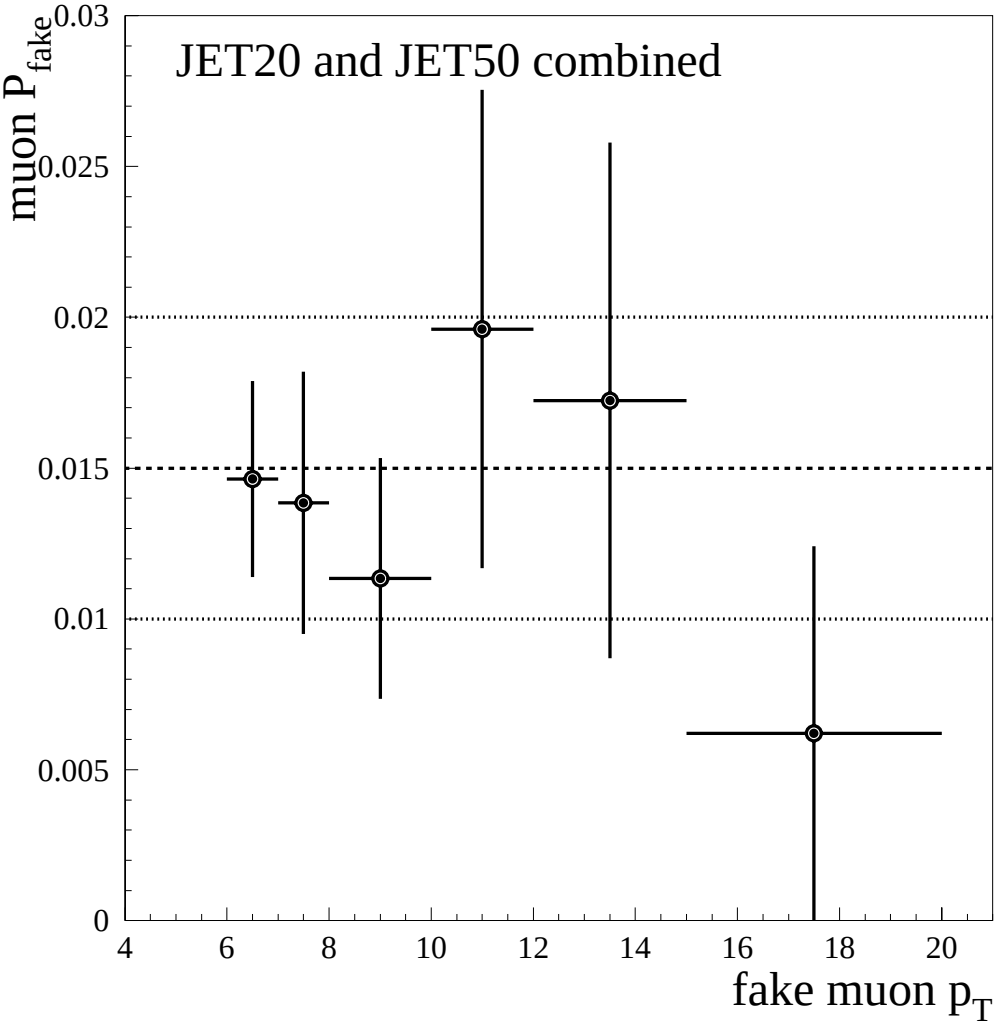

Figure 3.21: Muon fake rate (P_{fake}) per isolated track for the combined JET20 and JET50 data as a function of p_T. The errors shown on the data points assume binomial statistics. The errors shown on the fits are statistical and systematic.

p_T bin (GeV/c)	N_{isotrk}	N_{fake} electron
6-7	1366	15
7-8	722	5
8-10	705	7
10-12	306	0
12-15	232	4
15-20	161	1

Table 3.8: The number of events with an isolated track (N_{isotrk}) and selected fake electron events (N_{fake}) in increasing p_T bins in combined JET20 and JET50 data.

the combined JET20 and JET50 data as a function of p_T above 6 GeV/c. The distributions are consistent with a p_T-independent fake rate of $P_{fake} = (1.0\pm0.5)\%$ for electrons and $P_{fake} = (1.5\pm0.5)\%$ for muons, marked on the plots by the dashed lines. These are consistent with a probability of an isolated track faking a lepton (e or μ) of 1.5% per isolated track, from an early feasibility study for the LSD analysis [80]. As we do not necessarily expect JET20 and JET50 to yield identical P_{fake} values, as discussed in Refs. [38] and [78], we accept a systematic error in combining the JET20 and JET50 samples. The 0.5% error for electrons and muons includes both the statistical error from the low yield of fake lepton events in the jet data and the systematic error from combining samples. We estimate that an isolated track selected by the LSD analysis cuts has a combined probability of $(2.5\pm0.7)\%$ to fake either a signal electron or muon.

p_T bin (GeV/c)	N_{isotrk}	N_{fake} muon
6-7	1366	10
7-8	722	8
8-10	705	7
10-12	306	4
12-15	232	2
15-20	161	1

Table 3.9: The number of events with an isolated track (N_{isotrk}) and selected fake muon events (N_{fake}) in increasing p_T bins in combined JET20 and JET50 data.

3.4.5 Lepton + Fake Estimates

We select events from the $W^{\pm}W^{\mp}$, Drell-Yan γ^*/Z^0, and $W^{\pm}$ + jets Monte Carlo samples with at least one lepton passing the lepton ID cuts given in Tables 3.1 and 3.2 and a like-sign, isolated track from the TRKS bank. The initial selection cuts on the track are loose: $ISO_{\Delta R=0.4} < 2$ GeV, no cut on $ISO_{\Delta R=0.7}$, and $p_T > 4$ GeV. We do not apply the electron conversion or fiducial cuts or the muon hitmask cut to the track.

Figure 3.22 shows the p_T and $ISO_{\Delta R=0.4}$ distributions of the LS lepton and track pair in $W^{\pm}W^{\mp}$ Monte Carlo with only the event quality and resonance cuts applied. The $p_T > 11$ GeV/c and $ISO_{\Delta R=0.4} < 2$ GeV cuts are marked by the dashed lines. The high-p_T lepton distributions are consistent with selecting an e or μ from a leptonic $W^{\pm}$ decay with the momentum peak at $p_T \sim 40$ GeV/c and little energy in the $ISO_{\Delta R=0.4}$ cone. The low-p_T track distributions have rapidly falling p_T and a large amount of energy in the $ISO_{\Delta R=0.4}$ cone, consistent with

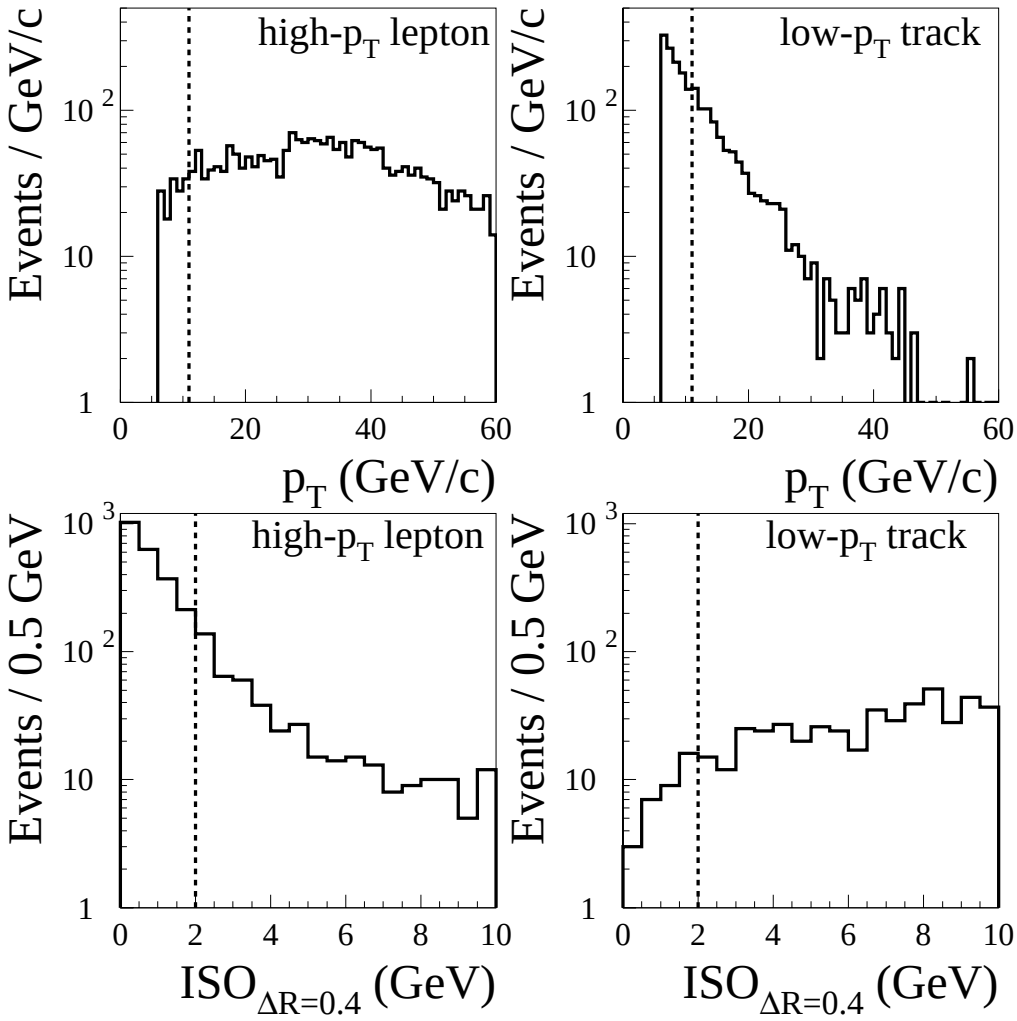

Figure 3.22: Distributions of p_T and $ISO_{\Delta R=0.4}$ for both the high-p_T lepton and low-p_T track in $W^{\pm}W^{\mp}$ Monte Carlo events prior to applying any LSD analysis cuts. The $p_T > 11$ GeV/c and $ISO_{\Delta R=0.4} < 2$ GeV cuts are marked by the dashed lines.

selecting the track from jet production. Applying the $ISO_{\Delta R=0.4} < 2$ GeV and $ISO_{\Delta R=0.7} < 7$ GeV cuts together with the $p_T > 11$ GeV/c cut removes 99% of this sample. The $W^{\pm}W^{\mp}$ Monte Carlo events are generated with ISAJET. Therefore, after applying the LSD analysis cuts, we scale the selected events by the isolated track rate correction factor, $C(p_T)$, given in Section 3.4.3 and multiply the number of selected events by $P_{fake} = (2.5 \pm 0.7)\%$ to account for the probability of the selected track in the event faking a real lepton. We then scale the Monte Carlo events to match the data luminosity to estimate $0.0003^{+0.0003}_{-0.0002}$ events in the LSD signal region from $W^{\pm}W^{\mp}$ production.

Figure 3.23 shows the p_T and $ISO_{\Delta R=0.4}$ distributions of the LS lepton and track pair in Drell-Yan γ^*/Z^0 Monte Carlo with only the event quality and resonance cuts applied. The $p_T > 11$ GeV/c and $ISO_{\Delta R=0.4} < 2$ GeV cuts are marked by the dashed lines. As in $W^{\pm}W^{\mp}$ background, the high-p_T lepton and low-p_T track distributions are consistent with selecting a real lepton and a track from jet production. Figure 3.24 shows the dilepton pair p_T distribution with the $p_T^{\ell\ell} > 20$ GeV/c cut and the LS invariant mass $m_{\ell\ell}$ distribution with the $m_{\ell\ell} > 10$ GeV/c^2 cut in the Drell-Yan γ^*/Z^0 Monte Carlo. The $m_{\ell\ell}$ cut is also effective against low-mass Drell-Yan production because one of the OS Drell-Yan γ^*/Z^0 pair may be lost, causing the OS dilepton mass cuts $m_{\ell 1 \ell 3} > 10$ GeV/c^2 and $m_{\ell 2 \ell 3} > 10$ GeV/c^2 to be ineffective. For brevity these plots include both Drell-Yan γ^* and Z^0 Monte Carlo samples described in Section 3.2.4. When estimating the Drell-Yan γ^*/Z^0 background contribution to the LSD signal region, we compute γ^* and Z^0 estimates separately and sum them to calculate the total estimated events from Drell-Yan production.

Applying the $p_T^{\ell\ell} > 20$ GeV/c and $m_{\ell\ell} > 10$ GeV/c^2 cuts removes 50% of this sample. Adding the $ISO_{\Delta R=0.4} < 2$ GeV and $ISO_{\Delta R=0.7} < 7$ GeV cuts

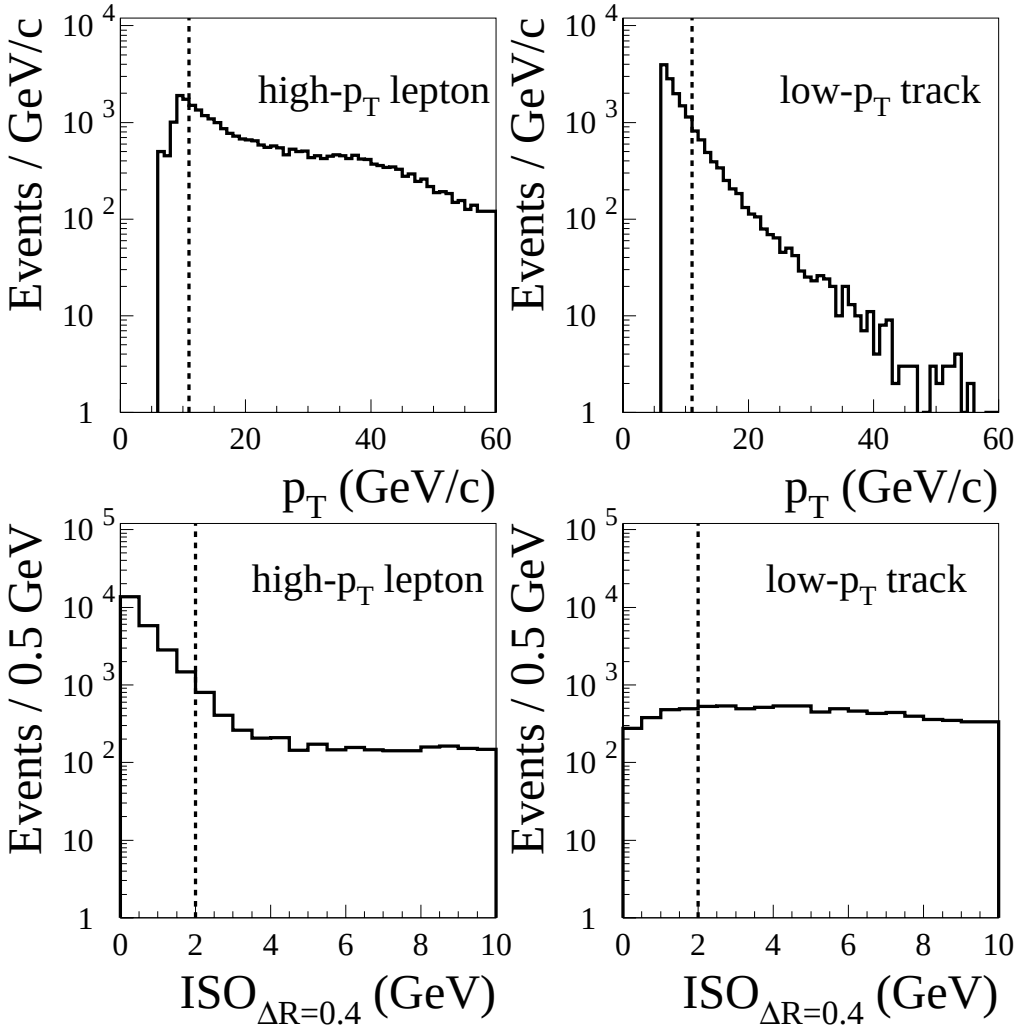

Figure 3.23: Distributions of p_T and $ISO_{\Delta R=0.4}$ for both the high-p_T lepton and low-p_T track in Drell-Yan γ^*/Z^0 Monte Carlo events prior to applying any LSD analysis cuts. The $p_T > 11$ GeV/c and $ISO_{\Delta R=0.4} < 2$ GeV cuts are marked by the dashed lines.

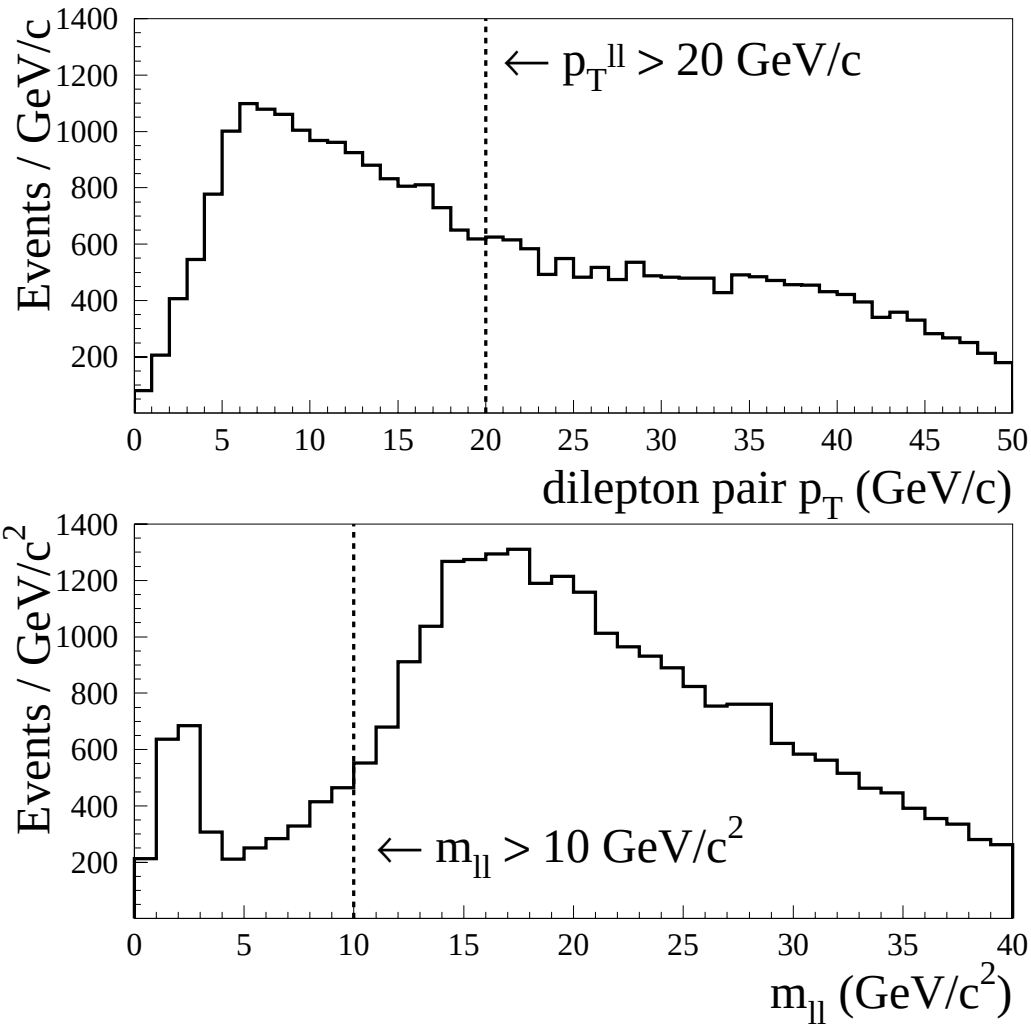

Figure 3.24: Distributions of $p_T^{\ell\ell}$ and $m_{\ell\ell}$ in Drell-Yan γ^*/Z^0 Monte Carlo events prior to applying any LSD analysis cuts. The $p_T^{\ell\ell} > 20$ GeV/c and $m_{\ell\ell} > 10$ GeV/c^2 cuts are marked by the dashed lines.

together with the $p_T > 11$ GeV/c cut removes a total of 99% of this sample. The Drell-Yan γ^*/Z^0 Monte Carlo events are generated with ISAJET. Therefore, after applying the LSD analysis cuts, we scale the selected events by the isolated track rate correction factor, $C(p_T)$, given in Section 3.4.3 and multiply the number of selected events by $P_{fake} = (2.5\pm0.7)\%$ to account for the probability of the selected track in the event faking a real lepton. We then scale the Monte Carlo events to match the data luminosity to estimate $0.03^{+0.10}_{-0.01}$ events in the LSD signal region from Drell-Yan γ^*/Z^0 production.

Figure 3.25 shows the p_T and $ISO_{\Delta R=0.4}$ distributions of the LS lepton and track pair in $W^{\pm}$ + jets Monte Carlo with only the event quality and resonance cuts applied. The $p_T > 11$ GeV/c and $ISO_{\Delta R=0.4} < 2$ GeV cuts are marked by the dashed lines. As in $W^{\pm}W^{\mp}$ background, the high-p_T lepton and low-p_T track distributions are consistent with selecting a real lepton from a leptonic $W^{\pm}$ decay and a track from additional jet production. Applying the $ISO_{\Delta R=0.4} < 2$ GeV and $ISO_{\Delta R=0.7} < 7$ GeV cuts together with the $p_T > 11$ GeV/c cut removes 99% of this sample. After applying the LSD analysis cuts, we multiply the number of selected events by $P_{fake} = (2.5\pm0.7)\%$ to account for the probability of the selected track in the event faking a real lepton. We then scale the Monte Carlo events to match the data luminosity to estimate 0.30 ± 0.07 events in the LSD signal region from $W^{\pm}$ + jets production, making this the largest background in the signal region.

Table 3.10 gives the number of expected events estimated from the Monte Carlo in the LSD signal region from each of the SM processes contributing to the LSD signature. We expect a total of $0.63^{+0.12}_{-0.07}$ from these processes.

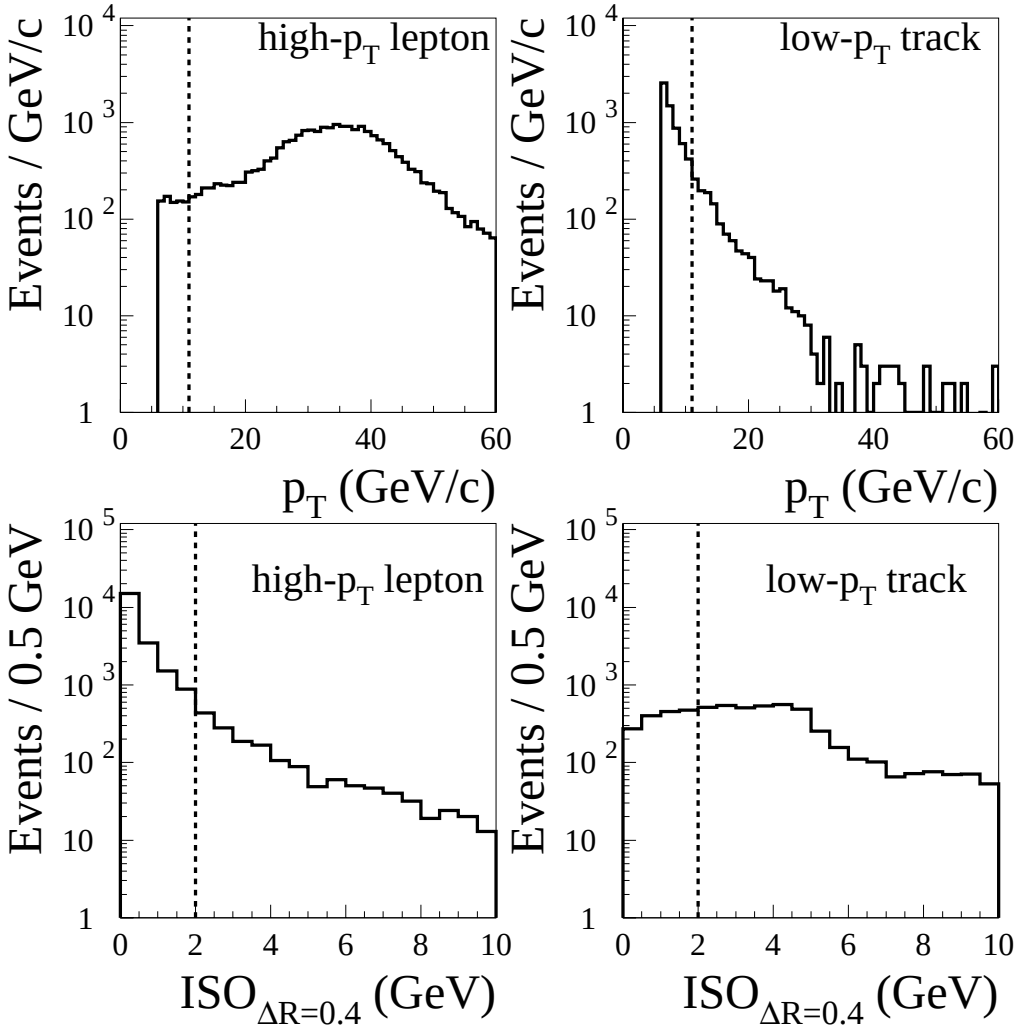

Figure 3.25: Distributions of p_T and $ISO_{\Delta R=0.4}$ for both the high-p_T lepton and low-p_T track in $W^{\pm}$ + jets Monte Carlo events prior to applying any LSD analysis cuts. The $p_T > 11$ GeV/c and $ISO_{\Delta R=0.4} < 2$ GeV cuts are marked by the dashed lines.

Process	expected events
Drell-Yan (γ^*/Z^0)	$0.03^{+0.10}_{-0.01}$
$W^{\pm}W^{\mp}$	$0.0003^{+0.0003}_{-0.0002}$
$W^{\pm}Z^0$	0.229 ± 0.004
Z^0Z^0	0.061 ± 0.001
$W^{\pm}$ + jets	0.30 ± 0.07
$t\bar{t}$	$0.008^{+0.006}_{-0.004}$
$b\bar{b}$	$0.0^{+0.001}_{-0.0}$
total	$0.63^{+0.12}_{-0.07}$

Table 3.10: Number of expected events estimated from the Monte Carlo in the LSD signal region from each SM process.

3.4.6 Difake

We use data sidebands adjacent to the LSD signal region to estimate the contribution of events with both LS dileptons selected from misidentified jets. Figure 3.26 shows the events selected in control regions adjacent to the LSD signal region in $p_T^{\ell\ell}$ versus p_T of the second LS lepton space. All of the LSD analysis cuts have been imposed on the data *except* the minimum p_T cut on the second LS lepton or the dilepton pair p_T cut have been inverted: $p_T < 11$ GeV/c and $p_T^{\ell\ell} < 20$ GeV/c. As the minimum p_T on the second LS lepton and dilepton pair p_T cuts remove most of the lepton + fake background, this space is most sensitive to events selected with at least one fake lepton. There are no events in the shaded $p_T < 6$ GeV/c region due to the minimum p_T cut in the lepton ID requirements. Due to the inverted minimum p_T and dilepton pair p_T analysis cuts we cannot observe events in the shaded LSD signal region.

Region	Background(s)	Expected background	Data
A	W+jets	$0.03^{+0.06}_{-0.01}$	1
B	$W^{\pm}Z^0$, Z^0Z^0	0.1 ± 0.1	0
C	$b\bar{b}$, Drell-Yan	$0.3^{+0.4}_{-0.2}$	14
D	$W^{\pm}$ + jets, Drell-Yan	0.6 ± 0.4	10
E	$W^{\pm}$ + jets, Drell-Yan	3.5 ± 1.0	4

Table 3.11: Events selected in data sidebands adjacent to the LSD signal region in $p_T^{\ell\ell}$ versus p_T of the second LS lepton space before including the difake estimate of QCD dijet background.

We estimate the expected background in each adjacent control region, labeled A-E, from all dilepton and lepton + fake background processes contributing to the LSD analysis exactly as presented in Sections 3.4.1 and 3.4.2, respectively. The number of expected background and observed events in each adjacent control region are summarized in Table 3.11. The primary background(s) contributing to the number of expected events are noted in the Table. We observe that the number of selected events in the data is not predicted correctly, especially in regions A, C, and D. As these are the control regions with the lowest values of p_T and $p_T^{\ell\ell}$, where we expect to observe primarily low-p_T difake background, we assume that the excess in observed events is due to QCD dijet backgrounds from two jets which have been misidentified as the LS dilepton pair.

Without a suitable Monte Carlo to describe QCD dijets production, we use data sidebands adjacent to both the LSD signal region and the regions shown in Figure 3.26 to estimate the contribution of events with both LS dileptons selected from misidentified jets. We examine the data sideband adjacent to the signal region defined by inverting the nominal LSD ISO requirement, $ISO_{\Delta R=0.4} < 2\,\mathrm{GeV}$

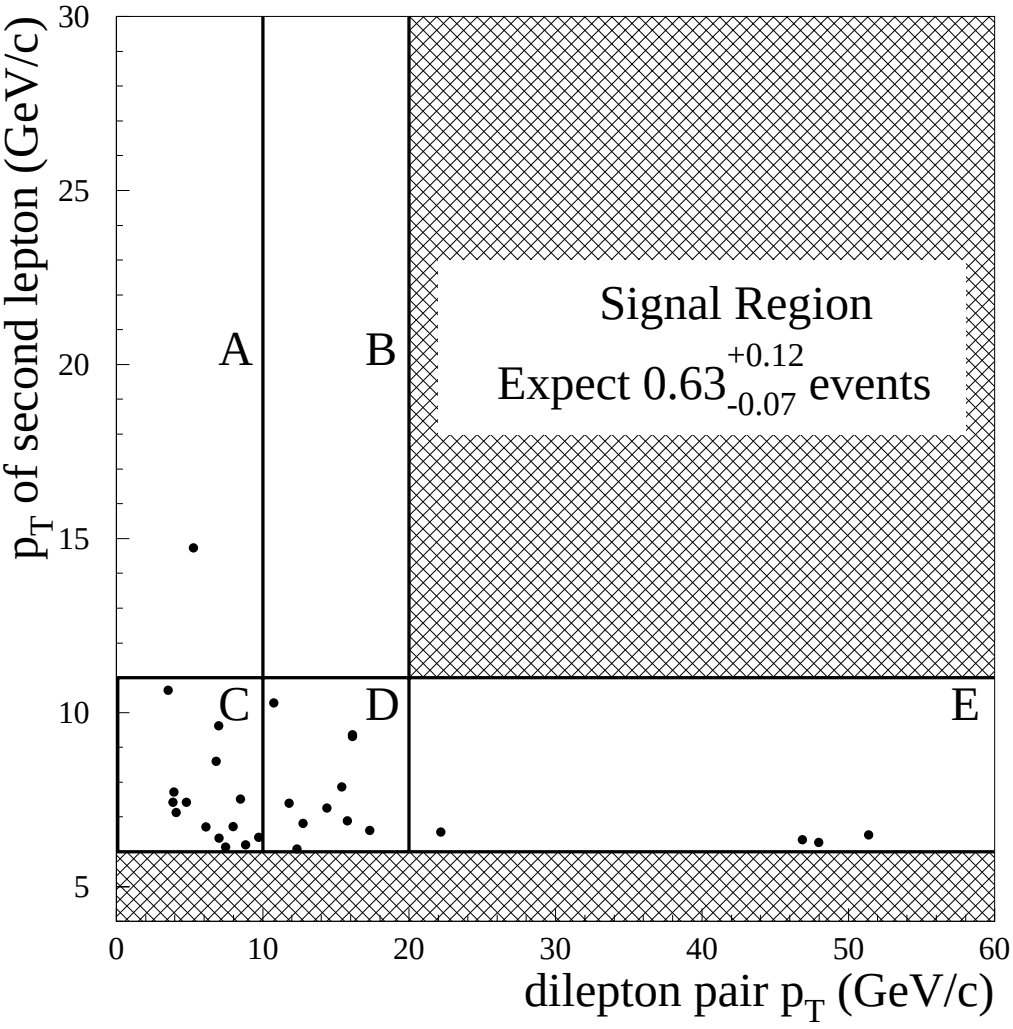

Figure 3.26: Events selected in data sidebands adjacent to the LSD signal region in $p_T^{\ell\ell}$ versus p_T of the second LS lepton space.

and $ISO_{\Delta R=0.7} < 7$ GeV, on the high-p_T lepton in the LS dilepton pair. The energy topology in the ISO cone is well-studied in Appendix D and shown to be highly efficient in retaining isolated, signal-like leptons while rejecting leptons associated with jet production. Thus, the number of events which fail the ISO cut in a given data sample can also provide an unbiased handle with which to predict event yields from jet background passing the ISO cut in that sample.

3.4.7 Isolation Ratio

As shown in Figures B.15, B.16, B.17, and B.18, the energy distribution in the ISO cone distinguishes well between signal-like and fake lepton candidates. We quantize this distinction with the ratio of the number of events passing the nominal LSD ISO requirements, $ISO_{\Delta R=0.4} < 2$ GeV and $ISO_{\Delta R=0.7} < 7$ GeV, to the number of events failing *both* of those requirements:

$$R_{ISO} \equiv \frac{N_{sel}(passing)}{N_{sel}(failing)} \ . \tag{3.12}$$

Table 3.12 gives $N_{sel}(passing)$, $N_{sel}(failing)$, and R_{ISO} for the signal-like electron and muon candidates selected from the $Z^0 \rightarrow \ell^+\ell^-$ events presented in Appendices B.2.1 and B.2.2. As expected for high-p_T, isolated lepton samples, R_{ISO} for the signal-like leptons is significantly greater than one.

Conversely, we expect lepton candidates selected from jet samples to mostly fail the ISO requirements, with an R_{ISO} less than one. Tables 3.13 and 3.14 give $N_{sel}(passing)$, $N_{sel}(failing)$, and R_{ISO} as a function of lepton p_T for electron and muon candidates, respectively, selected from the JET20 and JET50 events presented in Appendix B.2.4.

signal-like	$N_{sel}(passing)$	$N_{sel}(failing)$	R_{ISO}
electron	2076	271	7.7 ± 0.5
muon	2352	239	9.8 ± 0.7

Table 3.12: The number of events passing the nominal LSD ISO requirements ($N_{sel}(passing)$), the number of events failing both of those requirements ($N_{sel}(failing)$), and R_{ISO} for signal-like electron and muon candidates from $Z^0 \rightarrow \ell^+\ell^-$ events.

p_T bin (GeV/c)	$N_{sel}(passing)$	$N_{sel}(failing)$	R_{ISO} fake electron
5-8	36	37	0.97 ± 0.23
8-11	7	14	0.50 ± 0.23
11-20	5	15	0.33 ± 0.17

Table 3.13: The number of events passing the nominal LSD ISO requirements ($N_{sel}(passing)$), the number of events failing both of those requirements ($N_{sel}(failing)$), and R_{ISO} as a function of electron p_T for fake electron candidates from JET20 and JET50 events.

3.4.8 Difake Estimate

We invert the $ISO_{\Delta R=0.4} < 2$ GeV and $ISO_{\Delta R=0.7} < 7$ GeV cuts on the high-p_T lepton of the LS dilepton pair. We use the high-p_T lepton because the dilepton and lepton + fake backgrounds are selected with real, signal-like high-p_T leptons. However, by definition the difake background is selected with a high-p_T fake lepton from jet production. Thus, we assume that event yields estimated from the inverted ISO cut on the high-p_T lepton sideband do not double count difake

p_T bin (GeV/c)	$N_{sel}(passing)$	$N_{sel}(failing)$	R_{ISO} fake muon
5-8	30	13	2.31 ± 0.77
8-11	12	13	0.92 ± 0.37
11-20	7	11	0.64 ± 0.31

Table 3.14: The number of events passing the nominal LSD ISO requirements ($N_{sel}(passing)$), the number of events failing both of those requirements ($N_{sel}(failing)$), and R_{ISO} as a function of muon p_T for fake muon candidates from JET20 and JET50 events.

backgrounds with lepton + fake or real dilepton backgrounds.

We calculate the expected number of events with the high-p_T lepton passing the ISO cut with:

$$N_{expected} = R_{ISO} \times N_{failing} = \frac{N_{sel}(passing)}{N_{sel}(failing)} \times N_{failing} \ , \qquad (3.13)$$

where $N_{expected}$ is the number of expected events passing the ISO cut, R_{ISO} is taken from the fake electron and muon data, and $N_{failing}$ is the number of events failing the ISO cut. Thus, we use R_{ISO} from the jet background samples to estimate the number of expected events in the LSD signal region from the number of observed events in the data sideband defined by $ISO_{\Delta R=0.4} > 2$ GeV and $ISO_{\Delta R=0.7} > 7$ GeV applied to the high-p_T lepton.

For Equation 3.13, we require R_{ISO} from the jet background samples that can be applied to lepton candidates with $p_T > 11$ GeV/c to be consistent with the LSD leptons. Figures 3.27 and 3.28 show the R_{ISO} distributions for fake electron and muon candidates, respectively, as a function of lepton p_T. In general, as p_T increases R_{ISO} decreases. If we use the entire $p_T > 5$ GeV/c sample of

Region	Background(s)	Expected background	Data
A	QCD dijet	$2.2^{+1.8}_{-1.5}$	1
B	$W^{\pm}Z^0$, Z^0Z^0	$0.1^{+0.9}_{-0.1}$	0
C	QCD dijet	19.7 ± 8.4	14
D	QCD dijet	10.0 ± 4.5	10
E	$W^{\pm}$ + jets, QCD dijet	$6.0^{+1.6}_{-1.3}$	4

Table 3.15: Events selected in data control regions adjacent to the LSD signal region in $p_T^{\ell\ell}$ versus p_T of the second LS lepton space after including the difake estimate of QCD dijet background.

fake lepton candidates to calculate R_{ISO}, we will bias the result with the lower-p_T leptons. However, we do not have enough events in the jet sample with lepton $p_T > 11$ GeV/c to obtain R_{ISO} with acceptable statistical errors. Therefore, we use fake leptons with $p_T > 8$ GeV/c to calculate $R_{ISO} = 0.41 \pm 0.14$ for fake electron candidates and $R_{ISO} = 0.79 \pm 0.24$ for fake muon candidates with statistical errors of $\sim 30\%$, marked on Figures 3.27 and 3.28 by the dashed lines.

We apply this technique to regions A-E shown in Figure 3.26. In each region we invert ISO cuts on the high-p_T lepton in the sample. We multiply the number of selected electron candidates by $R_{ISO} = 0.41 \pm 0.14$ and the number of selected muon candidates by $R_{ISO} = 0.79 \pm 0.24$ to calculate the number of expected background events in each region from QCD dijet background. We combine the expected events from difake background with the dilepton and lepton + fake backgrounds given in Table 3.11 and summarize the total expected background in each region in Table 3.15. We find good agreement between the observed events and the number of expected events from combined dilepton, lepton + fake, and difake backgrounds.

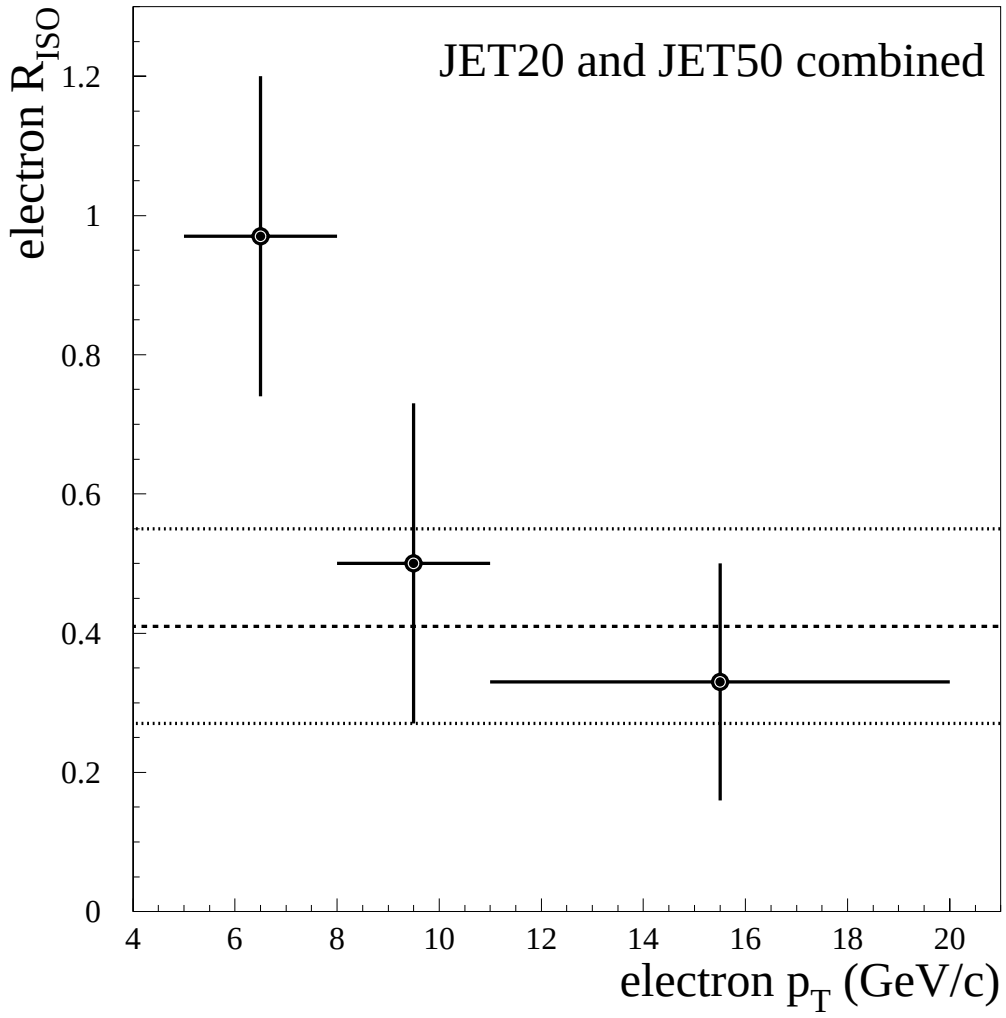

Figure 3.27: R_{ISO} distribution for fake electron candidates selected from the JET20 and JET50 datasets as a function of electron p_T. The value of electron $R_{ISO} = 0.41 \pm 0.14$ is marked by the dashed lines.

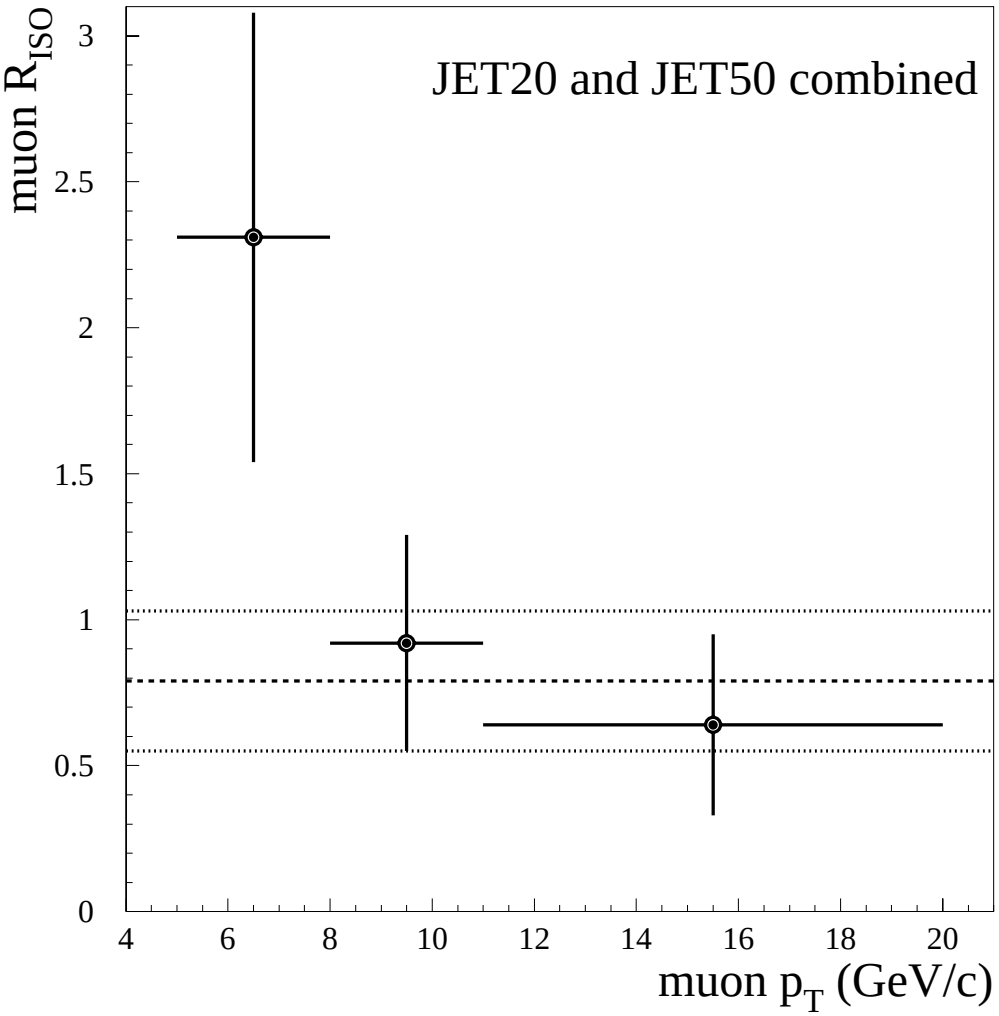

Figure 3.28: R_{ISO} distribution for fake muon candidates selected from the JET20 and JET50 datasets as a function of muon p_T. The value of muon $R_{ISO} = 0.79 \pm 0.24$ is marked by the dashed lines.

Finally, we apply this technique to the LSD signal region to estimate the difake event contribution to the signal region. We invert the $ISO_{\Delta R=0.4} < 2$ GeV and $ISO_{\Delta R=0.7} < 7$ GeV cuts on the high-p_T lepton in the LS dilepton pair and select no events. Thus, we expect $0.0^{+0.83}_{-0.0}$ events from QCD dijet production in the signal region, which is equivalent setting a 1σ Poisson upper limit on expected events from difake production. Combining this limit with the total number of expected events in the signal region from dilepton and lepton + fake backgrounds given in Table 3.10, we expect a total of $0.63^{+0.84}_{-0.07}$ events in the LSD signal region.

3.5 Around the Box Estimates

The good agreement between the background predictions (from Monte Carlo and data sidebands) and observed events in the data for the regions in Table 3.15 indicates that we are correctly estimating the lepton + fake and difake backgrounds near the LSD signal region. Thus, we expect that the Monte Carlo and data sideband background estimates for QCD dijet and $W^{\pm}$ + jets production in the LSD signal region are accurate. We can test the background predictions "around the box" in other regions near the LSD signal region to check the accuracy of the other background estimates in the LSD signal region. Aside from $W^{\pm}$ + jets, the largest SM background production estimates in the signal region come from diboson $W^{\pm}Z^0$ and Z^0Z^0 production.

3.5.1 Inverted Z^0 Resonance

We invert the Z^0 resonance cut defined in Section 3.3.1 to check the Monte Carlo estimates of diboson $W^{\pm}Z^0$ and Z^0Z^0 production. We require that the LSD candidate events have a third OS lepton ($\ell 3$) in the event with an in-

Process	expected events
Drell-Yan (γ^*/Z^0)	0.002 ± 0.001
$W^\pm W^\mp$	$0.0^{+0.001}_{-0.0}$
$W^\pm Z^0$	0.071 ± 0.002
$Z^0 Z^0$	0.035 ± 0.001
$W^\pm$ + jets	$0.0^{+0.01}_{-0.0}$
$t\bar{t}$	$0.0^{+0.004}_{-0.0}$
$b\bar{b}$	$0.0^{+0.001}_{-0.0}$
total	$0.11^{+0.01}_{-0.002}$

Table 3.16: Number of expected events estimated from the Monte Carlo in the Z^0 resonance range from each SM process.

variant mass reconstructed with either of the LS leptons ($\ell 1$ or $\ell 2$) of either 81 GeV/c^2 $< m_{\ell 1 \ell 2} <$ 101 GeV/c^2 or 81 GeV/c^2 $< m_{\ell 2 \ell 3} <$ 101 GeV/c^2. Table 3.16 summarizes the number of expected events in this region from all SM processes. Because of the low production cross sections for $W^\pm Z^0$ and $Z^0 Z^0$ processes and the low efficiency to select all three leptons from an event with three leptons, we expect only $0.11^{+0.01}_{-0.002}$ events in this region, entirely from processes containing Z^0 production. We observe 0 events in the data, consistent with the Monte Carlo background predictions.

3.5.2 OS Dilepton Pair + Track

We invert the LS cut described in Section 3.1.7 to require events with an opposite-sign dilepton pair: $Q_1 \times Q_2 = -1$. These events are dominated by OS dilepton Drell-Yan (γ^*/Z^0) production, although all SM backgrounds which

Process	expected events
Drell-Yan (γ^*/Z^0)	64 ± 8
$W^{\pm}W^{\mp}$	0.9 ± 0.1
$W^{\pm}Z^0$	0.127 ± 0.003
Z^0Z^0	0.073 ± 0.001
$W^{\pm}$ + jets	$0.0^{+0.6}_{-0.0}$
$t\bar{t}$	2.1 ± 0.1
$b\bar{b}$	$0.6^{+0.8}_{-0.4}$
total	68 ± 9

Table 3.17: Number of expected events estimated from the Monte Carlo in the OS dilepton pair + track region from each SM process.

contain a OS dilepton pair contribute to this region.

To make this region relevant to the LSD signal region, we further require each OS dilepton event to have a low-p_T, minimally-isolated track using the cuts to select isolated track candidates given in Table 3.6. This track will have the same sign as one of the OS leptons. With this region we are checking the estimate of backgrounds which have an OS lepton pair plus a track which may be selected as a fake LS lepton with either of the OS pairs. These backgrounds include Drell-Yan (γ^*/Z^0), $W^{\pm}W^{\mp}$, and heavy flavor $t\bar{t}$ and $b\bar{b}$ production. Table 3.17 summarizes the number of expected events in this region from all SM processes. We expect 68 ± 9 events in this region. We observe 62 events in the data, consistent with the Monte Carlo background predictions.

We expect a total of $0.63^{+0.84}_{-0.07}$ events in the LSD signal region from all SM backgrounds in 107 pb^{-1} of data from Monte Carlo and data sideband background predictions. The success of these predictions in the $p_T^{\ell\ell}$ versus p_T of the

second LS lepton regions combined with the correct predictions in the inverted Z^0 resonance and OS dilepton + track regions gives us confidence in the accuracy of the expected background predicted in the LSD signal region.

CHAPTER 4

Results

There is something fascinating about science. One gets such wholesale returns of conjecture out of such a trifling investment of fact. [81]

We expect a total of $0.63^{+0.84}_{-0.07}$ events in the LSD signal region from all SM backgrounds in 107 pb^{-1} of CDF Run I data. We have achieved this low number of predicted events without anticipating a specific model of event production from physics beyond the SM. Instead, we use a minimal number of kinematic cuts to remove SM backgrounds from the signal region, as summarized in Table 3.5.

We apply the LSD analysis cuts discussed in Section 3.3 to the 21,743 LSD candidate events remaining in the dilepton dataset after the electron and muon ID cuts and the event quality cuts have been applied. We observe zero events in the data, consistent with the SM background predictions from Monte Carlo samples and data control regions. Thus, we observe no evidence for physics beyond the SM in the LSD channel. We proceed to set exclusion limits on potential models of particle production beyond the SM with the final state $\ell^{\pm}\ell^{\pm} + X$.

4.1 Exclusion Limits

In high-energy physics, exclusion limits on new particle production are generally expressed at the 95% Confidence Level (CL). We assume that the signal

events from all models of particle production follow Poisson statistics. The Poisson probability to observe N events is:

$$\beta(N) = \frac{\mu^N e^{-\mu}}{N!} \ , \tag{4.1}$$

where μ is the expected mean number of signal events [82]. In the LSD analysis we observe $N = 0$ events in the data, yielding $\beta(0) = e^{-\mu}$.

The CL upper limit on the mean number of signal events is usually expressed as $100 \times (1 - \beta(N))\%$, given the observation of N events. To achieve a 95% CL upper limit, we require $\beta(N) = 0.05$. Thus, from pure Poisson statistics we find the 95% CL upper limit on the expected mean number of signal events is $\mu \equiv \bar{N}_{95} = 3.0$ events for the $N = 0$ events observed in the LSD analysis. However, this does not account for the systematic uncertainties present on the observation of $N = 0$ events, which must be included.

4.1.1 Systematic Uncertainties

We use a Bayesian approach to include systematic uncertainties in the 95% CL upper limit. This technique convolves the discrete Poisson distribution given in Equation 4.1 with a continuous Gaussian smearing distribution with a width determined by the total systematic uncertainty [83]. This is known as a 95% Bayesian CL; hereafter 95% CL refers to the 95% Bayesian CL. Following the methodology of previous analyses, the sources of systematic uncertainty include:

- The error on measuring the lepton trigger efficiency. The CDF trigger is not fully-efficient to pass e and μ events, *i.e.* not every event that should have passed a given leptonic trigger does so. The Run I e and μ trigger efficiencies were found to be:

$$\epsilon_e^{trig} = (87.3^{+3.8}_{-4.9})\% \tag{4.2}$$

$$\epsilon_{\mu}^{trig} \;=\; (87.1 \pm 2.9)\% \;, \tag{4.3}$$

for a total error on the lepton trigger efficiency measurement of ±5.6%.

- The error on the total integrated luminosity acquired by CDF during Run I. As measured by the BBC the error was found to be ±7.2%.

- The error on measuring the lepton ID efficiency. The lepton ID cuts described in Sections 3.1.5 and 3.1.6 have an combined efficiency to identify e and μ of $\epsilon^{leptonID} = (86.4 \pm 1.9)\%$.

These errors are summed in quadrature for a total systematic uncertainty from the luminosity and trigger and lepton ID efficiencies of ±9.3% [58].

The errors given for the $0.63^{+0.84}_{-0.07}$ expected events in the LSD signal region are primarily due to the statistical limitations of the Monte Carlo and data sideband samples. However, these errors are a systematic uncertainty on the number of events observed in the data. Thus, they are also taken into account as the error on the expected number of background events in the Bayesian model. We also include systematic uncertainties from the structure function (PDF) choice and the Q^2 dependence of those functions, which depend on the particular model of physics beyond the SM for which we set limits.

These errors cause $\bar{N}_{95}$ to increase from 3.0 by approximately 10% for the models considered here. Once we have chosen the structure functions and calculated the PDF and Q^2 uncertainties, we determine the new value of $\bar{N}_{95}$ for each model of particle production from physics beyond the SM considered.

4.1.2 Cross Section Upper Limit

In order to determine if we should have observed events from a given model of particle production beyond the SM, we require an upper limit on the production

cross section in the LSD channel for the new physics, given the observation of 0 events. We also express the cross section upper limit at the 95% CL. With $\bar{N}_{95}$, we define the 95% CL upper limit on the production cross section:

$$\bar{\sigma}_{95} \cdot \mathrm{BR}(\ell^{\pm}\ell^{\pm} \ + \ X) \equiv \frac{\bar{N}_{95}}{\epsilon_{tot} \cdot \int \mathcal{L} \ dt} \ , \tag{4.4}$$

where BR is the LS dileptonic branching ratio, ϵ_{tot} is the total event acceptance, and $\int \mathcal{L} \ dt = 107 \ \mathrm{pb}^{-1}$.

4.1.3 Total Event Acceptance

The total event acceptance, ϵ_{tot}, depends on the point of theory phase space under consideration. To determine ϵ_{tot}, we first generate enough signal Monte Carlo simulated by QFL to select a statistically significant number of $\ell^{\pm}\ell^{\pm} + X$ events with the LSD analysis cuts at a point in the phase space of theory. We expect that the signal Monte Carlo has the correct production cross section and leptonic decay parameters for the new particles as given by the theory. As we did for the background Monte Carlo estimates in the signal region, we then scale the number of selected events by the QFL lepton efficiency correction factor, C_{QFL}, defined in Section 2.2.7 and the Monte Carlo trigger weight, W_{trig}, defined in Section 2.2.9 to get N_{sel}, the number of selected signal events.

The ϵ_{tot} also includes the efficiencies for lepton ID and trigger ID given in Section 4.1.1. With N_{sel}, we define the total event acceptance for a given set of parameters in the theory phase space:

$$\epsilon_{tot} \ \equiv \ \frac{N_{sel}}{N_{tot}} \times \epsilon^{trig} \times \epsilon^{leptonID} \ , \tag{4.5}$$

where N_{tot} is the total number of generated signal Monte Carlo events at that point in phase space. As $\frac{N_{sel}}{N_{tot}}$ is the efficiency for the LSD analysis cuts to select

events from the Monte Carlo, ϵ_{tot} can thus be interpreted as the total acceptance per event for the LSD channel.

At each point in theory phase space, a model predicts a production cross section, σ_{theory}, and a leptonic BR. If $\bar{\sigma}_{95} \cdot \mathrm{BR}(\ell^{\pm}\ell^{\pm} + X)$ given by Equation 4.4 is less than $\sigma_{theory} \cdot \mathrm{BR}(\ell^{\pm}\ell^{\pm} + X)$ at a given point in the phase space of theory, then we should have observed an excess of events in the data from that point. The value of $\bar{\sigma}_{95}$ can thus be interpreted as the upper limit on the production cross section allowed by the observed number of events in the data being consistent with the SM background prediction. Regions of a theory with predicted production cross sections higher than $\bar{\sigma}_{95}$ are excluded at the 95% CL.

4.2 WZ-like Production

As we perform this search without considering any one particular model for new physics, we can evaluate the result as a general limit on particle production leading to the LS dilepton signature. We set limits on "WZ-like" particle production, using massive, charged bosons with the standard couplings and spins of the $W^{\pm}$ and Z^0. These bosons can decay leptonically to $\ell = e$ or μ via $W^{\pm} \rightarrow \ell^{\pm}\nu$ and $Z^0 \rightarrow \ell^{+}\ell^{-}$. However, we allow the masses of the W-like and Z-like particles to vary from 75 to 300 GeV/c^2.

It is important to note that while we have tried to make this limit as general as possible, we are nevertheless tied to Standard Model-dependent assumptions when evaluating WZ-like events. Thus, while the LSD analysis was a model-independent search for physics beyond the SM, this and any other limit we set is tied to a particular model, as discussed in Section 1.3. In particular, some theories of physics beyond the SM predict exotic resonance peaks of

the $W^{\pm}$ and Z^0 bosons heavier than the 80.4 and 91.2 GeV/c^2 masses in the SM, respectively. For example, the as-yet unobserved Z' has a predicted mass 250 GeV/c^2 $< m_{Z'} <$ 2 TeV/c^2 with SM strength couplings [84, 85]. This resonance has been excluded up to $m_{Z'} > 412$ GeV/c^2 at the 95% CL by previous searches at CDF during Run I of the Tevatron [86], well above the mass range we are considering in the WZ-like model.

However, this limit comes from a search for excess in the tail of the OS dilepton invariant mass distribution, $m_{\ell\ell}$ as defined in Section 3.3.1, for combined $\ell = e$ and μ channels. Although the Z-like particle in our WZ-like model is already excluded by the OS dilepton channel, the LS dilepton analysis provides a separate, non-degenerate channel with which to study heavy WZ-like particles. Thus, this limit provides both an example of a general limit on particle production leading to the LS dilepton signature and new information in parallel with previously published results.

4.2.1 Efficiency

We generate 5,000 WZ-like events using PYTHIA version 6.157 at intervals of 25 GeV/c^2 from 75 to 300 GeV/c^2 for both the W-like and Z-like particle masses. We force the W-like and Z-like particles to decay leptonically via $W \rightarrow \ell^{\pm}\nu$ and $Z \rightarrow \ell^{+}\ell^{-}$ with the SM coupling strengths. We apply the LSD analysis cuts to the Monte Carlo events at each point to obtain ϵ_{tot}. Figure 4.1 shows ϵ_{tot} as a function of W-like particle mass, m_W, for two representative points of the Z-like particle mass: $m_Z = 100$ GeV/c^2 (solid line) and 250 GeV/c^2 (dashed line). The errors on the plot show the statistical uncertainty from the event selection.

We find the efficiencies range from 3% to 8% as the W-like and Z-like masses vary from 100 to 300 GeV/c^2. Because we force the W-like and Z-like particles

to decay leptonically, these efficiencies do not include the BR imposed by the SM couplings.

We do not explicitly search for LS dilepton pairs with τ leptons. However, as we do not prevent the decays of the W-like and Z-like particles to τ, and the τ decays to electrons and muons with BR($\tau \to e\bar{\nu}_e\nu_\tau$) = (17.84±0.06)% and BR($\tau \to \mu\bar{\nu}_\mu\nu_\tau$) = (17.36±0.05)%, we can select LS dilepton pairs from e and μ from τ decays [4]. Thus, we include τ in the efficiency of the WZ-like particle selection.

As the mass of the Z-like particle approaches the Z^0 resonance peak, the Z^0 resonance cut of 81 GeV/c^2 $< m_{\ell\ell} <$ 101 GeV/c^2 discussed in Section 3.3.1 removes more LSD candidate events. Thus, the efficiency to select WZ-like events for m_Z = 100 GeV/c^2 is lower than 250 GeV/c^2. The efficiencies for both distributions generally increase as a function m_W, because the leptons produced in the W-like and Z-like particle decays become less like leptons produced in SM backgrounds as the W-like and Z-like masses increase. Thus, the LSD background removal cuts reject fewer events for the higher energy range of the WZ-like model. For example, after the LSD quality and lepton ID cuts, the mean p_T for the low-p_T lepton in the LS dilepton pair at the endpoints of the m_Z = 100 GeV/c^2 distribution are $\bar{p}_T \sim$ 25 GeV/c for m_W = 75 GeV/c^2 and $\bar{p}_T \sim$ 47 GeV/c for m_W = 300 GeV/c^2. Because of the spread of the p_T distributions, shown in Figure 4.2 along with the $p_T >$ 11 GeV/c cuts on each lepton marked by dashed lines, the LSD p_T cuts remove (13 ± 2)% of the lower energy m_W = 75 GeV/c^2 sample compared to (6 ± 1)% of the m_W = 300 GeV/c^2 sample. The remaining features of the distributions are within the spread of the statistical uncertainties.

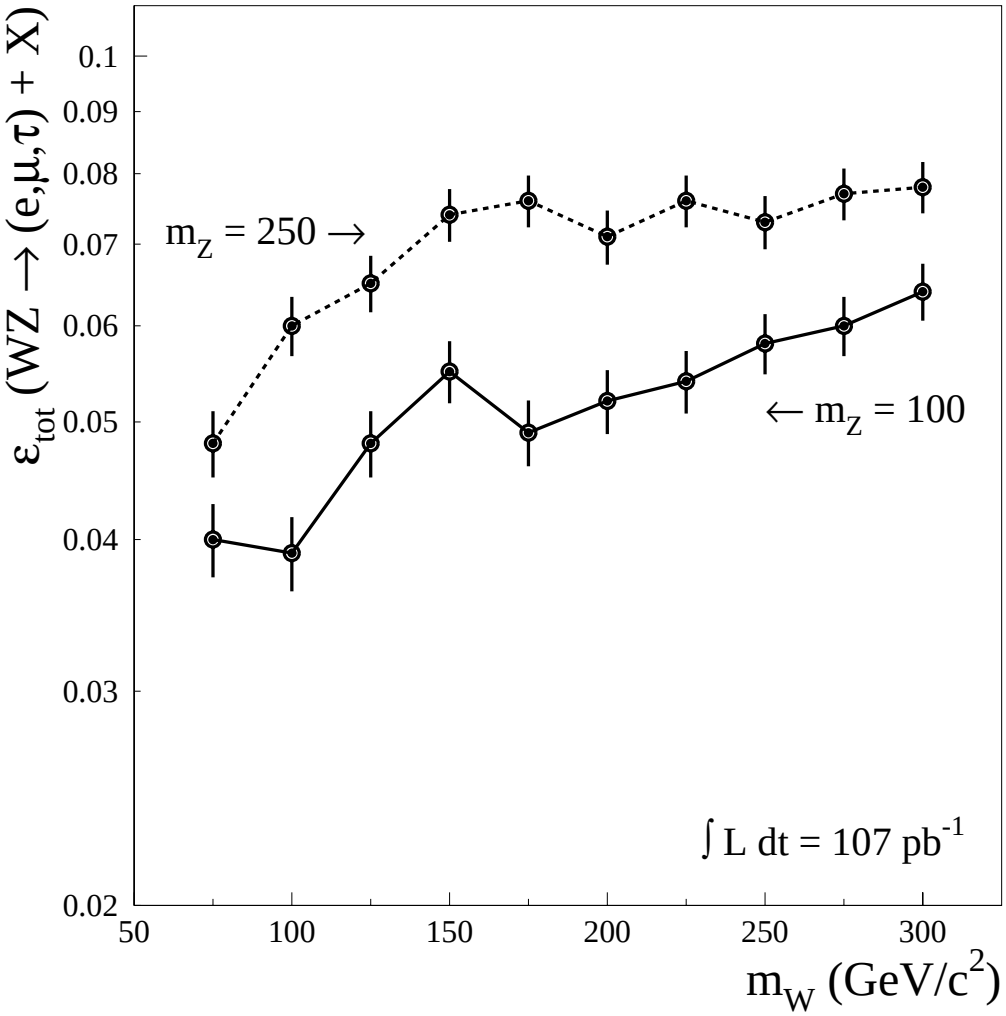

Figure 4.1: WZ-like ϵ_{tot} as a function of W-like particle mass for two representative points of Z-like particle mass: $m_Z = 100$ GeV/c^2 (solid line) and 250 GeV/c^2 (dashed line).

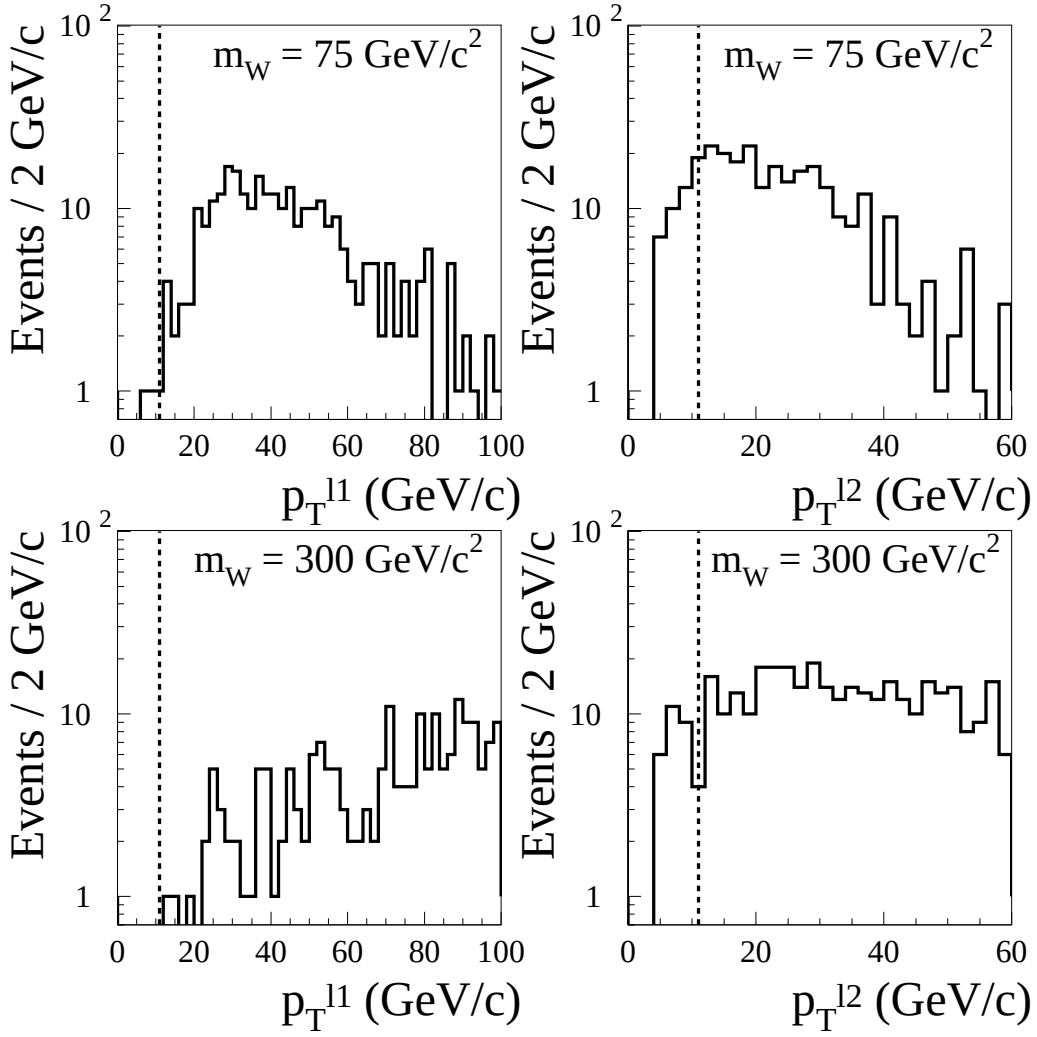

Figure 4.2: Distributions of the p_T of the high and low-p_T leptons, $\ell 1$ and $\ell 2$, respectively, in the LS dilepton pair from Monte Carlo events at $m_W = 75$ GeV/c^2 and $m_Z = 100$ GeV/c^2 (top) and $m_W = 300$ GeV/c^2 and $m_Z = 100$ GeV/c^2 (bottom). The $p_T > 11$ GeV/c cuts on each lepton are marked by the dashed lines.

4.2.2 Cross Section Limit

The systematic uncertainties on the PDF choice and the Q^2 dependence of those functions are $\pm 11\%$ and $\pm 9\%$, respectively. The total systematic uncertainty on the WZ-like model is $\pm 17\%$. From the procedure described in Section 4.1.1, we find $\bar{N}_{95} = 3.29$ for this model. We then use Equation 4.4 to calculate the 95% CL cross section upper limits for WZ-like particle production. Figure 4.3 shows $\bar{\sigma}_{95}$ as a function of m_W, for the two representative points of the Z-like particle mass discussed in Section 4.2.1: $m_Z = 100$ GeV/c^2 (solid line) and 250 GeV/c^2 (dashed line).

As we do not have a theoretical prediction for the production cross section for the WZ-like particle model, we do not set a limit on the W-like and Z-like particle masses. However, this limit on general particle production demonstrates one application of the model-independent LSD search to a model of physics beyond the SM.

4.3 mSUGRA Production

To calculate limits on mSUGRA production, we take the representative mSUGRA parameters, defined in Section 1.2.4, $\tan\beta = 3$, $\mu < 0$ and $A_0 = 0$, but allow m_0 and $m_{1/2}$ to vary. We generate mSUGRA Monte Carlo at a range of values in $m_0 - m_{1/2}$ space with PYTHIA version 6.157 and simulate the CDF detector with QFL. Rather than forcing the sparticles to decay leptonically, we allow all particles in the simulation to decay according to their calculated branching ratios [4]. Thus, charged leptons may be produced at any stage of the cascade sparticle and particle decays, allowing the LSD search to select leptons produced in any decay of mSUGRA sparticles which results in the LSD final state.

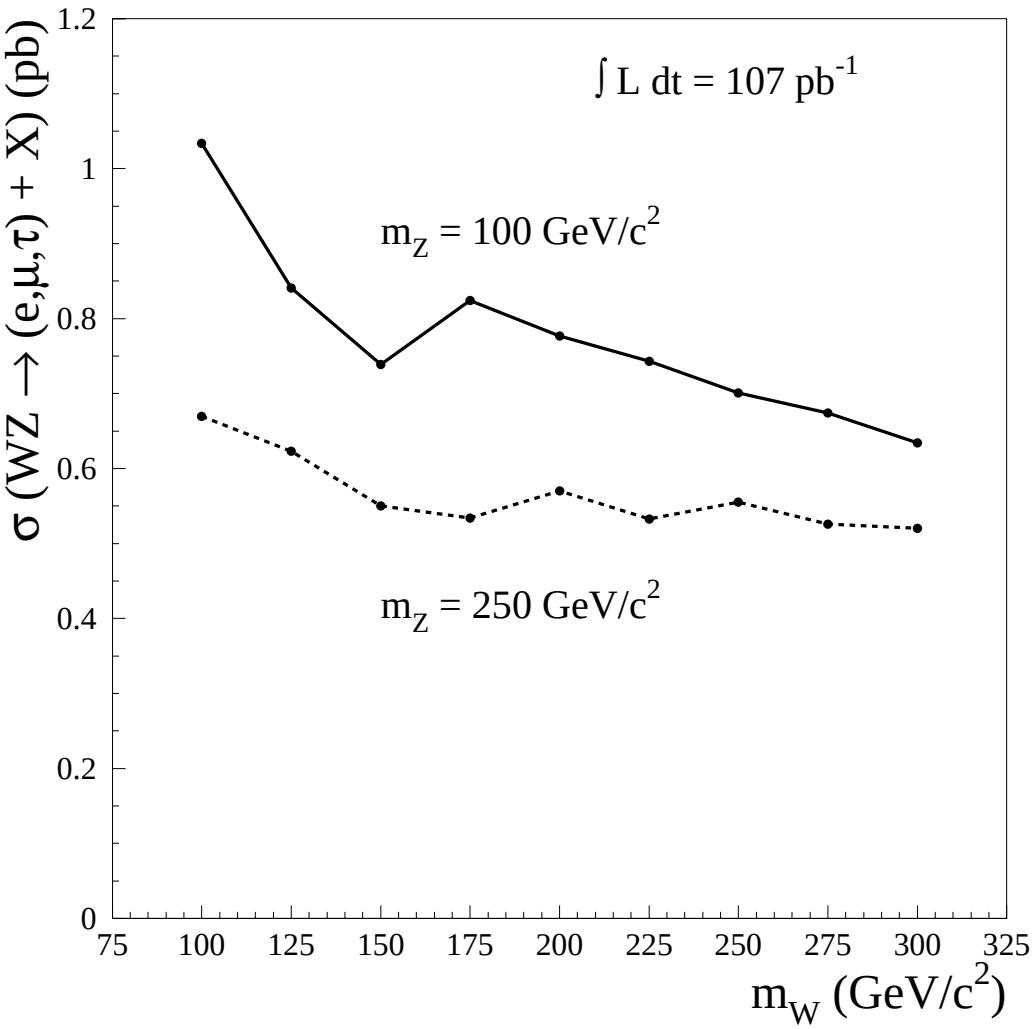

Figure 4.3: WZ-like $\bar{\sigma}_{95}$ as a function of W-like particle mass for two representative points of Z-like particle mass: $m_Z = 100$ GeV/c^2 (solid line) and 250 GeV/c^2 (dashed line).

The primary contribution to the LSD sensitivity is the mSUGRA production of charginos and neutralinos: $\tilde{\chi}_1^{\pm}\tilde{\chi}_2^0 \rightarrow \ell^{\pm}\ell^{\pm}\ell^{\mp}\tilde{\chi}_1^0\tilde{\chi}_1^0\nu$. Previous direct searches for $\tilde{\chi}_1^{\pm}\tilde{\chi}_2^0$ production of the trilepton final state have placed 95% CL upper limits on the $\tilde{\chi}_1^{\pm}$ and $\tilde{\chi}_2^0$ masses [31, 32]. The LSD analysis is sensitive as well to LS dileptons produced in cascade $\tilde{q}$ and $\tilde{g}$ decays. Direct searches for $\tilde{q}$ $\tilde{g}$ production have placed 95% CL upper limits on mSUGRA parameter space [77]. However, because we allow the leptons to be produced at any stage of the cascade decays, the LSD search may select events from other modes, such as $\tilde{\chi}_1^{\pm}$ and $\tilde{g}$ decays, yielding new information on these previously published limits.

4.3.1 Reoptimization

To use the LSD analysis to exclude mSUGRA parameter space, we reoptimize the LSD analysis cuts which define the signal region discussed in Section 3.3 for a specific signal [87]. As $\tilde{\chi}_1^{\pm}\tilde{\chi}_2^0$ is the dominant mode of mSUGRA production for which the LSD analysis is sensitive, we use this signal to reoptimize. We take the signal to be $\tilde{\chi}_1^{\pm}\tilde{\chi}_2^0$ events generated with PYTHIA with $65 < m_{\tilde{\chi}_1^{\pm}} < 105$ GeV/c^2 and force the $\tilde{\chi}_1^{\pm}$ and $\tilde{\chi}_2^0$ to decay leptonically.

We allow the dilepton pair p_T cut, nominally $p_T^{\ell\ell} > 20$ GeV/c, and the minimum-p_T cut on the second LS lepton, nominally $p_T^{\ell 2} > 11$ GeV/c, to vary while leaving all other cuts fixed. This slice of the LSD signal region is represented in Figure 4.4, which is the same slice as discussed in Section 3.4.6. From the signal Monte Carlo we calculate the expected $\bar{N}_{95}$, $\bar{N}_{95}^{exp}$, for a range of values of the cuts under consideration. We take $\bar{N}_{95}^{exp}$ along with the expected background from the signal region and sideband regions of Figure 4.4 to calculate the expected 95% CL cross section upper limit with Equation 4.4 entirely with signal Monte Carlo while stepping through a range of values for each cut.

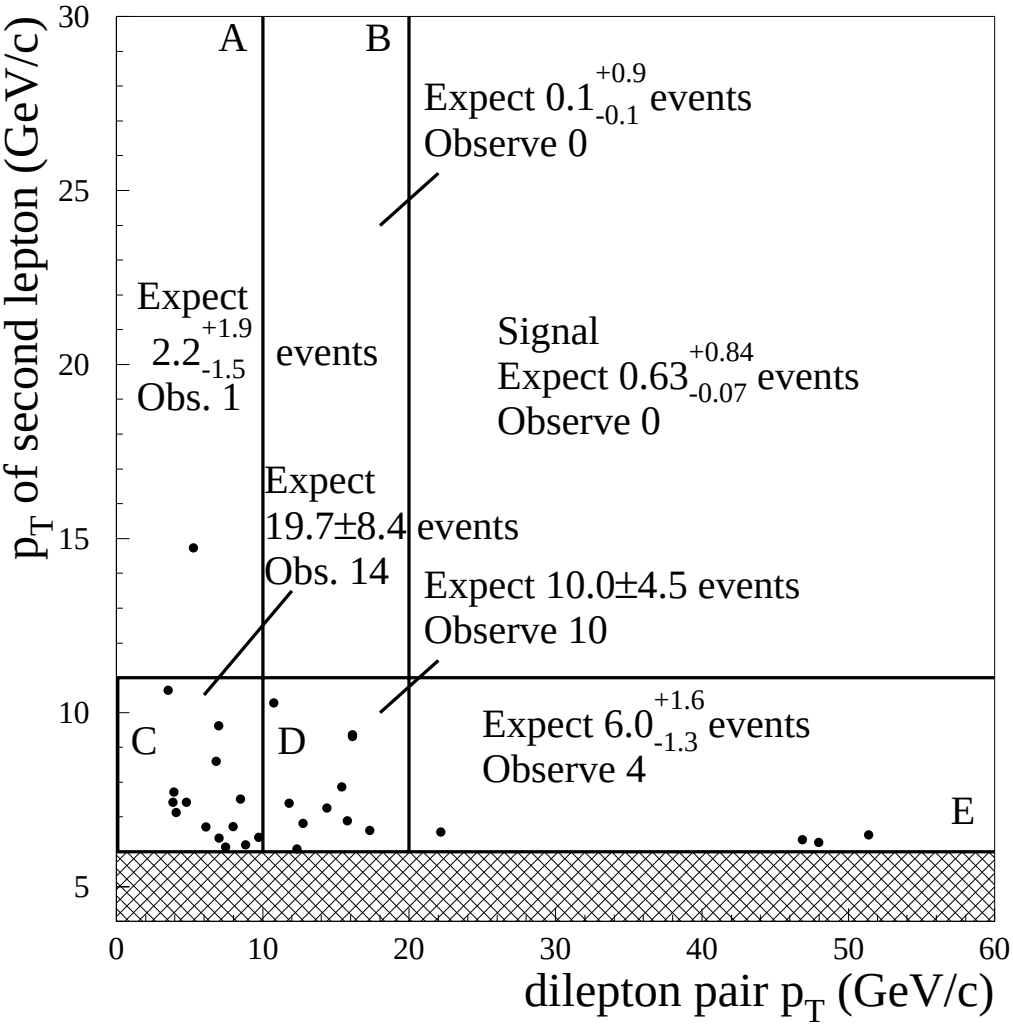

Figure 4.4: Events selected in data control regions adjacent to the previous LSD signal region in $p_T^{\ell\ell}$ versus p_T of the second LS lepton space.

We fix the optimal $p_T^{\ell\ell}$ and $p_T^{\ell 2}$ cuts to maximize $\bar{\sigma}_{95}$ for mSUGRA signal. We find that the values of $p_T^{\ell 2} > 11$ GeV/c (unchanged) and $p_T^{\ell\ell} > 10$ GeV/c, which yield an expected SM background of $0.7^{+1.2}_{-0.1}$ events, gives the optimal value of the expected $\bar{\sigma}_{95}$. We take these cuts as the nominal LSD signal region with which we report mSUGRA exclusion limits.

4.3.2 Efficiency

Figure 4.5 shows the production cross section times the total event acceptance defined in Equation 4.5 as a function of $m_{1/2}$ for four representative values of m_0. The curves show the contribution to the LSD signal from $\tilde{\chi}_1^{\pm}\tilde{\chi}_2^0$ (solid), $\tilde{q}$ $\tilde{g}$ (dashed), and $\tilde{\chi}_1^{\pm}$ $\tilde{g}$ (dotted) production modes, as well as all other production modes which contribute to the LSD sensitivity (dot-dash). As expected, $\tilde{\chi}_1^{\pm}\tilde{\chi}_2^0$ dominates. However, for small values of m_0 the $\tilde{\chi}_1^{\pm}$ and $\tilde{\chi}_2^0$ signal drops due to the $\tilde{\nu}$ becoming lighter than the $\tilde{\chi}_2^0$ mass, at which point the neutralino decays via sneutrinos and becomes invisible to detection. However, for these values of m_0 the LSD analysis recovers acceptance from other modes, primarily the heavier $\tilde{q}$ and $\tilde{g}$ cascade decays. Here the total efficiency, which includes the BR to leptons imposed by the mSUGRA model, ranges from 0.02% to 0.12%.

4.3.3 Cross Section Limit

The systematic uncertainties on the PDF choice and the Q^2 dependence of those functions are each ±9%. The total systematic uncertainty on the mSUGRA model is ±16%. From the procedure described in Section 4.1.1 and the reoptimized signal region, we find $\bar{N}_{95} = 3.40$ for this model. We then use Equation 4.4 to calculate the 95% CL cross section upper limits for mSUGRA sparticle production.

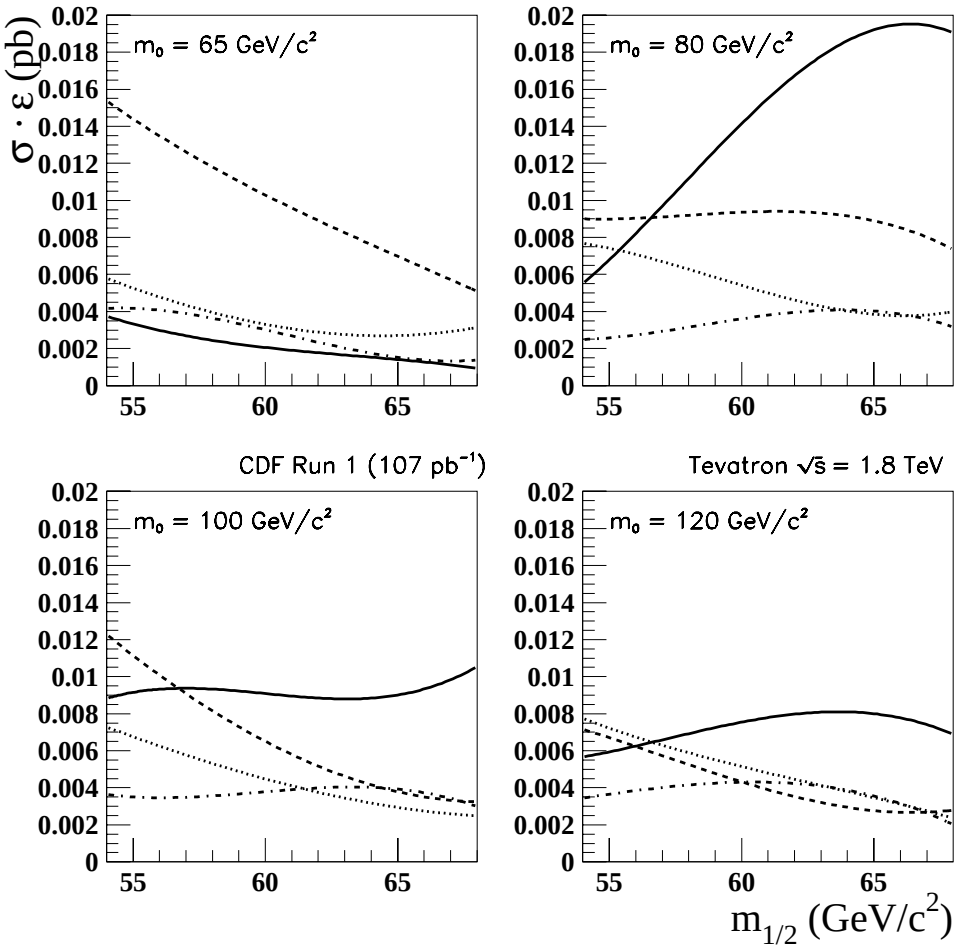

Figure 4.5: Production cross section times the total event acceptance as a function of $m_{1/2}$ for $\tilde{\chi}_1^{\pm}\tilde{\chi}_2^0$ (solid line), $\tilde{q}\ \tilde{g}$ (dashed), and $\tilde{\chi}_1^{\pm}\ \tilde{g}$ (dotted) production modes, as well as all other production modes which contribute to the LSD sensitivity (dot-dash).

Production	K
$\tilde{\chi}_1^{\pm}\tilde{\chi}_2^0$	1.30
$\tilde{q}\ \tilde{g}$	1.39
$\tilde{g}\ \tilde{g}$	1.37
$\tilde{q}\ \tilde{q}$	1.20

Table 4.1: NLO correction K factors for mSUGRA processes which dominate the LSD signal.

We compare $\bar{\sigma}_{95}$ to the predicted mSUGRA cross section, σ_{mSUGRA} from the PYTHIA Monte Carlo generated at a range of points in $m_0 - m_{1/2}$ space. As PYTHIA only includes leading-order QCD calculations [44], we correct σ_{mSUGRA} for next-to-leading order (NLO) effects for the dominant production modes by applying a scale factor (K). We generate the K with the Plehn algorithm for $\tilde{\chi}_1^{\pm}\tilde{\chi}_2^0$ production [88] and the Prospino algorithm for $\tilde{q}\ \tilde{g}$, $\tilde{g}\ \tilde{g}$, and $\tilde{q}\ \tilde{q}$ production [89]. Table 4.1 gives K for each of these processes. All other processes, which contribute little to the signal, are uncorrected ($K = 1.0$). If the NLO-corrected $\sigma_{mSUGRA} > \bar{\sigma}_{95}$, we exclude that point of mSUGRA parameter space at the 95% CL.

Figure 4.6 shows the mSUGRA 95% CL excluded region in $m_0 - m_{1/2}$ space. The shaded region is theoretically forbidden by electroweak symmetry breaking (EWSB) causing the $\tilde{\nu}$ to have unphysical masses [90]. The dip near 75 GeV/c^2 results from the loss of sensitivity to $\tilde{\chi}_1^{\pm}\tilde{\chi}_2^0$ production as the theory allows the sneutrinos ($\tilde{\nu}$) to become lighter than the $\tilde{\chi}_1^{\pm}$ and $\tilde{\chi}_2^0$. At this point the $\tilde{\chi}_1^{\pm}$ and $\tilde{\chi}_2^0$ decay to $\tilde{\nu}$, which escape detection, rather than leptonically. At lower m_0, the limit is regained due to sensitivity to $\tilde{q}\ \tilde{g}$ production decaying to leptons, as shown in Figure 4.5.

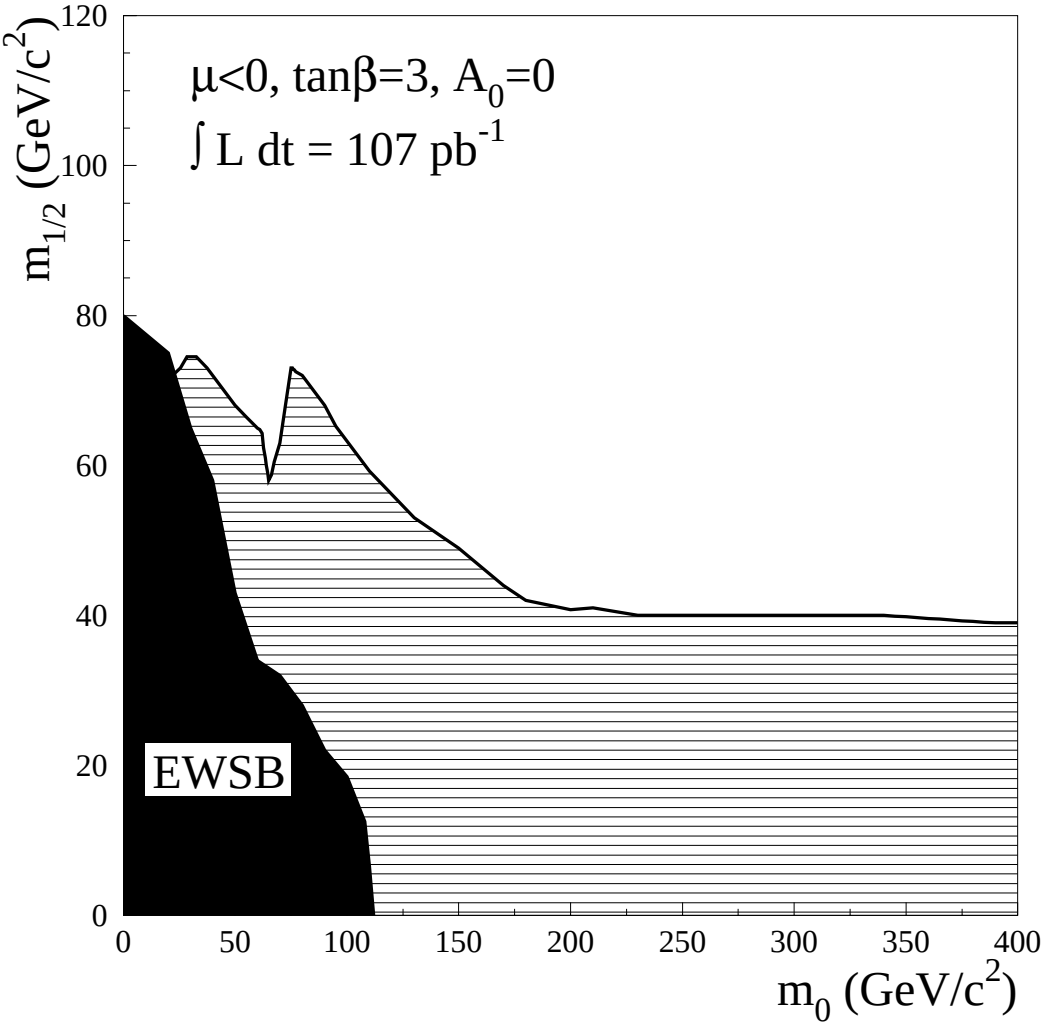

Figure 4.6: 95% CL limit region on the parameters m_0 and $m_{1/2}$ in the mSUGRA framework for $\tan\beta = 3$, $\mu < 0$ and $A_0 = 0$ (hatched region). The shaded region is theoretically forbidden by EWSB.

Previous direct searches at both CDF and DØ during Run I, based on final states containing missing transverse energy ($\not\!\!E_T$) and leptons in multijet events [91], have already excluded all of this space, assuming leptonic production from only $\tilde{q}$ $\tilde{g}$ decays. However, the inclusive LSD channel presents new information on this limit by allowing lepton production at any point in the mSUGRA decay cascade.

CHAPTER 5

Conclusion

It's all scientific stuff; it's been proved. . . . Do you see? [92]

The 107 pb^{-1} of data recorded with the CDF Run I detector at $\sqrt{s} = 1.8$ TeV has been examined for an production of events with final state $\ell^{\pm}\ell^{\pm} + X$ using a minimal number of analysis cuts. No excess above the predicted SM production has been observed and 95% CL exclusion limits in the LSD channel on quasi-generic particle and mSUGRA production have been set.

The generic particle mass ranges under consideration, 75–300 GeV/c^2, have been excluded by previous searches with the CDF Run I detector [86]. The mSUGRA parameter space excluded has previously been covered by direct SUSY searches with the CDF and DØ Run I detectors [77, 91]. However, the inclusiveness of the LSD search yields new information on the previous exclusion limits.

Studies have shown that combining the results from the LSD channel with direct search channels will improve the sensitivity to new physics signals at CDF Run II [38]. This technique can extend the discovery potential for physics beyond the SM at not only CDF and DØ during Run II of the Tevatron, but also the Large Hadron Collider at CERN [35] and the proposed Next Linear Collider [93]. Thus, inclusive searches such as the LSD analysis will make important contributions to direct searches for well-motivated theories such as SUSY, while retaining the potential to observe an unexpected new type of particle production.

APPENDIX A

Abbreviations

QFT	Quantum Field Theory
QCD	Quantum Chromodynamics
eV	electron volt (= 1.602×10^{-19} Joule)
SM	Standard Model
SUSY	Supersymmetry
LSP	Lightest Supersymmetic Particle
MSSM	Minimal Supersymmetric Standard Model
mSUGRA	minimal Supergravity
LSD	Like-Sign Dilepton
$p\bar{p}$	proton-antiproton
CDF	Collider Detector at Fermilab
LINAC	Linear Accelerator
$\sqrt{s}$	center-of-mass energy (= 1.8 TeV at the Fermilab Tevatron)
$\mathcal{L}$	instantaneous luminosity ($\mathrm{cm}^{-2}\mathrm{s}^{-1}$)
σ	cross section
pb	picobarns (= 10^{-24} cm^2)
VTX	Vertex Time Projection Chamber
CTC	Central Tracking Chamber

CEM	Central Electromagnetic Calorimeter
CHA/WHA	Central and Wall Hadronic Calorimeter
CMU/CMP	Central Muon Detectors
CMX	Central Muon Extension
PMT	photomultiplier tube
HTDC	Hadron Time-to-Digital Converters
QFL	CDF detector simulation
CFT	Central Fast Tracker
BBC	Beam-Beam Counters
$\int \mathcal{L}\, dt$	time integrated luminosity (pb^{-1})
ELES	Electron data bank
CMUO	Muon data bank
TRKS	Tracking data bank
CL	Confidence Level
ϵ	efficiency
PDF	parton distribution functions
NLO	next to leading order
EWSB	electroweak symmetry breaking

APPENDIX B

Isolation Improvement

Several leptonic SUSY searches at CDF, including $\tilde{\chi}_1^{\pm}\tilde{\chi}_2^0$ production and squark-gluino cascade decays, use some form of lepton isolation (ISO) as an important cut against SM heavy flavor pair production ($b\bar{b}$, $t\bar{t}$) and fake leptons [31, 77]. The LSD search also uses ISO to remove events in which a jet misidentified as a lepton in combination with a real lepton fakes an LSD signal event. These lepton + fake events are primarily from processes such as $W^{\pm} \rightarrow \ell^{\pm}\nu$ + jets or $Z^0 \rightarrow \ell^+\ell^-$ + jets. In an early LSD analysis feasibility study, lepton + fake background contributed to one-half of the entire expected background, as estimated from minimum bias data [80]. Because of the importance of removing these lepton + fake backgrounds, for the LSD analysis we have improved the ISO cut to remove lepton candidates associated with jets while leaving the LSD signal efficiency unchanged [78].

B.1 Original Isolation

We define isolation (ISO) as the sum of all E_T and p_T in a cone of radius $\Delta R \equiv \sqrt{(\Delta\phi)^2 + (\Delta\eta)^2}$ around the calorimeter tower to which we extrapolate the lepton candidate track (the "seed" tower). Together $\eta - \phi$ define a space which covers the entire CDF detector. ΔR therefore defines a circle around the seed tower in this space. We sum all of the E_T deposited in the calorimeter

towers contained in this circle to give the transverse calorimeter energy, $\sum E_T$. We define the calorimeter energy of the lepton candidate, E_T^{cand}, by summing the E_T deposited in the seed tower and the two towers on either side of the seed tower in η, to account for lateral energy leakage from the seed tower:

$$E_T^{cand} \equiv E_T^{seed} + E_T^{\eta-1} + E_T^{\eta+1} \ . \tag{B.1}$$

We assume that leakage from the seed tower into either adjacent ϕ tower is minimal. We define the calorimeter ISO as the calorimeter E_T with the lepton candidate E_T removed:

$$ISO^{cal} \equiv (\sum E_T) - E_T^{cand} \ , \tag{B.2}$$

which gives the energy in the calorimeter surrounding the lepton candidate. Similarly, we sum all of the p_T from all good CTC tracks pointing inside the circle of ΔR in $\eta - \phi$ space to get the track momentum, $\sum p_T$. Subtracting the p_T of the lepton candidate track, p_T^{cand}, we find the track ISO:

$$ISO^{trk} \equiv (\sum p_T) - p_T^{cand} \ , \tag{B.3}$$

which gives the momentum in the CTC surrounding the lepton candidate. This definition is equivalent to the ISO discussed in section 3.3.4, with $E_T^{leakage} \equiv E_T^{\eta-1} + E_T^{\eta+1}$.

Several studies consider ISO^{cal} and ISO^{trk} as separate cuts on a lepton candidate [94]. However, following the Run I CDF trilepton [31] and squark-gluino [77] analyses, we sum these quantities in quadrature to find the total ISO energy in a cone of ΔR around the lepton candidate:

$$ISO \equiv \sqrt{(ISO^{cal})^2 + (ISO^{trk})^2} \ . \tag{B.4}$$

Both of these analyses use cones of $\Delta R = 0.4$ radians and require a tight cut of $ISO_{\Delta R=0.4} < 2$ GeV for all lepton candidates.

B.2 Electron, Muon, and Jet Samples

To study the ISO cut efficiencies we require clean data samples of electrons, muons, and jets. We also require that the electron and muon samples not come from inside the LSD signal region, to avoid biasing our result by tuning the ISO cut on the LSD signal. In section 3.3.1 we define a Z^0 resonance range to remove Drell-Yan γ/Z^0, $W^{\pm}Z^0$, and Z^0Z^0 backgrounds from the LSD signal region: 81 GeV/c^2 $<$ $m_{\ell\ell}$ $<$ 101 GeV/c^2. Therefore, we can use the e and μ produced in $Z^0 \rightarrow \ell^+\ell^-$ decays for electron and muon samples, assuming that they will behave like the LSD signal lepton candidates. We select jet events from both minimum bias events and dedicated jet samples with 20 and 50 GeV trigger thresholds on the jet E_T.

B.2.1 Electrons

We select high-quality $Z^0 \rightarrow e^+e^-$ events with two OS central electrons within an invariant mass range of 81 GeV/c^2 $<$ m_{ee} $<$ 101 GeV/c^2 and apply a loose ISO cut on each e: $ISO_{\Delta R=0.4}$ $<$ 5.0 GeV. The $Z^0 \rightarrow e^+e^-$ electron ID and event quality cuts are listed in Table B.1. They are similar to the LSD analysis electron ID and event quality cuts, except the E_T and p_T cuts have been raised.

Figure B.1 shows the m_{ee} distribution of the events selected with the cuts listed in Table B.1 before the invariant mass cut. The invariant mass range 81 GeV/c^2 $<$ m_{ee} $<$ 101 GeV/c^2 is marked by dashed lines. Figure B.2 shows the E_T distributions for the two legs of the Z^0 after the invariant mass cut; Figure B.3 shows the p_T distributions for the two legs of the Z^0 after the invariant mass cut. Within the 81 GeV/c^2 $<$ m_{ee} $<$ 101 GeV/c^2 range, we select 1,255

Cut	Value
E_T	$\geq$ 25.0 GeV
p_T	$\geq$ 20.0 GeV/c
E/p	$\geq$ 0.75, $\leq$ 1.5
HAD/EM	$\leq$ 0.055 + 0.045($\frac{E}{100}$)
L_{shr}	$\leq$ 0.2
Δx	$\leq$ 3.0 cm
Δz	$\leq$ 5.0 cm
χ^2_{strip}	$\leq$ 15.0
$\chi^2_{3\times3}$	$\leq$ 15.0
$\lvert z_{vertex}\rvert$	$\leq$ 60 cm
$ISO_{\Delta R=0.4}$	$\leq$ 5.0 GeV
Fiducial	true
Conversion	false

Table B.1: Electron ID and event quality cuts used to select high-quality $Z^0 \rightarrow e^+e^-$ events with two OS central electrons. We cut invariant mass 81 GeV/c^2 $< m_{ee} <$ 101 GeV/c^2 after selecting events with these cuts.

$Z^0 \rightarrow e^+e^-$ events for a total sample of 2,510 signal-like electrons.

B.2.2 Muons

As with $Z^0 \rightarrow e^+e^-$, we select high-quality $Z^0 \rightarrow \mu^+\mu^-$ events with two OS central muons within an invariant mass range of 81 GeV/c^2 $< m_{ee} <$ 101 GeV/c^2 and apply a loose ISO cut on each μ: $ISO_{\Delta R=0.4} <$ 5.0 GeV. The $Z^0 \rightarrow \mu^+\mu^-$ muon ID and event quality cuts are listed in Table B.2. They are similar to the

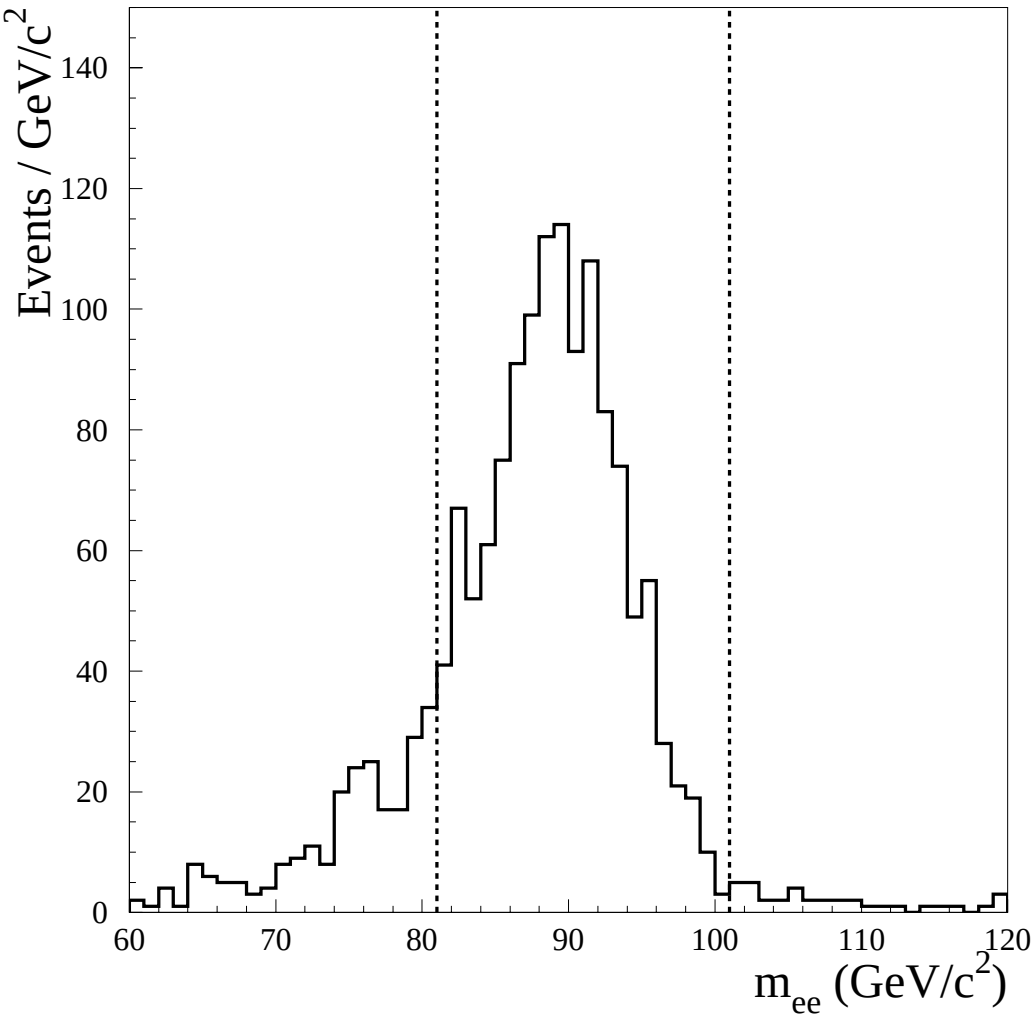

Figure B.1: Distribution of m_{ee} for $Z^0 \rightarrow e^+e^-$ events selected with the cuts listed in Table B.1. The 81 GeV/c^2 $< m_{ee} <$ 101 GeV/c^2 range is marked by dashed lines.

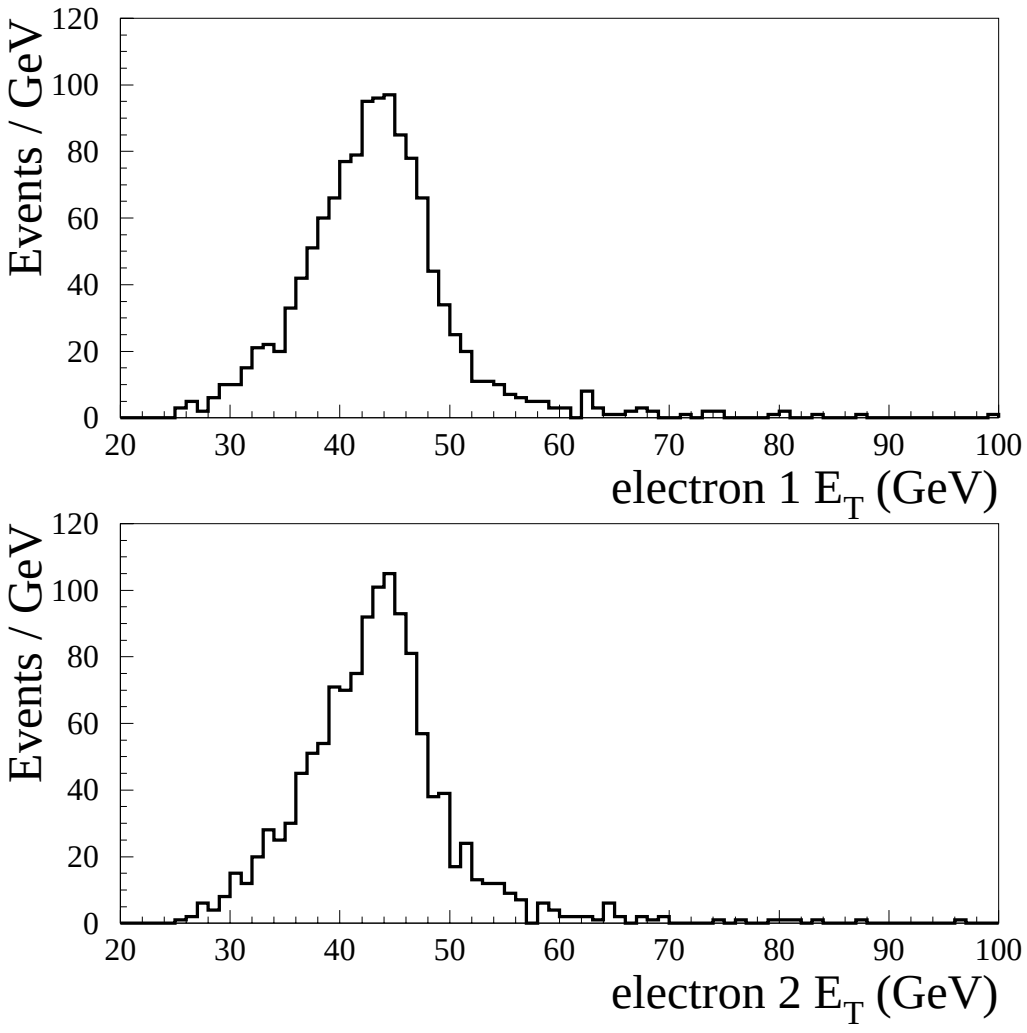

Figure B.2: Distribution of electron E_T for $Z^0 \rightarrow e^+e^-$ events selected with the cuts listed in Table B.1 after the invariant mass cut.

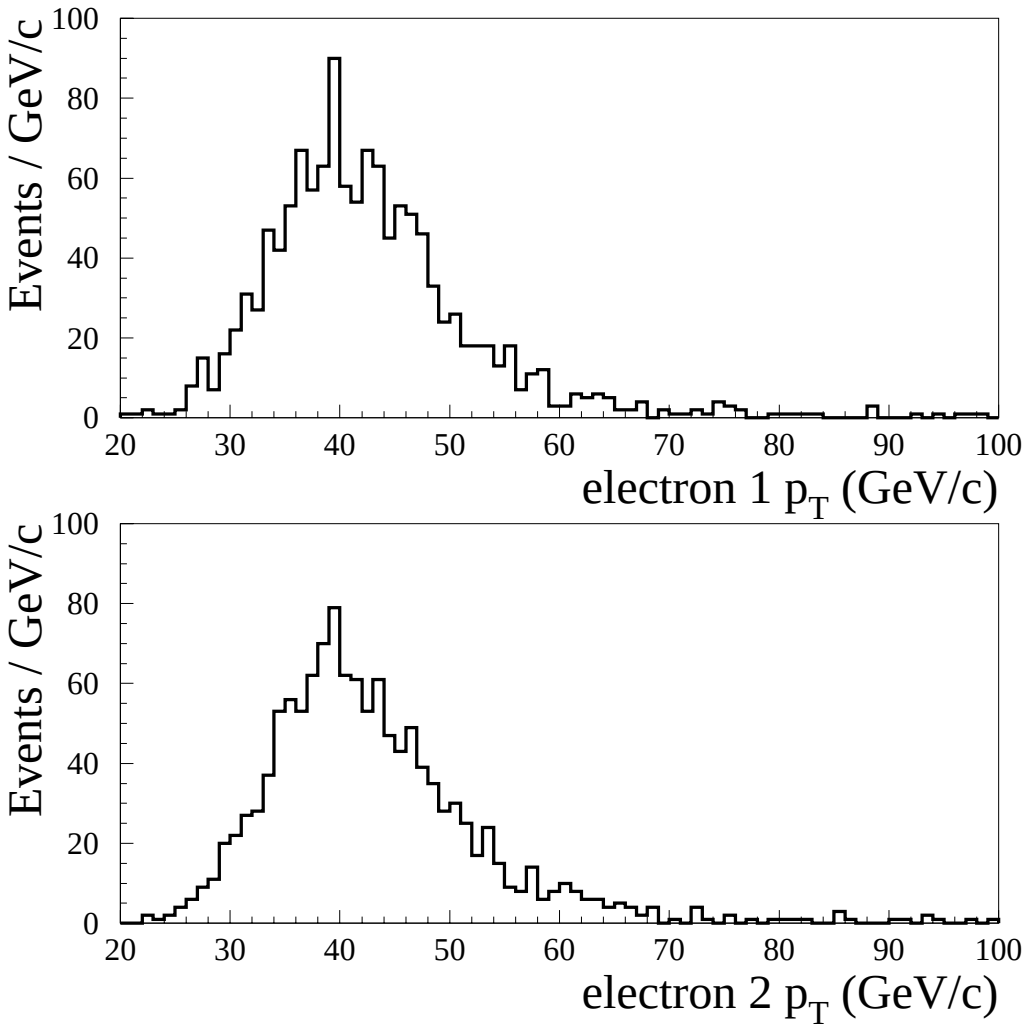

Figure B.3: Distribution of electron p_T for $Z^0 \rightarrow e^+e^-$ events selected with the cuts listed in Table B.1 after the invariant mass cut.

Cut	Value
p_T	$\geq$ 20.0 GeV/c
EM	$\leq$ 2.0 GeV
HAD	$\leq$ 6.0 GeV
d_0	$\leq$ 0.5 cm
$\lvert z_{vertex} \rvert$	$\leq$ 60 cm
$ISO_{\Delta R=0.4}$	$\leq$ 5.0 GeV
Cosmic	false
Muon hitmask	true

Table B.2: Muon ID and event quality cuts used to select high-quality $Z^0 \rightarrow \mu^+\mu^-$ events with two OS central muons. We cut invariant mass 81 GeV/c^2 $< m_{\mu\mu} <$ 101 GeV/c^2 after selecting events with these cuts.

LSD analysis muon ID and event quality cuts, except the E_T and p_T cuts have been raised.

Figure B.4 shows the $m_{\mu\mu}$ distribution of the events selected with the cuts listed in Table B.2 before the invariant mass cut. The invariant mass range 81 GeV/c^2 $< m_{\mu\mu} <$ 101 GeV/c^2 is marked by dashed lines. Figure B.5 shows the p_T distributions for the two legs of the Z^0 after the invariant mass cut. Within the 81 GeV/c^2 $< m_{\mu\mu} <$ 101 GeV/c^2 range, we select 1,389 $Z^0 \rightarrow \mu^+\mu^-$ events for a total sample of 2,778 signal-like muons.

B.2.3 Signal Efficiency

With the $Z^0 \rightarrow e^+e^-$ and $Z^0 \rightarrow \mu^+\mu^-$ samples, we calculate e and μ signal efficiencies by applying the ISO cut on each leg of the Z^0 separately. We define

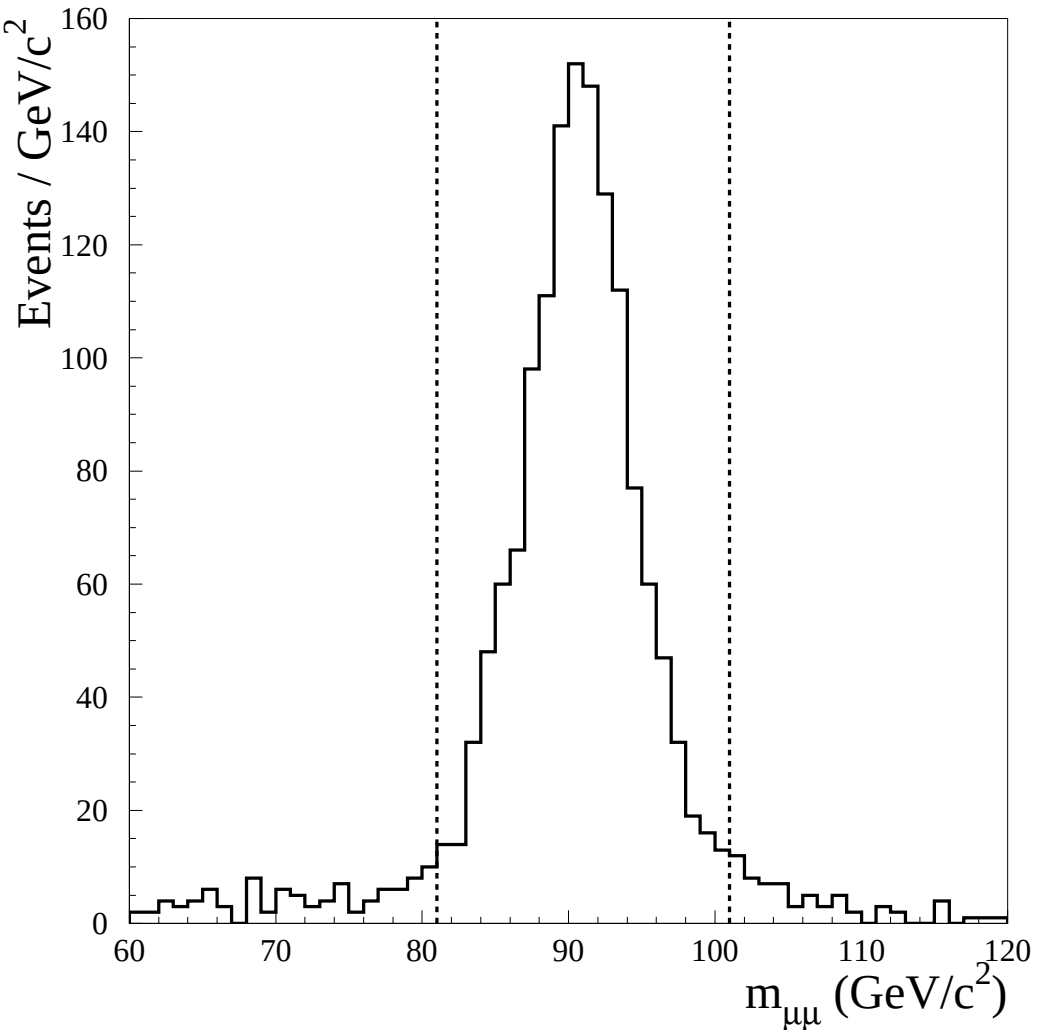

Figure B.4: Distribution of $m_{\mu\mu}$ for $Z^0 \rightarrow \mu^+\mu^-$ events selected with the cuts listed in Table B.2. The 81 GeV/c^2 $< m_{\mu\mu} <$ 101 GeV/c^2 range is marked by dashed lines.

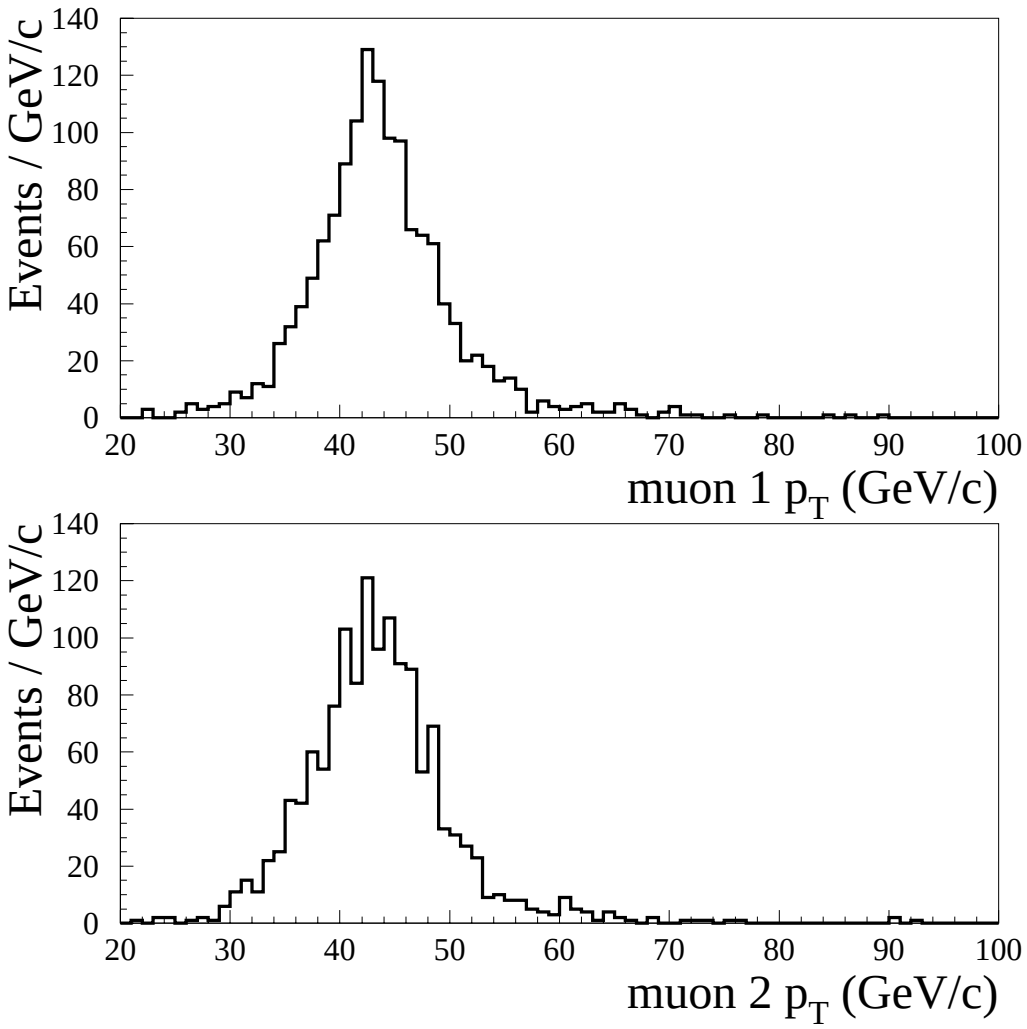

Figure B.5: Distribution of p_T for $Z^0 \rightarrow \mu^+\mu^-$ events selected with the cuts listed in Table B.2 after the invariant mass cut.

Cut	Value
p_T	≥ 3.0 GeV/c
d_0	≤ 0.5 cm
$ISO_{\Delta R=0.4}$	≤ 5.0 GeV

Table B.3: Initial cuts for a low-p_T, minimally-isolated track required to select events for minimum bias, JET20, and JET50 samples.

the signal efficiency per event as:

$$\epsilon \equiv \frac{N_1 + N_2}{2(N_{tot})} \ , \tag{B.5}$$

where N_1 and N_2 are the number of events passing the ISO cut on the first and second legs of the Z^0, respectively, and N_{tot} is the total number of events in the sample. To calculate the error on ϵ, we use:

$$\delta\epsilon = \sqrt{\frac{(N_1 + N_2)(2(N_{tot}) - (N_1 + N_2))}{8(N_{tot})^3}} \ , \tag{B.6}$$

which assumes that the event selection follows a binomial distribution [82]. We do not apply a systematic error.

B.2.4 Jets

We select jet events from both minimum bias data and dedicated jet datasets with 20 and 50 GeV trigger thresholds on the jet E_T, called JET20 and JET50, respectively. We initially require an event to have at least one low-p_T, minimally-isolated track satisfying the loose cuts given in Table B.3. With this requirement, we select 59,181 minimum bias, 151,452 JET20, and 83,710 JET50 events.

To use the jet events to estimate background from fake leptons passing the LSD lepton ID cuts, we further require each event to have at least one electron

or muon candidate which passes the strict electron and muon ID cuts given in Tables 3.1 and 3.2. We also make a loose ISO cut on each lepton candidate, $ISO_{\Delta R=0.4} < 5.0$ GeV, as we did when selecting the signal-like e and μ in section B.2.1 and B.2.2. We further require each event to pass the event quality cuts given in Table 3.3. After these cuts we are left with 37 minimum bias, 289 JET20, and 185 JET50 electron events and 31 minimum bias, 195 JET20, and 137 JET50 muon events.

We assume that the minimum bias events contain no real leptons from SM physics processes due to the generally low energy present and are therefore unbiased. Therefore, the lepton candidates selected in minimum bias events are all misidentified jets. However, the JET20 and JET50 samples are more energetic than minimum bias, and may contain real leptons from the trigger jet or from $W^{\pm} \rightarrow \ell^{\pm}\nu +$ jets or $Z^0 \rightarrow \ell^+\ell^- +$ jets processes. By selecting real leptons in a sample meant to contain only jets which are misidentified as leptons, we would bias the fake lepton background estimate.

We remove real leptons from the jet samples by first rejecting events consistent with leptonic decays of the $W^{\pm}$ or Z^0 from the jet samples. We search the remaining jet events for a second lepton passing the loose electron and muon ID cuts given in Tables 3.1 and 3.2. If a second lepton is found, we calculate the dilepton invariant mass ($m_{\ell\ell}$) as defined in section 3.3.1 for the event. We remove events consistent with $m_{\ell\ell}$ consistent with a wide Z^0 resonance peak, 61 GeV/$c^2 < m_{\ell\ell} <$ 121 GeV/c^2, to remove candidate events from $Z^0 \rightarrow \ell^+\ell^-$. Figure B.6 shows the $m_{\ell\ell}$ distributions for the minimum bias, JET20, and JET50 samples with the invariant mass range 61 GeV/$c^2 < m_{\ell\ell} <$ 121 GeV/c^2 marked by the dashed lines. Events with no second lepton have been suppressed.

To remove candidate events from $W^{\pm} \rightarrow \ell^{\pm}\nu$, we require a low missing

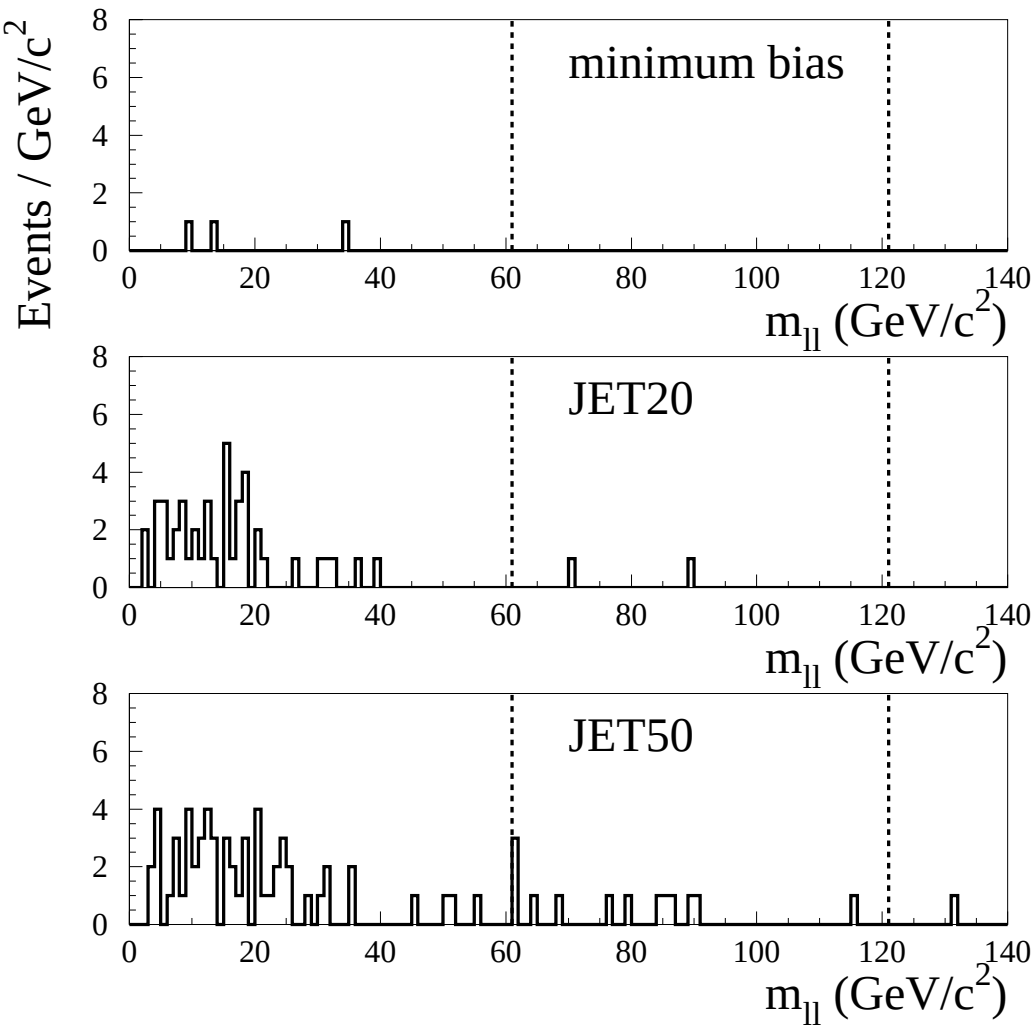

Figure B.6: Distribution of $m_{\ell\ell}$ in minimum bias, JET20, and JET50 data. The invariant mass range 61 GeV/c^2 $< m_{\ell\ell} <$ 121 GeV/c^2 is marked by the dashed lines. Events with no dilepton pair have been suppressed.

transverse energy ($\not\!\!E_T$) in the event, as $\not\!\!E_T \sim 40$ GeV indicates energy lost in the detector due to the escaping ν from the $W^{\pm} \rightarrow \ell^{\pm}\nu$ decay. Figure B.7 shows the $\not\!\!E_T$ distributions for the minimum bias, JET20, and JET50 samples with the $\not\!\!E_T < 30$ GeV cut marked by the dashed lines. We also calculate the transverse mass (m_T) of the strict e or μ candidate with which we select the jet samples:

$$m_T \equiv \sqrt{(p_T + \not\!\!E_T)^2 - (p_x + \not\!\!E_x)^2 - (p_y + \not\!\!E_y)^2} \ , \tag{B.7}$$

where p is the lepton candidate momentum and $\not\!\!E$ is the missing energy of the event. Large m_T indicates a the leptonic decay of the $W^{\pm}$. We require $m_T < 40$ GeV/c^2 to further remove candidate events from $W^{\pm} \rightarrow \ell^{\pm}\nu$. Figure B.8 shows the m_T distributions for the minimum bias, JET20, and JET50 samples with the $m_T < 40$ GeV/c^2 cut marked by the dashed lines. As we expect, as the overall amount of energy in the events increases due the higher trigger thresholds, the average values of $m_{\ell\ell}$, $\not\!\!E_T$, and m_T increase from minimum bias to JET20 to JET50. None of these cuts remove events from the low energy minimum bias sample.

The JET20 and JET50 samples also have a trigger bias which the minimum bias data does not contain due to the jet energy trigger. However, the JET20 and JET50 samples are more useful to estimate fake backgrounds due to the greater overall energy present in the jet events, caused by the jet energy trigger threshold. We assume that the lepton candidate selected in the jet samples with the strict e and μ ID cuts may be part of the jet which passed the 20 and 50 GeV trigger threshold. To remove the bias due to the lepton candidate originating from the trigger jet, we search the jet events for *another* high-p_T track in the event which is $\Delta R \geq 0.1$ radians away from the lepton candidate and which would also have passed the necessary jet E_T trigger threshold. To identify the tracks we use the selection cuts listed in Table B.2.4. After the $W^{\pm}$ and Z^0 removal discussed

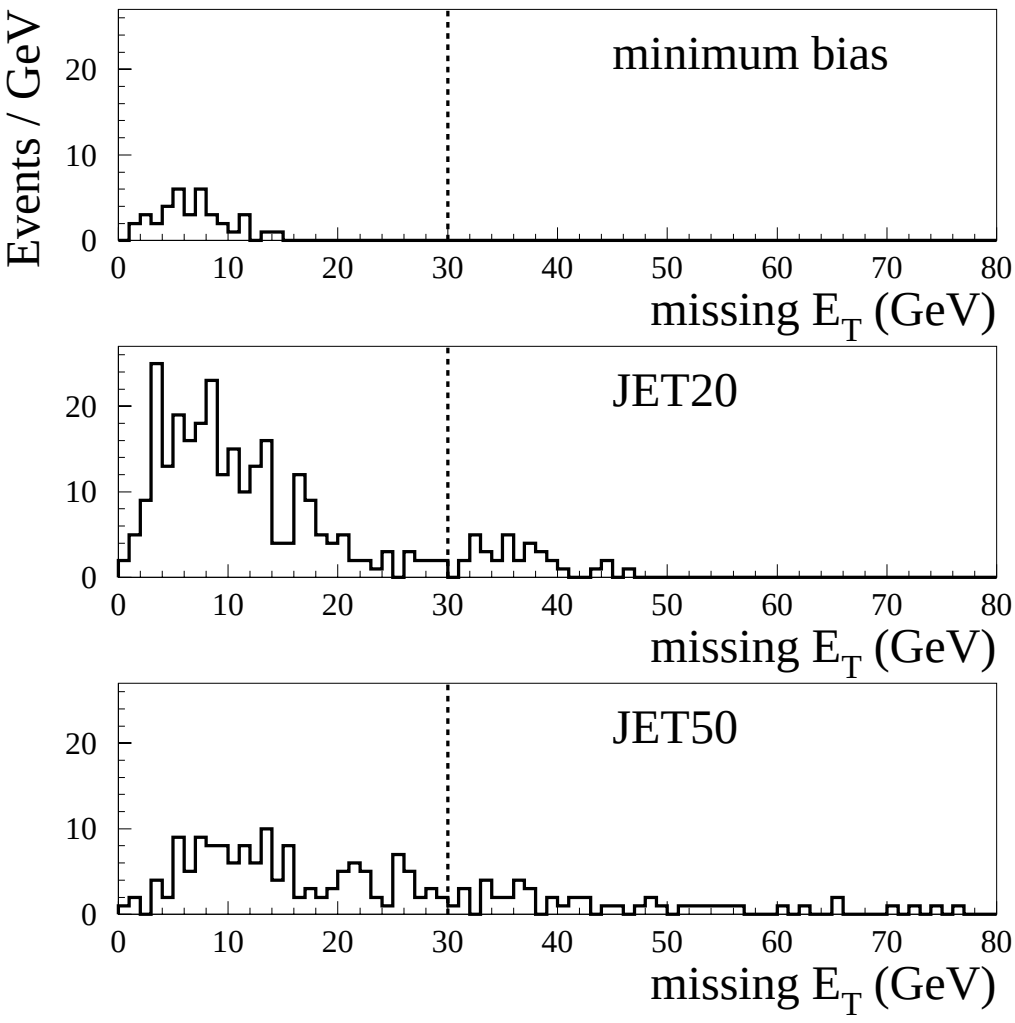

Figure B.7: Distribution of $\not\!\!E_T$ in minimum bias, JET20, and JET50 data. The missing $E_T < 30$ GeV cut is marked by the dashed lines.

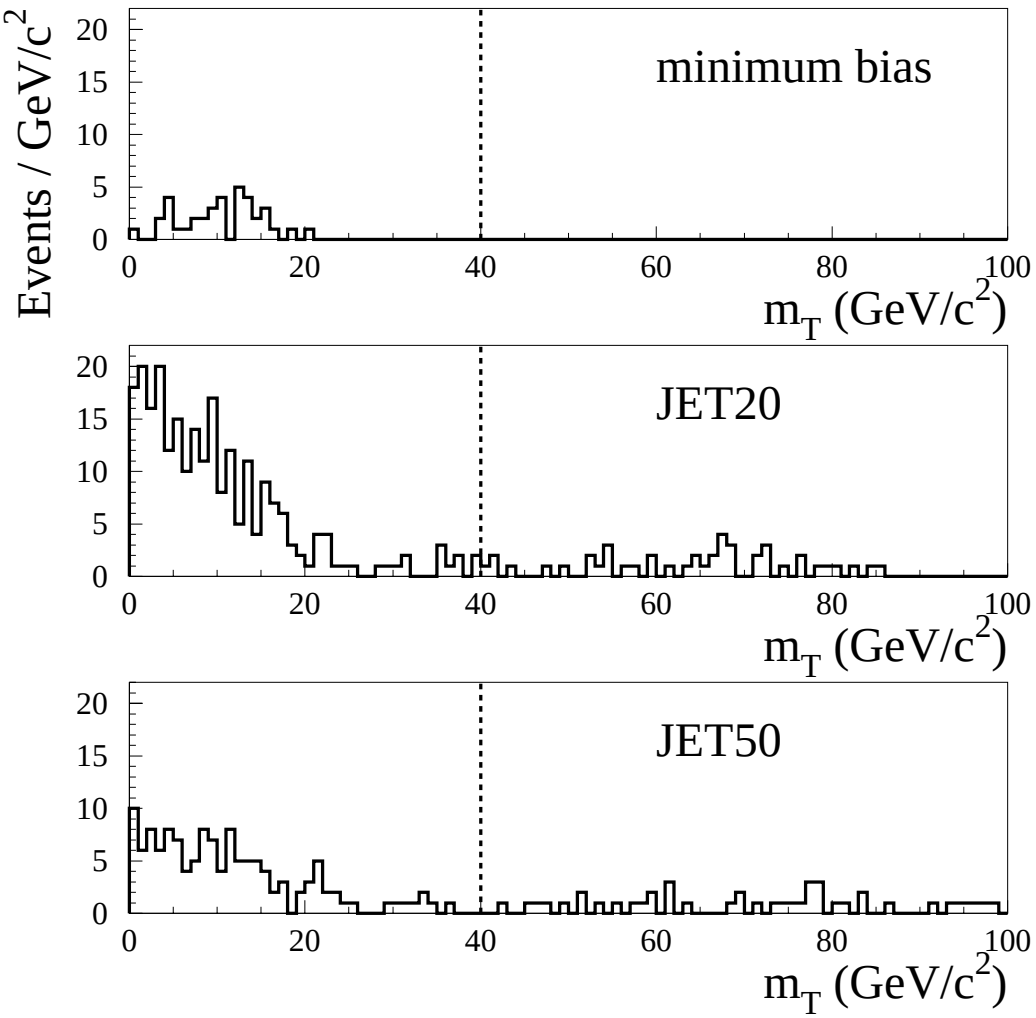

Figure B.8: Distribution of m_T in minimum bias, JET20, and JET50 data. The m_T < 40 GeV/c^2 cut is marked by the dashed lines.

	Cut	minimum bias events	JET20 events	JET50 events
Electrons	electron ID and event quality	37	289	185
	61 GeV/c^2 < $m_{\ell\ell}$ < 121 GeV/c^2	37	287	172
	$\not\!\!E_T$ < 30 GeV	37	254	129
	m_T < 40 GeV/c^2	37	238	107
	trigger bias	37	189	103
Muons	muon ID and event quality	31	195	137
	61 GeV/c^2 < $m_{\ell\ell}$ < 121 GeV/c^2	31	195	133
	$\not\!\!E_T$ < 30 GeV	31	191	103
	m_T < 40 GeV/c^2	31	187	95
	trigger bias	31	155	82

Table B.4: Summary of events remaining in the minimum bias, JET20, and JET50 samples after each unbiasing cut.

above, 79% and 96% of the remaining JET20 and JET50 events, respectively, have such a track. If no track is found satisfying these requirements, we remove the event from the JET20 or JET50 samples. After this requirement, we are left with jet samples of 37 minimum bias, 189 JET20, and 103 JET50 electron events and 31 minimum bias, 155 JET20, and 82 JET50 muon events. The events removed are summarized in Table B.4. We assume that the lepton candidates selected in these events are entirely from jets misidentified as leptons.

B.3 New Isolation

For the LSD analysis, we use a new definition of isolation energy in which we more carefully remove lepton E_T from the ISO sum. This new definition of isolation has two major components,

- Redefining the energy leakage from the lepton candidate E_T into calorimeter towers adjacent to the seed tower, $E_T^{leakage}$, to more distinctly separate isolated lepton signal from jet background. $E_T^{leakage}$ is originally defined as: $E_T^{leakage} \equiv {E_T}^{\eta-1} + {E_T}^{\eta+1}$. We make two important changes to $E_T^{leakage}$, (1) adding an electromagnetic calorimeter tower in ϕ into the $E_T^{leakage}$ sum and (2) removing a hadronic tower in η from the $E_T^{leakage}$ sum, depending on where the lepton candidate track extrapolates into the seed tower.

- Presenting a second cut on a wider ISO cone beyond the standard CDF Run I cut of $ISO_{\Delta R=0.4} < 2$ GeV in a cone of $\Delta R = 0.4$ radians used in Refs. [31, 77].

These changes are discussed in detail below.

B.3.1 ϕ Tower Removal

Figure B.9 is an enlarged diagram of the electromagnetic calorimeter towers at the center of the ISO cone. We divide the seed tower into four smaller "subwedges" in ϕ, labeled 1 through 4. If an electron candidate track extrapolates to one of the subwedges in ϕ on either edge of the seed tower, subwedges 1 or 4 represented by the darkly shaded regions in Figure B.9, we add into the $E_T^{leakage}$ sum the electromagnetic calorimeter tower energy in the ϕ tower adjacent to the subwedge that received the track, represented by the lightly-shaded regions in

Figure B.9:

$$E_T^{leakage} = E_T^{\eta-1} + E_T^{\eta+1} + E_T^{\phi\pm1} \ . \tag{B.8}$$

If the electron candidate track extrapolates to either of the central s in the seed tower, subwedges 2 or 3, we use the original definition of $E_T^{leakage}$ discussed above.

As an isolated signal-like electron candidate deposits a large amount of E_T in the electromagnetic calorimeter seed tower, we are removing a potential source of energy leakage into a nearby ϕ tower from the ISO sum and adding it into our definition of the electron candidate E_T. Figure B.10 shows the distributions of original and newly-reclustered $ISO_{\Delta R=0.4}$ for the signal-like electron sample. While the effect is small, comparing the ISO curves shows that a significant number of events have electron energy removed from the $ISO_{\Delta R=0.4}$ cone by the new reclustering. However, in jet backgrounds we expect E_T deposited over the entire cone. Thus, we are removing little energy on average from the ISO sum in the case of fake electrons. Figure B.11 shows the distributions of original and newly-reclustered $ISO_{\Delta R=0.4}$ for the fake electron samples.

B.3.2 η Tower Addition

Figure B.12 is an enlarged diagram of the hadronic calorimeter towers at the center of the ISO cone. In the same manner as we did for ϕ tower removal, we divide the seed tower into four smaller subwedges in η, labeled 1 through 4. If a muon candidate track extrapolates to one of the subwedges in η on either edge of the seed tower, subwedges 1 or 4, represented by the darkly-shaded regions in Figure B.12, we remove from the $E_T^{leakage}$ sum the hadronic calorimeter tower energy in the η tower *opposite* from the subwedge that received the track, represented by the lightly-shaded regions in Figure B.12:

$$E_T^{leakage} = E_T^{\eta\pm1} \ . \tag{B.9}$$

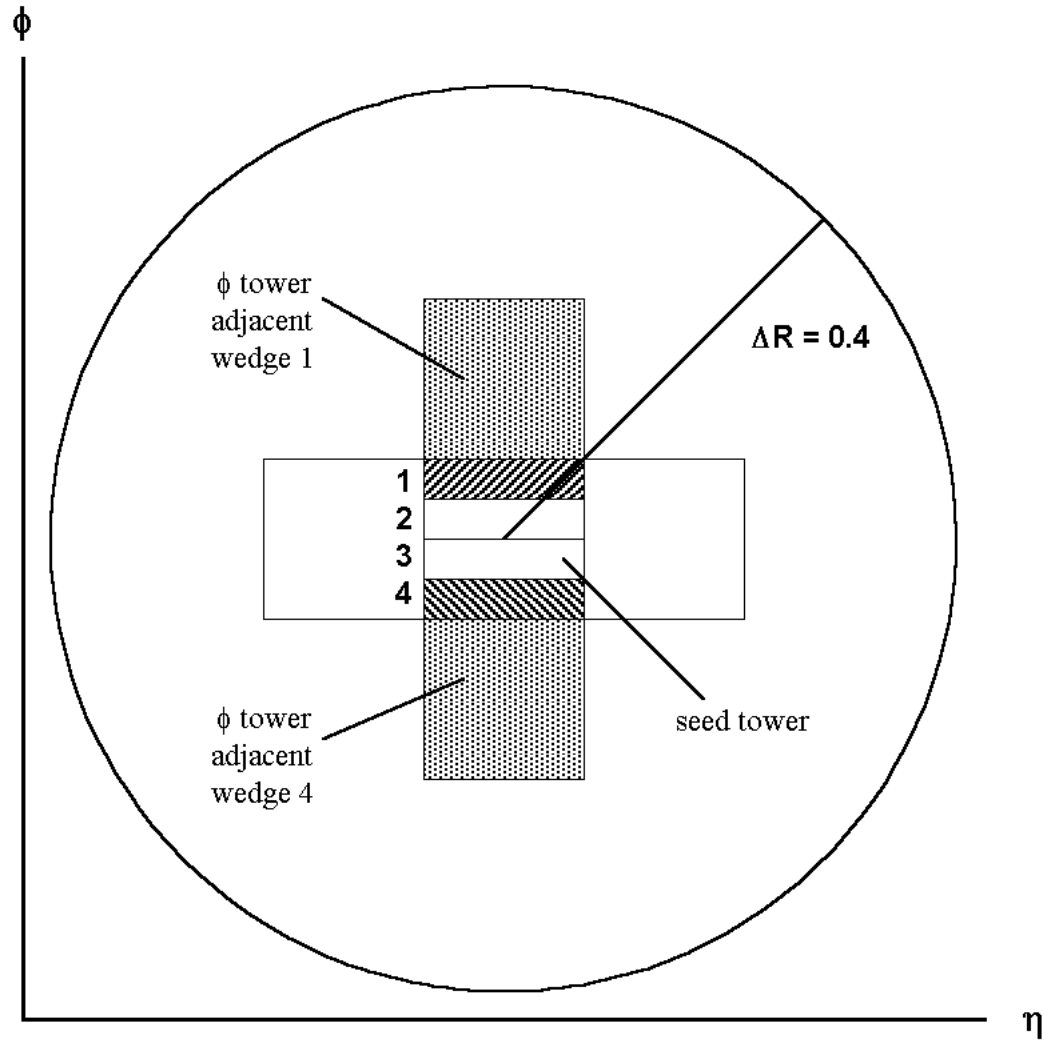

Figure B.9: Enlarged diagram of the electromagnetic calorimeter towers at the center of the ISO cone.

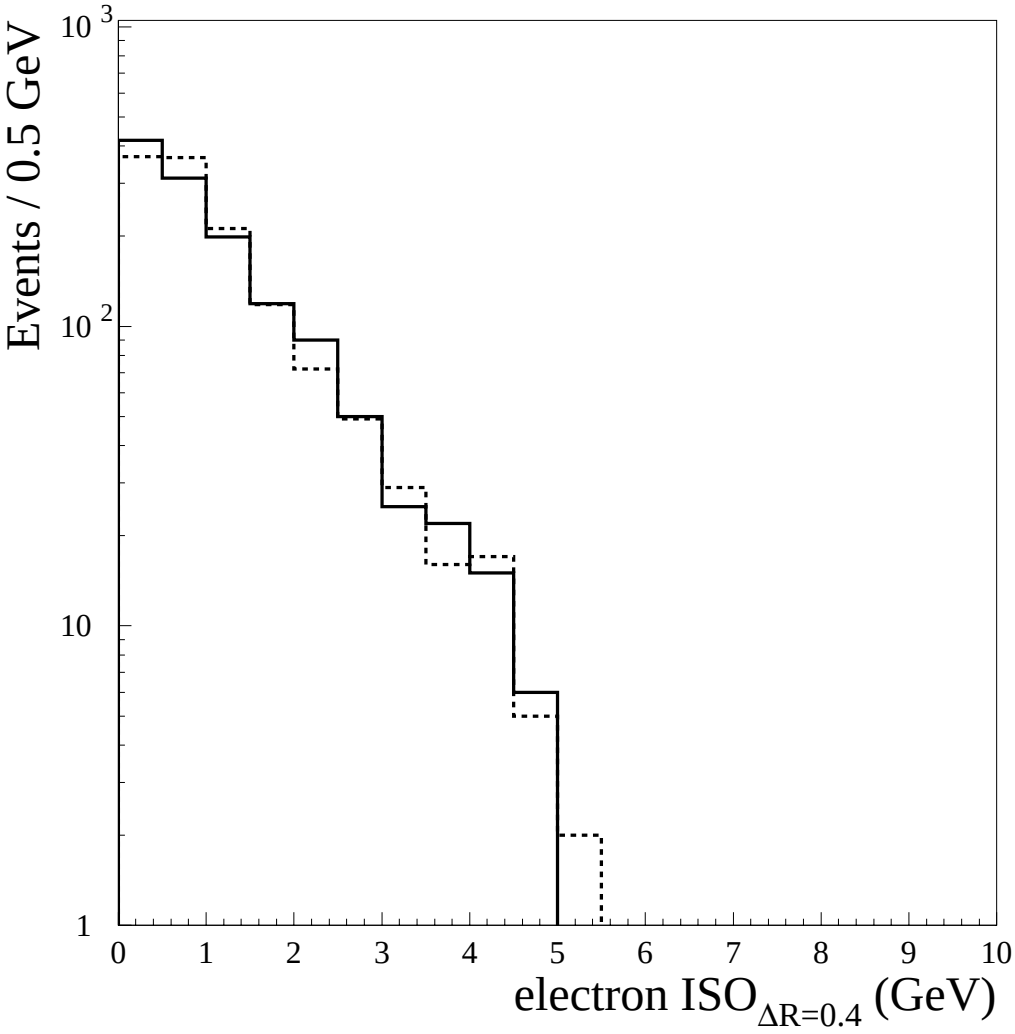

Figure B.10: Original (solid line) and newly-reclustered (dashed line) $ISO_{\Delta R=0.4}$ distributions for the signal-like electron sample.

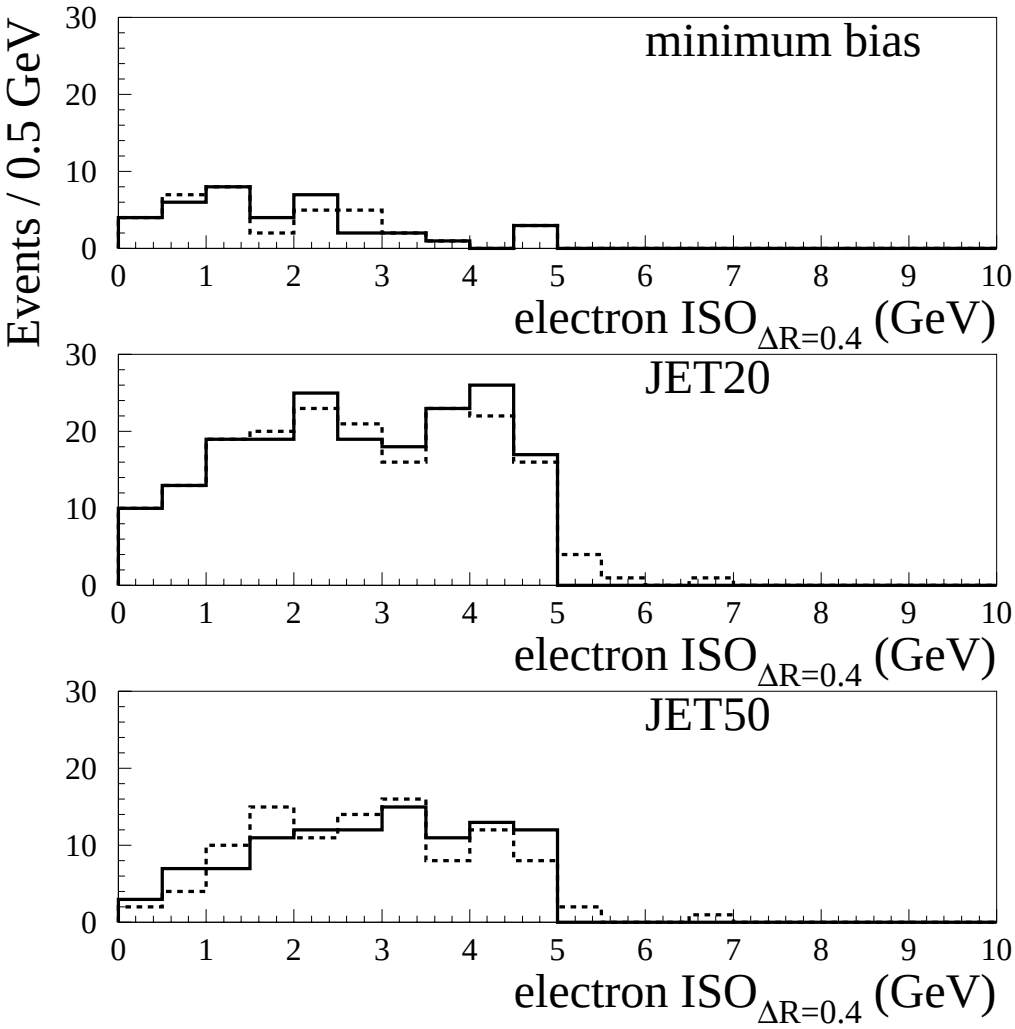

Figure B.11: Original (solid line) and newly-reclustered (dashed line) $ISO_{\Delta R=0.4}$ distributions for the fake electron samples.

If the muon candidate track extrapolates to either of the central subwedges in the seed tower, subwedges 2 or 3, we use the original definition of $E_T^{leakage}$ discussed above.

As an isolated signal-like muon candidate deposits a small amount of E_T into the hadronic calorimeter seed tower, we expect it to leak E_T weakly into the hadronic calorimeter tower in η on the opposite side of the seed tower from the muon impact. Thus, we are adding energy back into the ISO sum which was previously assumed to be a potential source of energy leakage into a nearby η tower. Figure B.13 shows the distributions of original and newly-reclustered $ISO_{\Delta R=0.4}$ for the signal-like muon sample. While the effect is again small, comparing the ISO curves shows that a significant number of events have muon energy returned to the $ISO_{\Delta R=0.4}$ cone by the new reclustering. However, in jet backgrounds we expect E_T deposited over the entire cone. Thus, we are adding little energy on average into the ISO sum in the case of fake muons. Figure B.14 shows the distributions of original and newly-reclustered $ISO_{\Delta R=0.4}$ for the fake muon samples.

B.3.3 Outer Cone Cut

In addition to ISO in a cone of $\Delta R = 0.4$ radians, we also calculate the amount of excess energy surrounding a lepton candidate in a cone of $\Delta R = 0.7$ radians centered on the seed tower using the newly-reclustered definition of ISO. Figure B.15 shows the $ISO_{\Delta R=0.7}$ distributions for the 2,510 signal-like electrons in the $Z^0 \rightarrow e^+e^-$ sample (solid line) and the 329 fake electrons in the combined jet samples (dashed line). No scaling has been applied to either distribution. We apply cut of $ISO_{\Delta R=0.7} < 7$ GeV, marked on Figure B.15 by a dotted line, removing $(50 \pm 3)\%$ of the fake electron background while retaining $(93.5 \pm 0.5)\%$

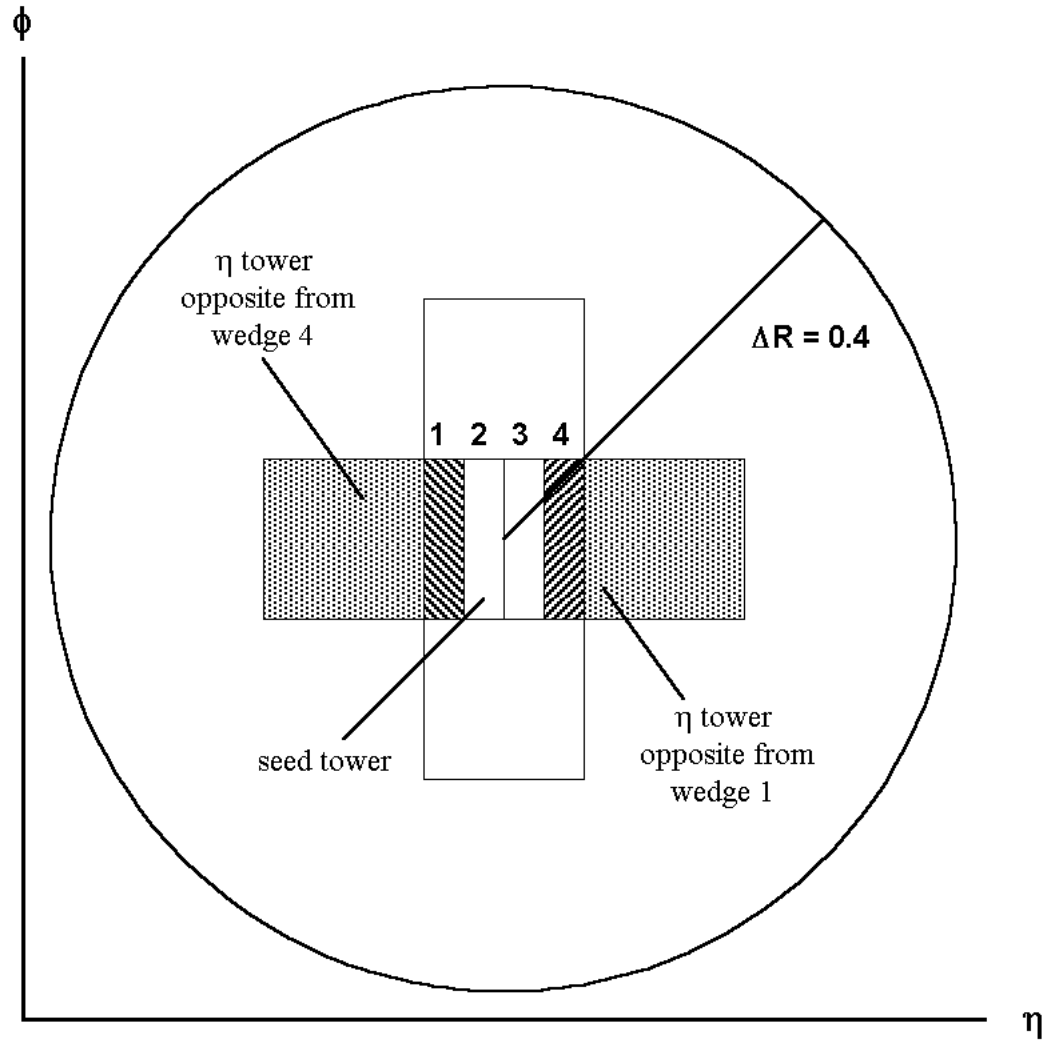

Figure B.12: Enlarged diagram of the hadronic calorimeter towers at the center of the ISO cone.

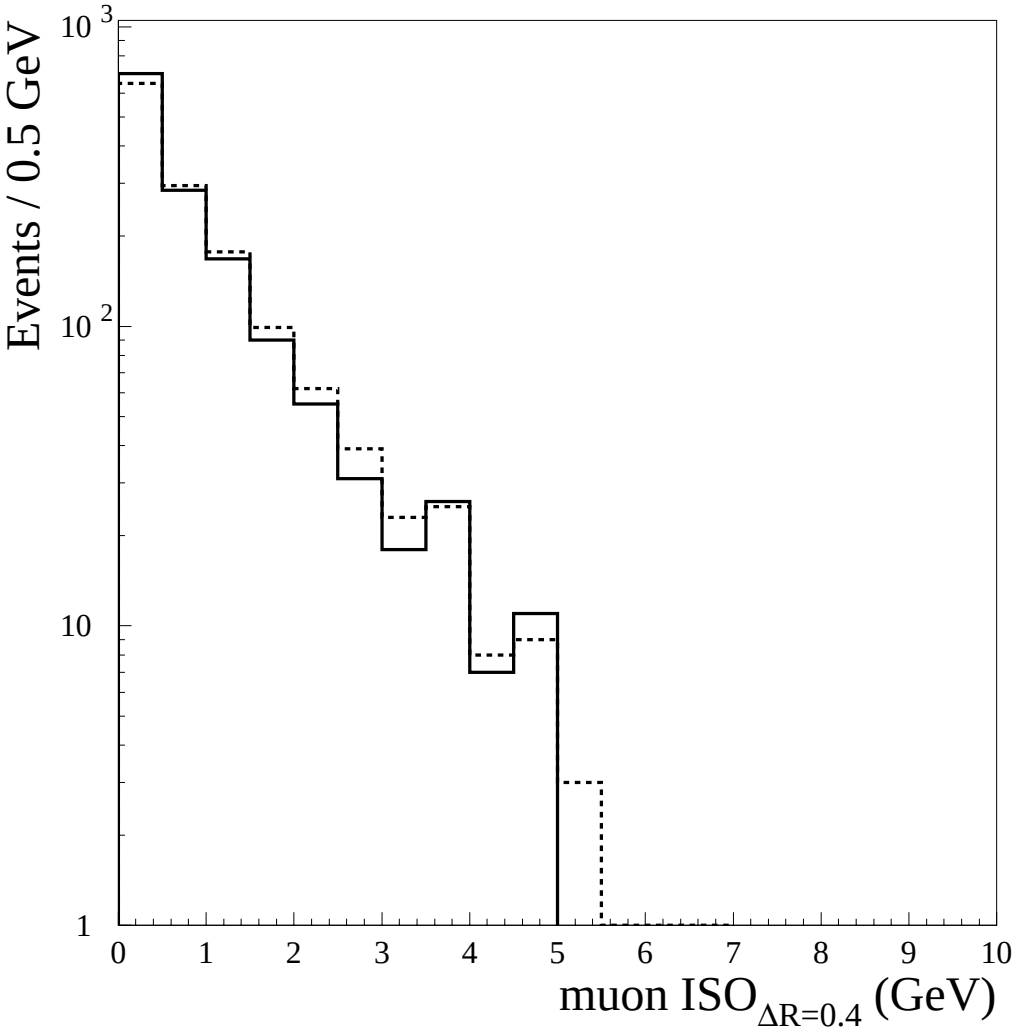

Figure B.13: Original (solid line) and newly-reclustered (dashed line) $ISO_{\Delta R=0.4}$ distributions for the signal-like muon sample.

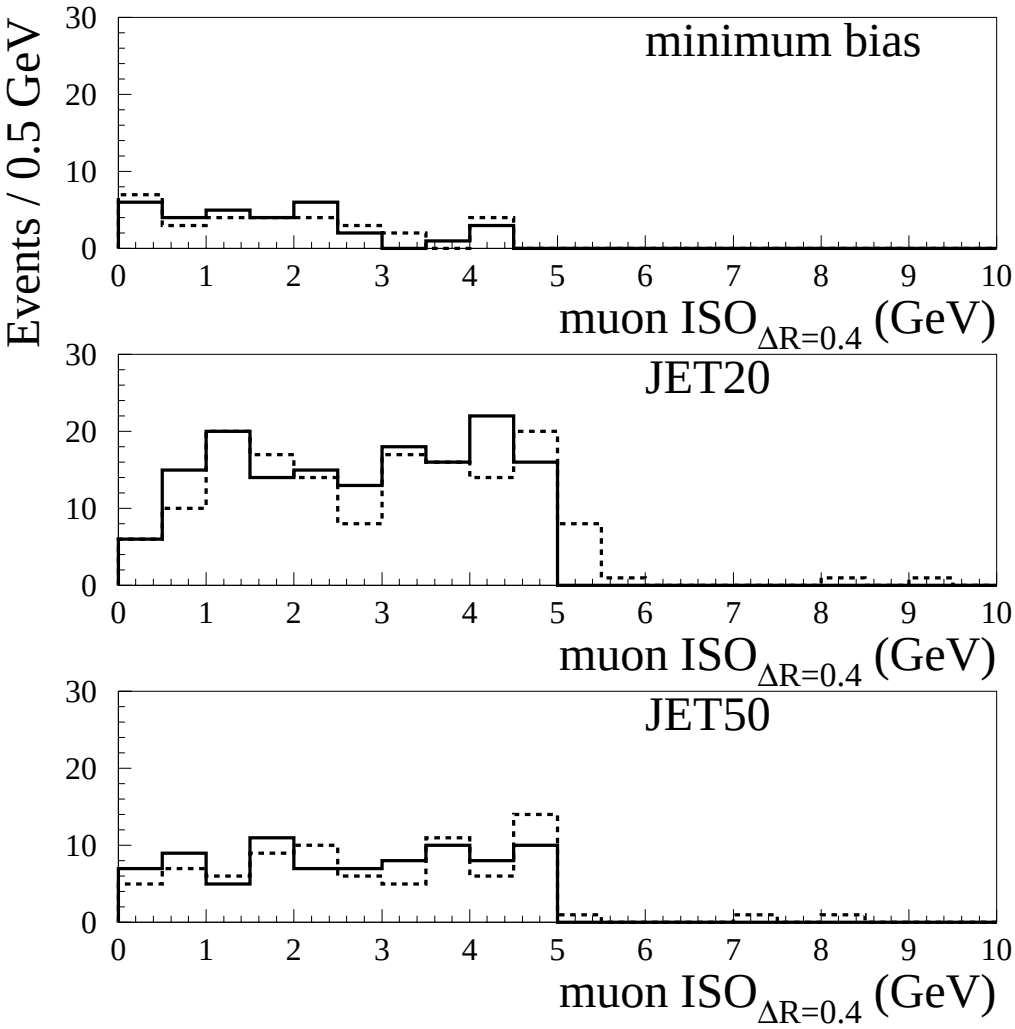

Figure B.14: Original (solid line) and newly-reclustered (dashed line) $ISO_{\Delta R=0.4}$ distributions for the fake muon samples.

of the signal electron sample.

Figure B.16 shows the $ISO_{\Delta R=0.7}$ distributions for the 2,778 signal-like muons in the $Z^0 \rightarrow \mu^+\mu^-$ sample (solid line) and the 268 fake muons in the combined jet samples (dashed line). No scaling has been applied to either distribution. We apply cut of $ISO_{\Delta R=0.7} < 7$ GeV, marked on Figure B.16 by a dotted line, removing $(57 \pm 3)\%$ of the fake muon background while retaining $(93.3 \pm 0.5)\%$ of the signal muon sample.

As Figures B.15 and B.16 show, the $ISO_{\Delta R=0.7} < 7$ GeV cut is in the tail of the signal-like lepton distributions, while near the peak of the fake lepton distributions. Thus, tightening the $ISO_{\Delta R=0.7}$ cut would continue to decrease the fake lepton background more rapidly than it would decrease the lepton signal efficiency. However, with the $ISO_{\Delta R=0.7}$ cut at 7 GeV, we are in general removing events with a large amount of energy in the event underlying the lepton production, while not necessarily removing leptons directly associated with jet production. This overall energy in the event underlying the lepton production is difficult to quantify. Thus, tightening the $ISO_{\Delta R=0.7}$ cut would make the effect of this cut difficult to interpret. With the loose cut, we can interpret $ISO_{\Delta R=0.7} < 7$ GeV as removing particularly energetic events with a large amount of calorimeter E_T or track p_T surrounding the lepton candidate, while leaving almost all the events with isolated signal lepton candidates intact.

B.3.4 Inner Cone Cut

With the outer cone $ISO_{\Delta R=0.7} < 7$ GeV cut applied to each lepton candidate, we now study the lepton signal efficiency as a function of jet background events selected with the inner cone $ISO_{\Delta R=0.4}$ variable using the newly-reclustered definition of ISO. After applying reclustered $ISO_{\Delta R=0.7} < 7$ GeV to each lepton

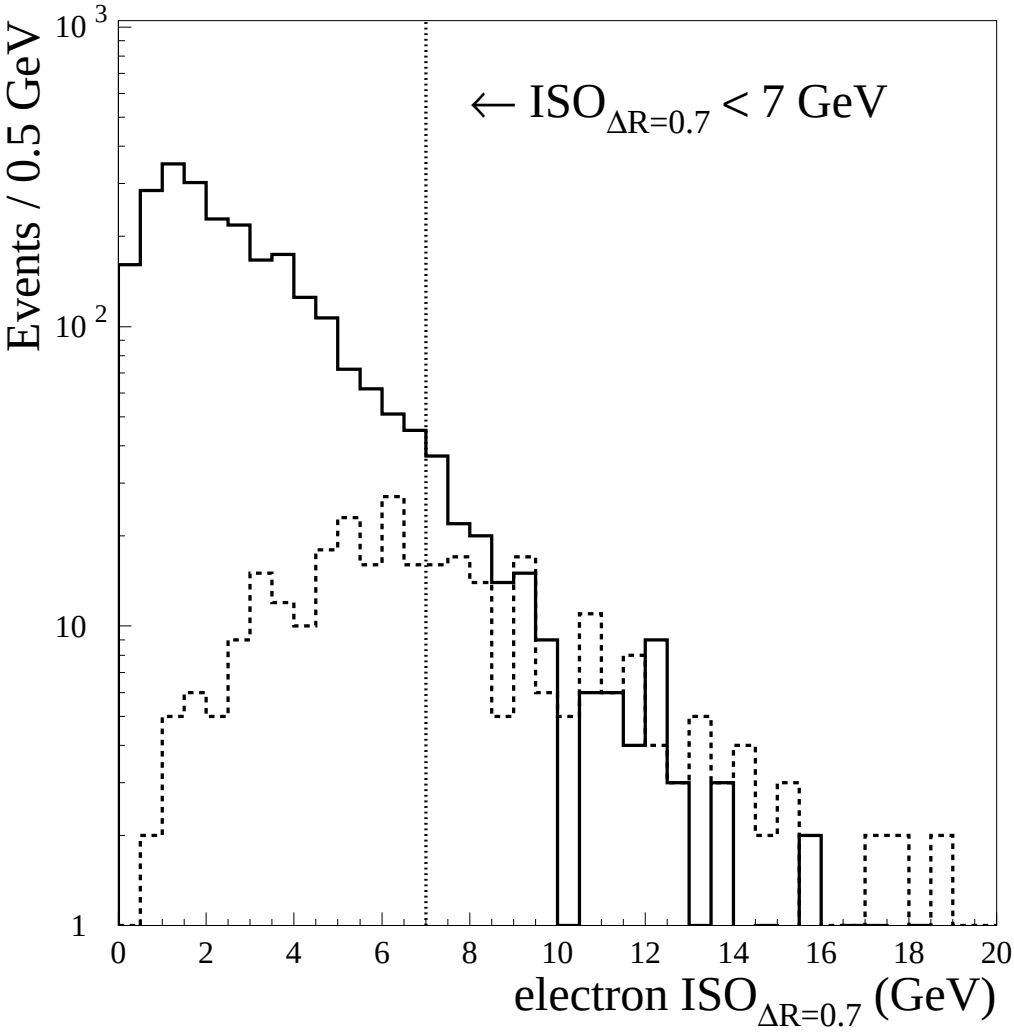

Figure B.15: Reclustered $ISO_{\Delta R=0.7}$ distributions for signal-like (solid line) and fake (dashed line) electrons. No scaling has been applied to either distribution. The $ISO_{\Delta R=0.7} < 7$ GeV cut is marked by the dotted line.

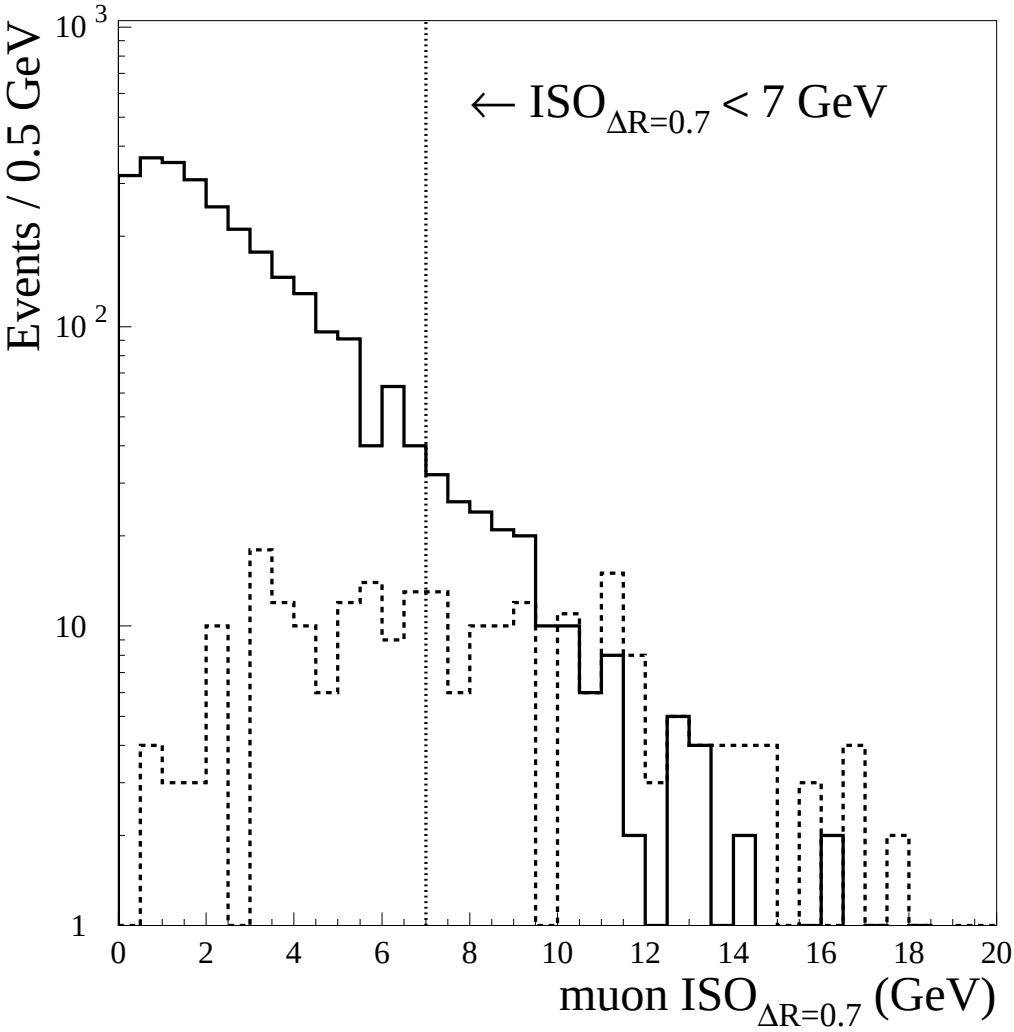

Figure B.16: Reclustered $ISO_{\Delta R=0.7}$ distributions for signal-like (solid line) and fake (dashed line) muons. No scaling has been applied to either distribution. The $ISO_{\Delta R=0.7} < 7$ GeV cut is marked by the dotted line.

candidate, we are left with signal-like lepton samples of 2,347 electrons and 2,591 muons and fake lepton samples of 165 electrons and 116 muons. The energy in the $ISO_{\Delta R=0.4}$ cone is not as dependent on the overall energy in the event underlying the lepton production as the $ISO_{\Delta R=0.7}$ cone. Thus, we find the inner cone cut in general removes events with individual lepton candidates which are directly associated with jet production.

Figure B.17 shows the $ISO_{\Delta R=0.4}$ distributions for the 2,347 signal-like electrons in the $Z^0 \rightarrow e^+e^-$ sample (solid line) and the 165 fake electrons in the combined jet samples (dashed line). No scaling has been applied to either distribution. In both of these samples, we vary an energy cut on $ISO_{\Delta R=0.4}$ between 1.0 and 4.0 GeV in 0.5 GeV increments. Table B.5 shows the number of signal-like electrons selected from each leg of the Z^0 (N_1 and N_2) and the electron signal efficiency (ϵ) defined in section B.2.3 along with the number of fake electrons selected from the jet samples (N_{fake}) for each cut on $ISO_{\Delta R=0.4}$.

Figure B.18 shows the $ISO_{\Delta R=0.4}$ distributions for the 2,591 signal-like muons in the $Z^0 \rightarrow \mu^+\mu^-$ sample (solid line) and the 116 fake muons in the combined jet samples (dashed line). No scaling has been applied to either distribution. In both of these samples, we vary an energy cut on $ISO_{\Delta R=0.4}$ between 1.0 and 4.0 GeV in 0.5 GeV increments. Table B.6 shows the number of signal-like muons selected from each leg of the Z^0 (N_1 and N_2) and the muon signal efficiency (ϵ) along with the number of fake muons selected from the jet samples (N_{fake}) for each cut on $ISO_{\Delta R=0.4}$.

The ISO energy distributions in Figures B.17 and B.18 end abruptly around $ISO_{\Delta R=0.4} \sim 5$ GeV. This is due to the loose $ISO_{\Delta R=0.4} < 5$ GeV cut made on each lepton candidate in the lepton ID cuts defined in sections B.2.1 and B.2.2. The distributions do not necessarily end exactly at 5 GeV because the selection

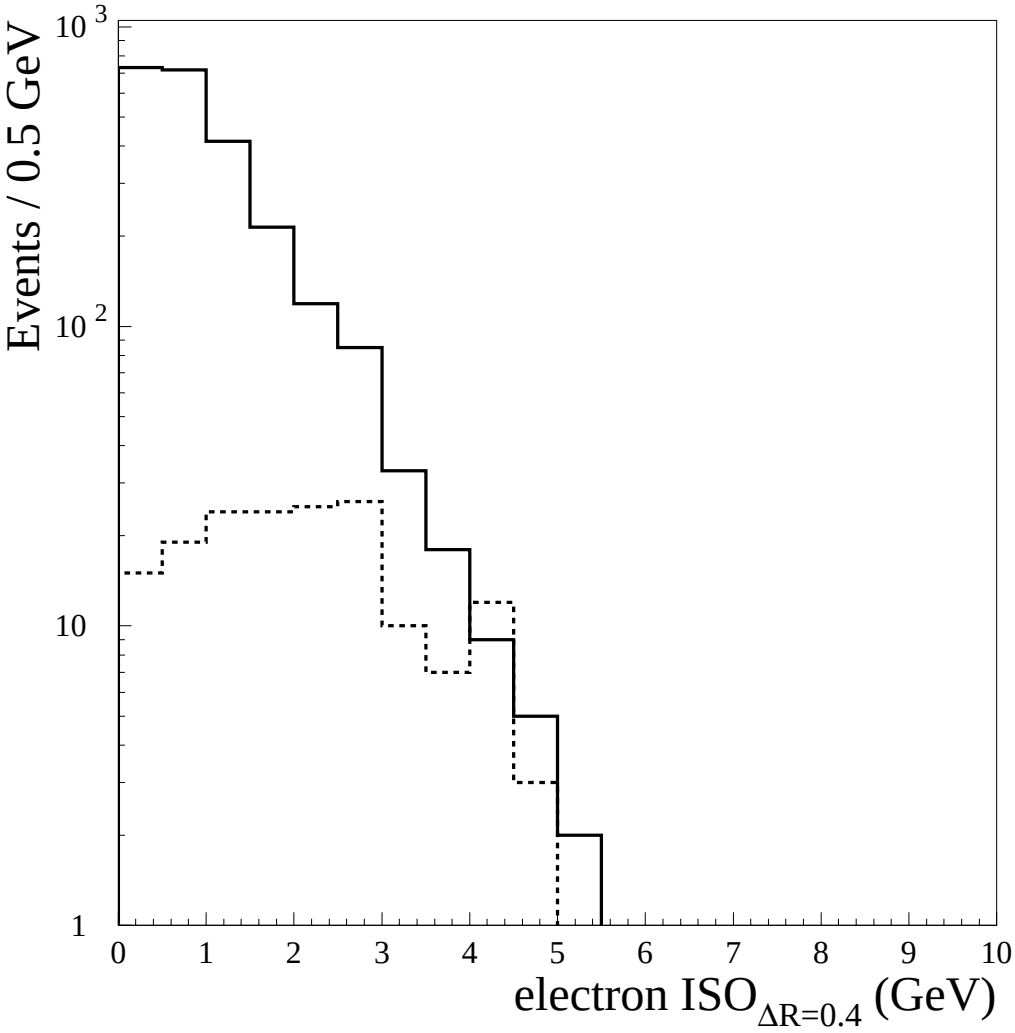

Figure B.17: Reclustered $ISO_{\Delta R=0.4}$ distributions for signal-like (solid line) and fake (dashed line) electrons. No scaling has been applied to either distribution.

$ISO_{\Delta R=0.4}$ Cut (GeV)	N_1	N_2	ϵ (%)	N_{fake}		
				min bias	JET20	JET50
1.0	725	723	57.7 ± 1.0	11	18	5
1.5	927	935	74.2 ± 0.9	18	28	12
2.0	1032	1044	82.7 ± 0.8	20	40	22
2.5	1094	1101	87.5 ± 0.7	22	55	30
3.0	1133	1147	90.8 ± 0.6	26	67	40
3.5	1148	1165	92.2 ± 0.5	28	74	41
4.0	1156	1175	92.9 ± 0.5	28	79	43

Table B.5: The number of signal-like electrons selected from each leg of the Z^0 (N_1 and N_2) and the electron signal efficiency (ϵ) along with the number of fake electrons selected from the minimum bias, JET20, and JET50 samples (N_{fake}) for each value of the reclustered $ISO_{\Delta R=0.4}$ cut.

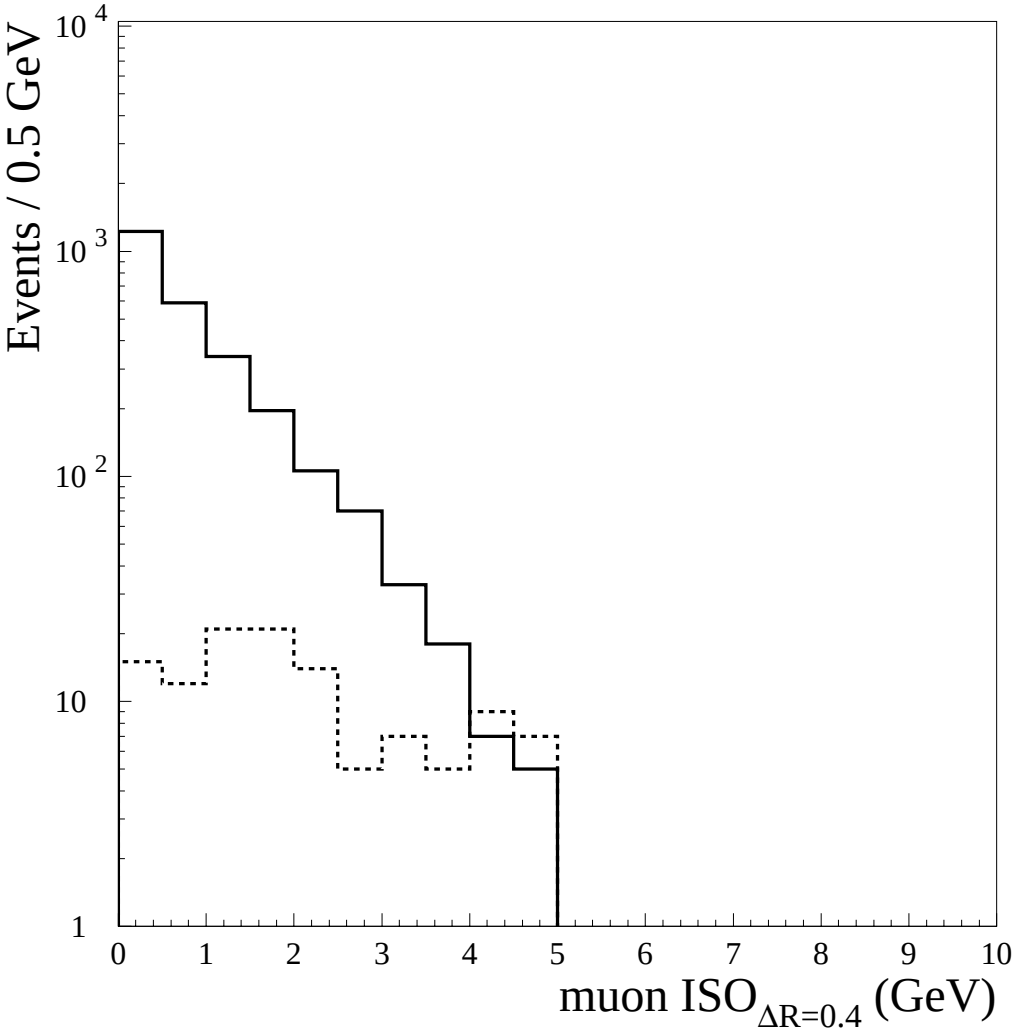

Figure B.18: Reclustered $ISO_{\Delta R=0.4}$ distributions for signal-like (solid line) and fake (dashed line) muons. No scaling has been applied to either distribution.

$ISO_{\Delta R=0.4}$ Cut (GeV)	N_1	N_2	ϵ (%)	N_{fake}		
				min bias	JET20	JET50
1.0	934	881	65.3 ± 0.9	10	13	4
1.5	1101	1055	77.6 ± 0.8	14	30	4
2.0	1189	1163	84.7 ± 0.7	17	42	10
2.5	1242	1216	88.5 ± 0.6	20	48	15
3.0	1276	1252	91.0 ± 0.5	22	50	16
3.5	1293	1268	92.2 ± 0.5	24	54	17
4.0	1302	1277	92.8 ± 0.5	24	57	19

Table B.6: The number of signal-like muons selected from each leg of the Z^0 (N_1 and N_2) and the muon signal efficiency (ϵ) along with the number of fake muons selected from the minimum bias, JET20, and JET50 samples (N_{fake}) for each value of the reclustered $ISO_{\Delta R=0.4}$ cut.

cut was made with the original definition of $ISO_{\Delta R=0.4}$ and in these Figures we are plotting the newly-reclustered $ISO_{\Delta R=0.4}$ variable which has shifted the energy in the ISO cone. However, we do not expect this truncation to bias the ISO efficiency study as it is well above the $1.0 < ISO_{\Delta R=0.4} < 4.0$ GeV region through which we scan the $ISO_{\Delta R=0.4}$ cut.

B.3.5 Signal Efficiency vs Background Events

To evaluate the efficacy of the newly-reclustered, double-cone definition of ISO, we plot lepton signal efficiency as a function of selected background events for the original and new definitions of ISO. The goal is to decrease the number of selected background events for a fixed lepton signal efficiency with the new ISO cut. We use the original definition of ISO, a single cone cut on $ISO_{\Delta R=0.4}$ with $E_T^{leakage} = E_T^{\eta+1} + E_T^{\eta-1}$ to generate Tables B.7 and B.8, which contain the same sliding $1.0 < ISO_{\Delta R=0.4} < 4.0$ GeV cut information as Tables B.5 and B.6 do for the new ISO.

From Tables B.5 and B.7 we plot the electron signal efficiency as a function of number of selected electron background events from the JET20 and JET50 samples for the original and new definitions of ISO in Figure B.19. From Tables B.6 and B.8 we plot the muon signal efficiency as a function of number of selected muon background events from the JET20 and JET50 samples for the original and new definitions of ISO in Figure B.20. We fit the points in each plot with a polynomial and draw the curves from the original (solid line) and new (dashed line) ISO fits. Each point on the curves represents a fixed cut on the $ISO_{\Delta R=0.4}$ cone between 1.0–4.0 GeV at 0.5 GeV intervals. The dotted line on each plot shows the fixed signal efficiency of 83.9% for electrons and 88.5% for muons for the original $ISO_{\Delta R=0.4} < 2$ GeV cut made by previous CDF lepton-based anal-

$ISO_{\Delta R=0.4}$ Cut (GeV)	N_1	N_2	ϵ (%)	N_{fake}		
				min bias	JET20	JET50
1.0	729	726	57.9 ± 1.0	10	23	10
1.5	928	941	74.4 ± 0.9	18	42	17
2.0	1047	1059	83.9 ± 0.7	22	61	28
2.5	1137	1131	87.5 ± 0.6	29	86	40
3.0	1187	1179	94.2 ± 0.5	31	105	52
3.5	1212	1211	96.5 ± 0.4	33	123	67
4.0	1234	1255	99.2 ± 0.2	34	146	78

Table B.7: The number of signal-like electrons selected from each leg of the Z^0 (N_1 and N_2) and the electron signal efficiency (ϵ) along with the number of fake electrons selected from the minimum bias, JET20, and JET50 samples (N_{fake}) for each value of the original $ISO_{\Delta R=0.4}$ cut.

$ISO_{\Delta R=0.4}$ Cut (GeV)	N_1	N_2	ϵ (%)	N_{fake}		
				min bias	JET20	JET50
1.0	983	952	69.7 ± 0.9	10	21	16
1.5	1151	1112	81.5 ± 0.7	15	41	21
2.0	1241	1217	88.5 ± 0.6	19	55	32
2.5	1296	1284	92.9 ± 0.5	25	70	39
3.0	1327	1320	95.3 ± 0.4	27	83	46
3.5	1345	1353	97.1 ± 0.3	27	101	54
4.0	1371	1372	98.7 ± 0.2	28	117	64

Table B.8: The number of signal-like muons selected from each leg of the Z^0 (N_1 and N_2) and the muon signal efficiency (ϵ) along with the number of fake muons selected from the minimum bias, JET20, and JET50 samples (N_{fake}) for each value of the original $ISO_{\Delta R=0.4}$ cut.

	ISO Cut	ϵ (%)	N_{fake}
Electrons	original $ISO_{\Delta R=0.4} < 2$ GeV	83.9 ± 0.7	89
	new $ISO_{\Delta R=0.4} < 2$ GeV $ISO_{\Delta R=0.7} < 7$ GeV	82.7 ± 0.8	62
Muons	original $ISO_{\Delta R=0.4} < 2$ GeV	88.5 ± 0.6	87
	new $ISO_{\Delta R=0.4} < 2$ GeV $ISO_{\Delta R=0.7} < 7$ GeV	84.7 ± 0.7	52

Table B.9: Summary of electron and muon signal efficiency (ϵ) from the $Z^0 \rightarrow \ell^+\ell^-$ samples and number of selected background events from the JET20 and JET50 samples (N_{fake}) for new and original definitions of ISO.

yses [31, 77]. These lines indicate that for a constant signal efficiency we have reduced background events from jets misidentified as leptons by a statistically significant amount for both electron and muon candidates.

To retain approximately the same signal efficiency for the ISO cut as the previous CDF Run 1 analyses, we fix the inner cone cut to be $ISO_{\Delta R=0.4} < 2$ GeV. Thus, we define the newly-reclustered, double-cone isolation cut:

$$ISO_{\Delta R=0.4} < 2 \text{ GeV} \tag{B.10}$$

$$ISO_{\Delta R=0.7} < 7 \text{ GeV} \tag{B.11}$$

Table B.9 summarizes the signal efficiencies from the $Z^0 \rightarrow \ell^+\ell^-$ samples and number of selected background events from the JET20 and JET50 samples for the original and new ISO cuts for both electrons and muons. With the new ISO cut, the number of jets misidentified as electrons has been reduced by a factor of $\sim$1.4 for an efficiency to retain signal-like electrons that is constant to within statistical errors. The number of jets misidentified as muons has also been

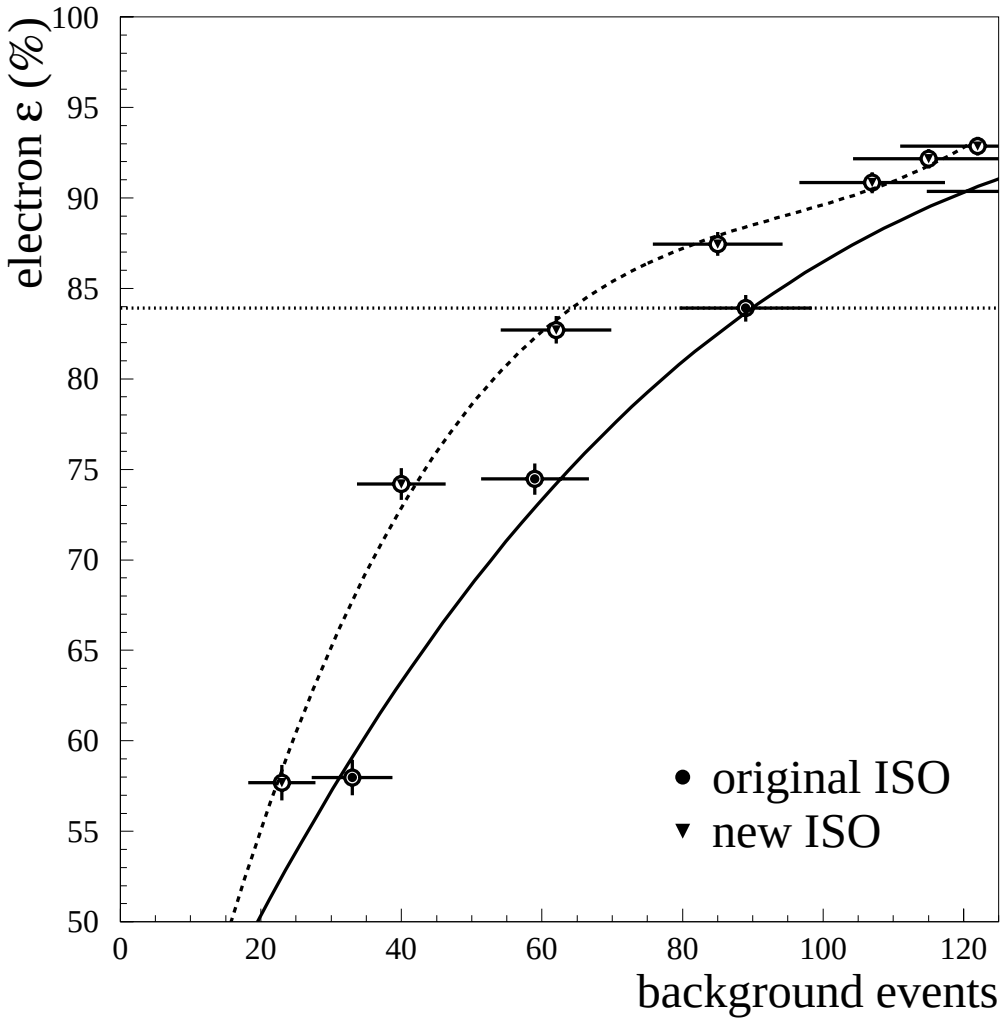

Figure B.19: Electron signal efficiency (ϵ) as a function of number of selected electron background events for the original (solid circles) and new (triangles) definitions of ISO. The dotted line shows the fixed signal efficiency of 83.9% for the original $ISO_{\Delta R=0.4} < 2$ GeV cut.

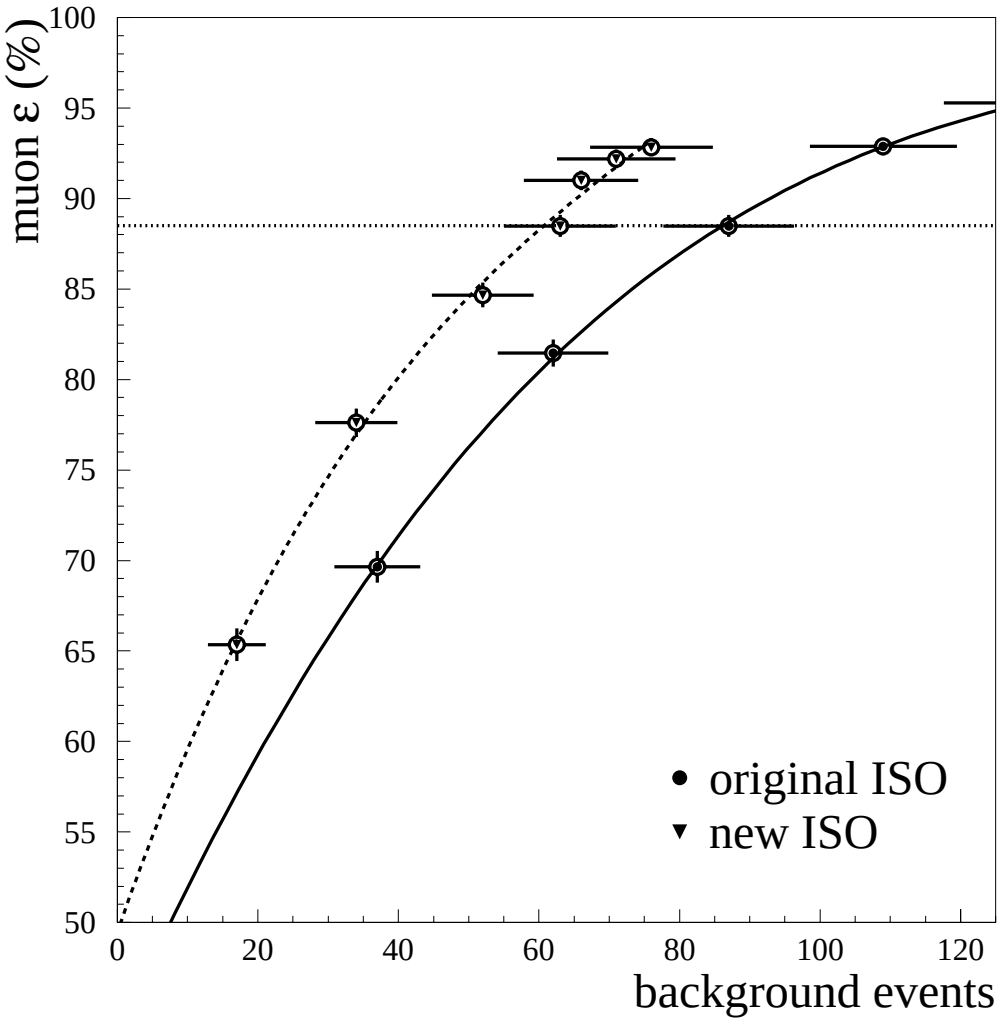

Figure B.20: Muon signal efficiency (ϵ) as a function of number of selected muon background events for the original (solid circles) and new (triangles) definitions of ISO. The dotted line shows the fixed signal efficiency of 88.5% for the original $ISO_{\Delta R=0.4} < 2$ GeV cut.

reduced by a factor of $\sim$1.7 for a $\sim$4% reduction in efficiency to retain signal-like muons. Thus, we have reduced lepton + fake backgrounds by a combined factor of $(1.4 \times 1.7) \sim 2.4$ for a nearly constant lepton signal efficiency. We further reduce difake backgrounds where both lepton candidates are selected from misidentified jets by a factor of $(2.4)^2$. We make the new definition of the newly-reclustered, double-cone ISO cut given in Equations D.10 and D.11 the default ISO cut for the LSD analysis presented in Chapter 3.

References

[1] Herman Melville. *Moby Dick*. Bantam Books, New York, 1876.

[2] K. G. Wilson, Phys. Rev. **D10**:2445-2459, 1974; G. Altarelli and G. Parisi, Nucl. Phys. **B126**:298, 1977.

[3] S. L. Glashow, Nucl. Phys. **22**:579-588, 1961; S. Weinberg, Phys. Rev. Lett. **19**:1264-1266, 1967; A. Salam, in *Elementary Particle Theory*, ed. N. Svartholm, Almquist and Wiksell, Stockhom, 1977.

[4] K. Hagiwara *et al.*, Phys. Rev. **D66**:010001, 2002.

[5] A. Einstein, *The Meaning of Relativity*, Princeton University Press, Princeton, 1950; A. Einstein *et al.*, *The Principle of Relativity*, Dover Publications, New York, 1952.

[6] S. N. Gupta, Phys. Rev. **96**:1683, 1954; R. H. Kraichnan, Phys. Rev. **98**:1118, 1955.

[7] D. Griffiths, *Introduction to Elementary Particles*, John Wiley & Sons, Inc., New York, 1987.

[8] F. Reines and C. L. Cowan, Jr., Phys. Rev. **92**:8301, 1953; C. L. Cowan *et al.*, Science **124**:103, 1956.

[9] Y. Fukuda *et al.* (Super-Kamiokande Collaboration), Phys. Rev. Lett. **81**:1562, 1998; Q. R. Ahmad *et al.* (SNO Collaboration), Phys. Rev. Lett. **89**:011301, 2002; K. Eguchi *et al.* (KamLAND Collaboration), Phys. Rev. Lett. **90**:021802, 2003.

[10] M. Veltman, Phys. Lett. **B70**:253, 1977; B. W. Lee, C. Quigg, and H. B. Thacker, Phys. Rev. Lett. **38**, 1977; *ibid.* Phys. Rev. **D16**:1519, 1977.

[11] G. Abbiendi *et al.* (LEP Working Group for Higgs Boson Searches), Phys. Lett. **B565**:61, 2003; V. M. Abazov *et al.* (DØ Collaboration), Phys. Rev. Lett. **87**:231801, 2001; F. Abe *et al.* (CDF Collaboration), Phys. Rev. Lett. **81**:5748, 1998.

[12] M. Drees and S. Martin, "Implications of SUSY Model Building", in *Report of the DPF Working Group on Electroweak Symmetry Breaking and Beyond the Standard Model*, hep-ph/9504324, 1995.

[13] A. H. Chamseddine, R. Arnowitt, and P. Nath, Phys. Rev. Lett. **49**:970, 1982; R. Barbieri, S. Ferroa, and C. A. Savoy, Phys. Lett. **B119**:343, 1982; L. Hall, J. Lykken, and S. Weinberg, Phys. Rev. **D27**:2359, 1983.

[14] G. t'Hooft in *Recent Developments in Gauge Theories*, eds. G. t'Hooft *et al.*, Plenum, New York, 1980.

[15] J. C. Pati and A. Salam, Phys. Rev. **D10**:275, 1974.

[16] R. D. Peccei and H. Quinn, Phys. Rev. Lett. **38**:1440, 1977; S. Weinberg, Phys. Rev. Lett. **40**:223, 1978.

[17] H. P. Nilles, Phys. Rept. **110**:1, 1984; H. E. Haber and G. I. Kane, Phys. Rept. **117**:75, 1985.

[18] H. Murayama and M. Peskin, *Ann. Rev. Nucl. Part. Sci.* 1996, hep-ex/9606003; G. Anderson, D. Castano and A. Riotto, hep-ph/9609463, 1996.

[19] S. Dawson, *SUSY and Such*, hep-ph/9612229, 1996.

[20] P. Fayet, Phys. Lett. **B69**:489, 1977; G. Farrar and P. Fayet, Phys. Lett. **B76**:3900, 1995.

[21] J. Lopez, Rept. Prog. Phys. **59**:819-865, 1996.

[22] For example, T. S. Kosmas and J. D. Vergados, Phys. Rev. **D55**:1752-1764, 1997.

[23] L. Bergström and A. Goobar, *Cosmology and Particle Astrophysics*, John Wiley & Sons, New York, 1999.

[24] M. Drees, *An Introduction to Supersymmetry*, hep-ph/9611409, 1996.

[25] R. Arnowitt and P. Nath, *Supersymmetry and Supergravity: Phenomenology and Grand Unification,* in Proceedings of VII$^{\rm th}$ J. A. Swieca Summer School, Campos de Jordao, Brazil, 1993.

[26] J. Nachtman, *Search for Charginos at $\sqrt{s}$ = 161 and 172 GeV with the Aleph Detector*, Ph.D. thesis, University of Wisconsin-Madison, 1997.

[27] W. Oller, H. Eberl, W. Majerotto, and C. Weber, Eur. Phys. J. **C29**:563-572, hep-ph/0304006, 2003.

[28] A. Bartl, H. Fraas, and W. Porod, Z. Phys. **C64**:499, 1994; *ibid*, Z. Phys. **C68**:518, (erratum) 1995.

[29] J. Gunion and H. Haber, Phys. Rev. **D37**:2515, 1988.

[30] G. Azuelos *et al.*, *Beyond the Standard Model Working Group: Summary Report*, hep-ph/0204031, 2002.

[31] F. Abe *et al.* (CDF Collaboration), Phys. Rev. Lett. **76**:4307, 1996; F. Abe *et al.* (CDF Collaboration), Phys. Rev. Lett. **80**:5275, 1998.

[32] S. Abachi et al. (DØ Collaboration), Phys. Rev. Lett. **76**:2228, 1996; B. Abbott et al. (DØ Collaboration), Phys. Rev. Lett. **80**:1591, 1998.

[33] A. Heister *et al.* (ALEPH Collaboration), Phys. Lett. **B533**:223, 2002; R. Barate *et al.* (ALEPH Collaboration), Phys. Lett. **B499**:67, 2001; P. Abreu *et al.* (DELPHI Collaboration), Phys. Lett. **B489**:38, 2000.

[34] H. Baer *et al.*, "Low Energy Supersymmetry Phenomenology", in *Report of the DPF Working Group on Electroweak Symmetry Breaking and Beyond the Standard Model*, hep-ph/9503479, 1995.

[35] J. Bagger, U. Nauenberg, X. Tata, and A. White, *Summary of the Supersymmetry Working Group*, hep-ph/9612359, 1995; F. Paige, in *New Directions for High-Energy Physics*:710, eds. D. Cassel, L. Gennari and R. Siemann, SLAC, Stanford, 1997.

[36] For examples of inclusive analyses, see C. Balazs *et al.*, Phys. Lett. **B489**:157-162, 2000; S. Ambrosanio *et al.*, Phys. Rev. **D54**: 5395-5411, 1996.

[37] See, for example, G. Abbiendi *et al.* (OPAL Collaboration), Eur. Phys. J. **C33**:173-212, 2004; S. Braibant, *SUSY Searches at LEP*, in *Proceedings of Moriond '03*, 2003.

[38] M. Worcester, J. Nachtman, and D. Saltzberg (CDF Collaboration), Int. J. Mod. Phys. **A16S1B**:797, 2001.

[39] D. B. Cline, Lett. Nuovo Cim. **41**:518, 1984.

[40] See, for example, F. Almeida *et al.*, Phys. Lett. **B400**:331, 1997; A. Ali *et al.*, Eur. Phys. J. **C21**:123, 2001.

[41] *e.g.*, see Th. Rizzo, Int. J. Mod. Phys. **A11**:1563, 1996.

[42] For a discussion of blind analyses, see P. F. Harrison, in *Proceedings of Advanced Statistical Techniques in Particle Physics*:278-289, Durham, UK, 2002.

[43] F. E. Paige *et al.*, hep-ph/9810440, 1998.

[44] T. Sjöstrand *et al.*, Computer Phys. Commun. **135**:238, 2001; T. Sjöstrand, L. Lönnblad and S. Mrenna, hep-ph/0108264, 2001.

[45] J. M. Campbell, hep-ph/0105226, 2001.

[46] Attributed to the Greek playwright Menander (342 - 291 B.C.), in *The Woman Possessed with a Divinity*.

[47] J. Thompson. "Introduction to Colliding Beams at Fermilab." Technical Report FERMILAB-TM-1909, 1994.

[48] F. Abe *et al.*, Nucl. Instrum. Meth. **A271**:387-403, 1988.

[49] D. Amidei *et al.*, Nucl. Instrum. Meth. **A350**:73-130, 1994.

[50] J. P. Marriner, "Tevatron Luminosity Upgrade Project", in *EPAC '98 Proceedings*, IOP Publishing, 1998.

[51] R. Blair *et al.* "The CDF II Detector: Technical Design Report." Technical Report FERMILAB-PUB-96-390-E, 1996.

[52] D. Bortoletto for the CDF II Collaboration, Nucl. Instrum. Meth. **A386**:87-95, 1997.

[53] F. Abe *et al.* (CDF Collaboration), Phys. Rev. **D50**:2966-3026, 1994.

[54] A. Caner, CDF Internal Note CDF/ANAL/MONTECARLO/CDFR/2177, 1993.

[55] J. P. Done, M. Chertok, T. Kamon, CDF Internal Note CDF/ANAL/EXOTIC/CDFR/4218, 1997.

[56] William Shakespeare, *Hamlet*, ed. G. R. Hibbard, Oxford University Press, New York, 1987.

[57] F. Abe *et al.* (CDF Collaboration), Phys. Rev. **D52**:2624, 1994.

[58] B. Tannenbaum, *A Search for Chargino-Neutralino Production at the Fermilab Tevatron Collider*, Ph.D. thesis, University of New Mexico, 1997.

[59] S. Kopp and C. Grosso-Pilcher, CDF Internal Note CDF/DOC/ELECTROWEAK/CDFR/1992, 1993.

[60] M. Miller, CDF Internal Note CDF/ANAL/ELECTRON/CDFR/1086, 1989.

[61] K. Ragan, J. Walsh, and H. H. Williams, CDF Internal Note CDF/ANAL/ELECTRON/CDFR/0902, 1989; M. Gold, CDF Internal Note CDF/ANAL/ELECTRON/CDFR/0913, 1989.

[62] A. Scott, J. Hauser, D. Saltzberg, and P. Murat, CDF Internal Note CDF/ANAL/ELECTROWEAK/CDFR/4755, 1998.

[63] R. Swartz, CDF Internal Note CDF/DOC/CDF/CDFR/1259, 1990.

[64] F. Abe *et al.* (CDF Collaboration), Phys. Rev. Lett. **62**:613, 1989; F. Abe *et al.* (CDF Collaboration), Phys. Rev. Lett. **68**:1104, 1992; F. Abe *et al.* (CDF Collaboration), Phys. Rev. Lett. **77**:438, 1996.

[65] F. Abe *et al.* (CDF Collaboration), Phys. Rev. **D50**:4252, 1994.

[66] S. Abachi *et al.* (DØ Collaboration), Phys. Rev. Lett. **74**:3548, 1995.

[67] B. Aubert *et al.* (BABAR Collaboration), Phys. Rev. Lett. **88**:221802, 2002.

[68] K. Abe *et al.* (Belle Collaboration), Phys. Rev. Lett. **86**:3228-3232, 2001; N. C. Hastings *et al.* (Belle Collaboration), Phys. Rev. **D67**:052004, 2003.

[69] F. Abe *et al.* (CDF Collaboration), Phys. Rev. Lett. **80**:2779-2784, 1998.

[70] F. Abe *et al.* (CDF Collaboration), Phys. Rev. **D44**:29-52, 1991.

[71] F. Abe *et al.* (CDF Collaboration), Phys. Rev. Lett. **73**:2296, 1993; F. Abe *et al.* (CDF Collaboration), Phys. Rev. Lett. **79**:4760, 1997.

[72] F. Abe *et al.* (CDF Collaboration), Phys. Rev. Lett. **70**:4042, 1993; F. Abe *et al.* (CDF Collaboration), Phys. Rev. **D63**:072003, 2001.

[73] A. Scott, *A Measurement of Low Mass Drell-Yan Production at the Collider Detector at Fermilab*, Ph.D. thesis, University of California, Los Angeles, 2000.

[74] F. Abe *et al.* (CDF Collaboration), Phys. Rev. Lett. **78**:4536-4540, 1997; DØ places a limit on $\sigma(WW \to \text{leptons})$ in S. Abachi *et al.* (DØ Collaboration), Phys. Rev. **D56**:6742-6778, 1997.

[75] F. Abe *et al.* (CDF Collaboration), Phys. Rev. Lett. **64**:157, 1990; F. Abe *et al.* (CDF Collaboration), Phys. Rev. Lett. **79**:2636, 1997.

[76] F. Abe *et al.* (CDF Collaboration), Phys. Rev. Lett. **62**:3020, 1989; F. Abe *et al.* (CDF Collaboration), Phys. Rev. Lett. **69**:2896, 1992; F. Abe *et al.* (CDF Collaboration), Phys. Rev. Lett. **77**:5336, 1996.

[77] F. Abe *et al.* (CDF Collaboration), Phys. Rev. Lett. **83**:2133, 1999; F. Abe *et al.* (CDF Collaboration), Phys. Rev. Lett. **87**:251803, 2001.

[78] M. Worcester, CDF Internal Note CDF/ANAL/EXOTIC/CDFR/5081, 1999.

[79] F. Abe *et al.* (CDF Collaboration), Phys. Rev. Lett. **61**:1819, 1988.

[80] M. Worcester, J. Nachtman, and D. Saltzberg, in *Proceedings of the Division of Particles and Fields Conference 1999*, Los Angeles, USA, 1999; *ibid*, CDF Internal Note CDF/ANAL/EXOTIC/CDFR/4874, 1999.

[81] Mark Twain. *Great Short Works of Mark Twain.* Harper & Row, New York, 1967.

[82] J. R. Taylor. *An Introduction to Error Analysis.* University Science Books, United States of America, 1982.

[83] J. Conway, in *Proceedings of Workshop on Confidence Limits*, Geneva, Switzerland, 2000.

[84] M. Cvetic and P. Langacker, Phys. Rev. **54**:3570, 1996; M. Cvetic and P. Langacker, Mod. Phys. Lett. **A11**:1247, 1996.

[85] J. Lykken *et al.* (New Phenomena Working Group), in *Proceedings of the 1996 DPF/DPB Summer Study on New Directions in High-energy Physics*, Snowmass, CO, 1996.

[86] F. Abe *et al.* (CDF Collaboration), Phys. Rev. Lett. **68**:1463-1467, 1992; F. Abe *et al.* (CDF Collaboration), Phys. Rev. Lett. **67**:2418-2422, 1991.

[87] M. Worcester, J. Nachtman, N. Wisniewski, and D. Saltzberg, CDF Internal Note CDF/ANAL/EXOTIC/CDFR/6607, 2003.

[88] T. Plehn, private communication.

[89] W. Beenakker, R. Hopker, and M. Spira, hep-ph/9611232, 1996.

[90] For more details on experimental signatures of representative mSUGRA models, see S. Abdullin *et al.* (CMS Collaboration), J. Phys. **G28**:469, 2002; V. Krutelyov *et al.*, Phys. Lett. **B505**:161, 2001.

[91] F. Abe *et al.* (CDF Collaboration), Phys. Rev. Lett. **76**:2006, 1996; F. Abe *et al.* (CDF Collaboration), Phys. Rev. Lett. **88**:041801, 2002; B. Abbott *et al.* (DØ Collaboration), Phys. Rev. Lett. **83**:4937, 1999.

[92] F. Scott Fitzgerald. *The Great Gatsby.* Simon & Schuster, New York, 1925.

[93] M. Danielson, in *New Directions for High-Energy Physics*:720, eds. D. Cassel, L. Gennari and R. Siemann, SLAC, Stanford, 1997.

[94] J. P. Done, M. Chertok, T. Kamon, CDF Internal Note CDF/ANAL/EXOTIC/CDFR/4291, 1998.